Instituut voor
Kern- en Stralingsfysica
Departement Natuurkunde
Faculteit Wetenschappen

KATHOLIEKE UNIVERSITEIT
LEUVEN

MAGNETIC MOMENTS OF ISOMERS AND GROUND STATES OF EXOTIC NUCLEI PRODUCED BY PROJECTILE FRAGMENTATION

Promotors:
Prof. Em. R. Coussement
Dr. G. Neyens

Proefschrift ingediend tot
het behalen van de graad van
doctor in de wetenschappen
door

Georgi Georgiev

2001

Contents

Introduction

Even though the structure of the atomic nucleus is governed to a large extent by the strong interaction between the nucleons, most of our present knowledge on the nuclear properties has been obtained from the interaction of the nuclei with electromagnetic fields. Examples are provided by excitation energies, transition rates, magnetic and electric moments etc. The interaction of the external electromagnetic fields with the electric charge and current distribution inside the nucleus is the one which allows us to measure the above mentioned nuclear characteristics. Comparison of the experimental results with theoretical calculations provides the background of our understanding of the physical origin of complex nuclear processes.

A particular valuable information on the wave function of a given nuclear state is provided by the static nuclear moments. Since the wave function of a single state is involved in the estimation of their expectation values, the magnetic and electric moments are the most sensitive tools for testing the single-particle nature of a state and, hence, can serve as an impetus for further extending and deepening of our understanding of the nuclear structure.

Current nuclear models are well established theories, describing the properties of the nuclei close to the valley of β-stability. In the recent years due to the fast developments of the exotic (radioactive) beam facilities and in nuclear detection techniques, more and more nuclear species further away from stability are becoming available for investigation. Under the extreme conditions of the nuclear spin and isospin some deviations of the regularities are observed, namely there is experimental evidence for a change in the energy spacing between the different orbits (quenching of shell closures and also appearance of new (sub) shell closures). In such a situation there is a need for a rigorous test of the existing nuclear models and for our understanding of the nuclear prop-

erties far from stability. This test ground can be provided by measuring magnetic moments of nuclear ground and/or excited (isomeric) states.

So far, the nucleon-nucleon interaction, neither the bare one nor the in-medium, is well understood. Therefore, the majority of nuclear models still exploit the phenomenological effective interaction, based mostly on the available empirical information. In this situation there is a strong need for a rigorous test of the existing nuclear models and eventually for our understanding of the properties of nuclei far from stability. Such a testing ground can be provided by measuring magnetic moments of nuclear ground and/or excited (isomeric) states.

In the first chapter of this work a brief overview of the theory of nuclear moments will be given, including the electromagnetic interaction in nuclei, the nuclear orientation formalism, the production and conservation of a spin-oriented ensemble of nuclei, as well as two methods used in this work for the measurement of nuclear magnetic moments: $\underline{N}$uclear $\underline{M}$agnetic $\underline{R}$esonance (NMR) and $\underline{T}$ime $\underline{D}$ependent $\underline{P}$erturbed $\underline{A}$ngular $\underline{D}$istribution (TDPAD). The second chapter contains the results and the interpretation of an experiment to measure the ground state magnetic moment of ^{32}Cl, performed at the National Superconducting Cyclotron Laboratory, MSU, USA. The third chapter is devoted to the g-factor measurement of short-lived isomers of nuclei in the vicinity of ^{68}Ni, which was performed at the Grand Accelerateur National d'Ions Lourds, Caen, France. In the last part we will present the conclusions and an outlook.

Chapter 1

Measurements of magnetic moments

1.1 Introduction

Much of what we know about the nuclei comes from studying not the strong nuclear interaction of nuclei with their surroundings, but from the much weaker electromagnetic interaction. The strong nuclear interaction reflects the distribution and the motion of the nucleons in the nucleus, while the electromagnetic interaction can be taken as a small perturbation and even neglected in certain cases (e.g., when comparing the properties of the 'mirror' nuclei). Thus, when using electromagnetic probes in the measurement process we do not disturb seriously the object we are trying to investigate.

The simplest way of studying the properties of nuclei by means of electromagnetic interactions is to measure the interaction of their charge and current distribution with a known static field. It is convenient to assign to the charge and current distribution an electromagnetic multipole moment associated with each characteristic spatial dependence - the $1/r^2$ electric field arises from the net charge, which can be assigned a monopole moment; the $1/r^3$ electric field arises from the first or dipole moment; the $1/r^4$ electric field arises from the second or quadrupole moment and so on. The magnetic multipole moments behave similarly, with the exception of the magnetic monopole moment which, as far as we know, does not exist (there are no 'magnetic charges').

3

Another restriction on the multipole moments comes from the symmetry of the nucleus and is directly related to the parity of the nuclear states. Each electromagnetic multipole moment has a parity which is determined by the behaviour of the multipole operator when $\mathbf{r} \to -\mathbf{r}$. The parity of electric moments is $(-1)^l$ while the parity of the magnetic moments is $(-1)^{l+1}$, where l is the order of the moment ($l = 0$ for monopole, $l = 1$ for dipole, $l = 2$ for quadrupole, *etc.*). When we compute the expectation value of a moment, we have to evaluate an integral form like $\int \psi^* \mathbf{O} \psi \, dv$, where $\mathbf{O}$ is the appropriate electromagnetic operator. If $\mathbf{O}$ has an odd parity then the integrand is an odd function of the coordinates and must vanish identically. Thus all odd-parity static multipole moments must vanish - *i.e.* electric dipole, magnetic quadrupole, electric octupole and so on.

1.2 Definitions

It is found experimentally that nuclei with non-zero spin have a magnetic dipole moment given by:

$$\mu = gI\mu_N \tag{1.1}$$

where g is know as the nuclear gyromagnetic ratio, I is the total angular momentum of the nuclear state, $\mu_N = e\hbar/2M$ is the nuclear magneton which has a value of $5.05084 \times 10^{-27} J/T$ and M is the proton mass. There is a clear analogy between the nuclear magneton (μ_N) and the Bohr magneton (μ_B) for which the mass M is the mass of the electron. Note that $\mu_N \ll \mu_B$ due to the difference in the masses, thus in most conditions the nuclear magnetism has a much smaller effect compared to the atomic magnetism. Usually the nuclear magnetic moments are expressed in units of μ_N so from now on, if not mentioned explicitly, we will follow this convention.

There are two sources of the nuclear magnetism:

- the orbital movement of the charged particles (protons) in the nucleus generates a loop current, thus a magnetic field;

- the intrinsic spin of the nucleons, $s = \frac{1}{2}$, generates its own intrinsic magnetic field.

The magnetic dipole operator of a nuclear state can be written as a

sum of two terms [Cas90]:

$$\vec{\mu} = \sum_{k=1}^{A} g_{\ell}^{(k)} \vec{\ell}^{\,(k)} + \sum_{k=1}^{A} g_{s}^{(k)} \vec{s}^{\,(k)} \qquad (1.2)$$

where the summation is over all nucleons in the nucleus and $\vec{\ell}^{(k)}$ and $\vec{s}^{(k)}$ are the orbital and the spin angular momentum operators for the kth nucleon, respectively. Here g_ℓ and g_s are the orbital and the spin gyromagnetic ratios. For a free proton $g_\ell^\pi = 1$ and for a free neutron $g_\ell^\nu = 0$, thus the orbital magnetization comes entirely from the protons. The spin gyromagnetic factors have been measured experimentally for free protons and neutrons and have values [Kra88]:

$$\begin{aligned} g_s^\pi &= 5.5856912 \pm 0.0000022 \\ g_s^\nu &= -3.8260837 \pm 0.0000018 \end{aligned} \qquad (1.3)$$

The magnetic moment of a nuclear state can be calculated using equation (1.2) as the expectation value of the z-component of the magnetic moment operator in a magnetic substate $M = I$. If we note the wave function of a nuclear state with spin I in a magnetic substate M as $|IM\rangle$, then the magnetic moment is defined as:

$$\mu = gI = \langle II | \vec{\mu}_z | II \rangle \qquad (1.4)$$

We can simplify this expression, using the fact that the nuclear Hamiltonian is rotationally invariant and the Wigner-Eckart theorem (see App. A)

$$\mu = \langle II10 | II \rangle \langle I \| \vec{\mu} \| I \rangle = \sqrt{\frac{I}{(I+1)}} \langle I \| \vec{\mu} \| I \rangle$$

Note that from angular momentum selection rules the Clebsch-Gordan coefficient is non-vanishing only if $2I \geq 1$ which means that nuclear states with spin 0 have no magnetic dipole moment.

The magnetic moment is related to the $\overrightarrow{M1}$ operator via the equation

$$\mu = gI = \langle II | \sqrt{\frac{4\pi}{3}} \overrightarrow{M1}_z | II \rangle \qquad (1.5)$$

Often, it is convenient to introduce the isospin concept, when describing the properties of nuclei. In the isospin formalism, the neutron

and the proton are regarded as two different states of one and the same particle. Then, the wave function of a nucleon will depend not only on the space and spin coordinates, but also on the isospin variable τ_z, which distinguishes between a proton ($\tau_z = +1$) and a neutron ($\tau_z = -1$). In these notations, the magnetic dipole moment operator can be rewritten in the form

$$
\begin{aligned}
\vec{\mu} \quad = \quad & g_\ell^{IS} \sum_{k=1}^{A} \vec{\ell}^{\,(k)} + g_\ell^{IV} \sum_{k=1}^{A} \vec{\ell}^{\,(k)} \tau_z^{(k)} \\
+ \quad & g_s^{IS} \sum_{k=1}^{A} \vec{s}^{\,(k)} + g_s^{IV} \sum_{k=1}^{A} \vec{s}^{\,(k)} \tau_z^{(k)}
\end{aligned}
\tag{1.6}
$$

where

$$
\begin{aligned}
g_\ell^{IS} &= 1/2(g_\ell^\pi + g_\ell^\nu) = 0.5 \\
g_\ell^{IV} &= 1/2(g_\ell^\pi - g_\ell^\nu) = 0.5 \\
g_s^{IS} &= 1/2(g_s^\pi + g_s^\nu) = 0.880 \\
g_s^{IV} &= 1/2(g_s^\pi - g_s^\nu) = 4.706
\end{aligned}
\tag{1.7}
$$

The gyromagnetic ratios with superscript IS are called isoscalar g-factor (they are coupling constants associated with operators which are isospin independent) and those with superscript IV are called isovector g-factors.

To calculate the magnetic moment of a nuclear state, we can use equation (1.2) and evaluate the expectation value of the magnetic moment operator for a state with $M = I$. Since in a jj coupling scheme ℓ_z and s_z are not conserved, we can use the expression $\vec{j} = \vec{\ell} + \vec{s}$ and rewrite (1.2) in the form

$$
\vec{\mu} = \sum_{k=1}^{A} g_\ell \vec{j}^{\,(k)} + (g_s - g_\ell)\vec{s}^{\,(k)}
\tag{1.8}
$$

Taking the expectation value for $M = I$ gives the result

$$
\langle \mu \rangle = g_\ell j + (g_s - g_\ell)\langle s_z \rangle
\tag{1.9}
$$

The expectation value $\langle s_z \rangle$ can be calculated (see, e.g., [Kra88]) if we take into account that $\vec{j}$ is the only vector of interest and $\vec{\ell}$ and $\vec{s}$ are meaningful only in their relation to $\vec{j}$ (see, e.g., [Kra88])

$$
\langle s_z \rangle = \frac{j}{2j(j+1)} \left[j(j+1) - \ell(\ell+1) + s(s+1) \right] \hbar
\tag{1.10}
$$

which gives the magnetic moment for the two different cases:

$$
\begin{aligned}
j &= \ell + \frac{1}{2} & \langle\mu\rangle &= g_\ell\left(j - \frac{1}{2}\right) + \frac{1}{2}g_s \\
j &= \ell - \frac{1}{2} & \langle\mu\rangle &= g_\ell\frac{j(j+3/2)}{(j+1)} - \frac{1}{2}\frac{j}{j+1}g_s
\end{aligned}
\tag{1.11}
$$

1.2.1 Magnetic moments of odd-mass nuclei

Let us now consider an odd-mass nucleus, which has one unpaired proton (neutron). In the extreme single particle shell model, the properties of such a nucleus should be determined only by the single unpaired nucleon and the rest of the nucleons, coupled to spin $I = 0$ pairs, should not influence, *e.g.*, the magnetic moment of the nucleus. For such a configuration, the magnetic moment should be directly reproduced by the equations (1.11). The computed values, known as Schmidt lines, are presented for neutrons and protons in Fig. 1.1 and Fig. 1.2, respectively. Some experimental magnetic moments are presented on the figures with full dots. We can note the following points for the Schmidt diagrams:

- the moments of most single particle nuclei deviate inwards from the Schmidt lines

- the experimental values, in general, do follow the trend of the Schmidt lines but are smaller in amplitude and are considerably scattered.

The main reason for the deviation of the experimentally measured magnetic moments from the Schmidt values is the fact that, for computing the Schmidt values, we used free nucleons g-factors, while the nucleons in the nuclei are not free particles. They interact via exchange of mesons. This leads to a correction of the magnetic moment, known as meson-exchange current (MEC) corrections. The relatively large scattering of the measured magnetic moments can give us an indication that the magnetic moment, depends on the particular nuclear configuration. This means that the assumption we made in the extreme single particle shell model is not fully correct and we also have to take into account the configuration mixing.

1.2.2 Additivity relation

Let us now consider a nucleus which is assumed to consist of three groups of nucleons: a core with $I_{core} = 0$ and two groups labeled A and B with
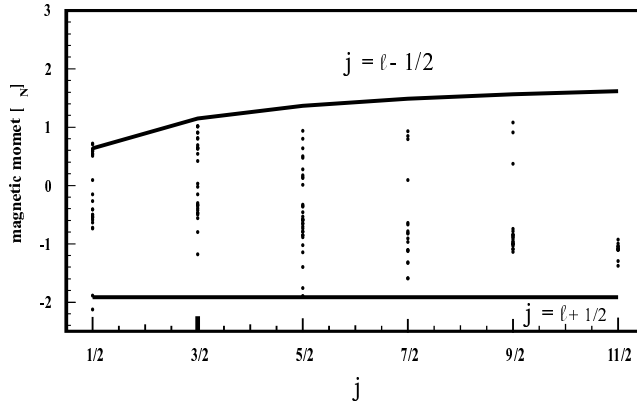
Figure 1.1: *Schmidt diagram for odd-neutron nuclei. The dots are the experimentally measured values.*
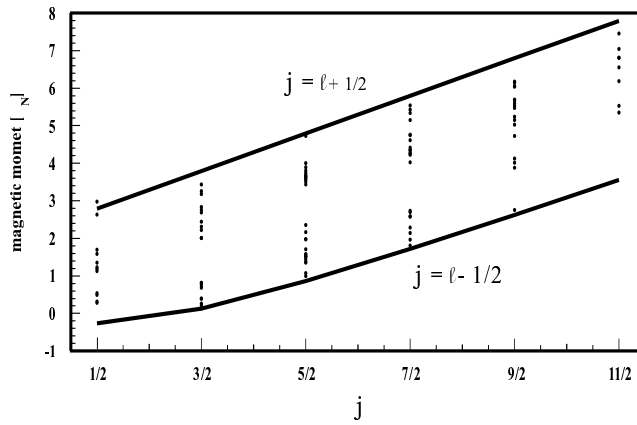

Figure 1.2: *Schmidt diagram for odd-proton nuclei. The dots are the experimentally measured values.*

angular momenta I_A and I_B, respectively. The total angular momentum of such a nucleus is $\vec{I} = \vec{I}_A + \vec{I}_B$. One can write the magnetic moment of state $|IM = I\rangle$ as

$$\mu = gI = \langle II|gI_z|II\rangle. \qquad (1.12)$$

If we assign g-factors g_A and g_B to the groups A and B, respectively, the magnetic moment of the system can be written

$$\mu = gI = \langle II|g_A I_{Az} + g_B I_{Bz}|II\rangle \tag{1.13}$$

where we neglect the interaction between the two groups. Each of the g-factors (g_A and g_B) depend on the structure of the respective groups and can possibly include interaction with the core. Using the generalized Landé formula [Bru77] we can write the magnetic moment and the g-factor as

$$\mu = \frac{\langle II|g_A \vec{I}_A \cdot \vec{I} + g_B \vec{I}_B \cdot \vec{I}|II\rangle}{I(I+1)}\langle II|I_z|II\rangle \tag{1.14}$$

$$g = \frac{\langle II|g_A \vec{I}_A \cdot \vec{I} + g_B \vec{I}_B \cdot \vec{I}|II\rangle}{I(I+1)}. \tag{1.15}$$

To evaluate the matrix elements of $\vec{I}_A \cdot \vec{I}$ and $\vec{I}_B \cdot \vec{I}$ we can use the relation $\vec{I} = \vec{I}_A + \vec{I}_B$ and write

$$\vec{I}_A \cdot \vec{I} = \vec{I}_A \cdot (\vec{I}_A + \vec{I}_B) = \vec{I}_A^2 + \vec{I}_A \cdot \vec{I}_B$$
$$\vec{I}^2 = (\vec{I}_A + \vec{I}_B)^2 = \vec{I}_A^2 + \vec{I}_B^2 + 2\vec{I}_A \cdot \vec{I}_B$$
$$\vec{I}_A \cdot \vec{I}_B = \frac{1}{2}(\vec{I}^2 - \vec{I}_A^2 - \vec{I}_B^2)$$

from where we can derive

$$\vec{I}_A \cdot \vec{I} = \frac{1}{2}(\vec{I}^2 + \vec{I}_A^2 - \vec{I}_B^2)$$
$$\vec{I}_B \cdot \vec{I} = \frac{1}{2}(\vec{I}^2 + \vec{I}_B^2 - \vec{I}_A^2)$$

After substituting this into (1.15), we can find

$$\begin{aligned} g &= \frac{g_A\left[I(I+1) + I_A(I_A+1) - I_B(I_B+1)\right]}{I(I+1)} \\ &+ \frac{g_B\left[I(I+1) + I_B(I_B+1) - I_A(I_A+1)\right]}{I(I+1)} = \\ &= \frac{1}{2}(g_A + g_B) + \frac{1}{2}(g_A - g_B)\frac{I_A(I_A+1) - I_B(I_B+1)}{I(I+1)} \end{aligned} \tag{1.16}$$

which is called the additivity relation (also known as 'addition theorem').

It is useful to mention that, if the two groups A and B have the same value of the g-factors and the spins (for example two unpaired nucleons on the same orbital), the second part in formula 1.16 vanishes, thus the g-factor of such a configuration is independent on the total spin to which this two groups are coupled.

1.3   Nuclear orientation

For most methods to measure nuclear magnetic moments, it is essential to obtain an ensemble of oriented nuclear states prior to the measurement. A schematic picture of the notations of the nuclear states in the production and measurement process can be found in Fig. 1.3.
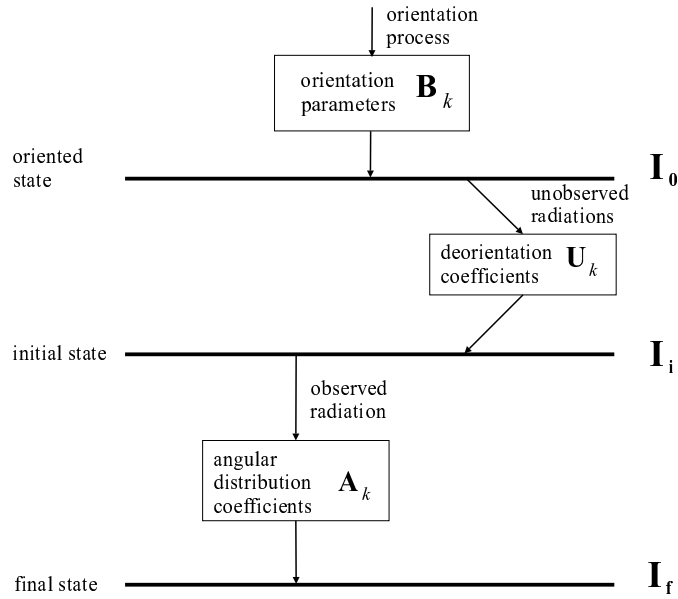
Figure 1.3: *Schematic diagram with the nuclear states and the parameters describing the angular distribution measurement of an oriented nuclear ensemble.*

The original oriented state, denoted I_0 is the parent state of the nuclear radioactive decay. The initial and the final states, connected by

the observed radiation, are denoted I_i and I_f, respectively. The initial oriented state is usually described by the orientation parameters B_k or, in the case of lack of axial symmetry, by the more general statistical tensor ρ_q^k. If there is an unobserved intermediate transition between the oriented parent state and the initial state, the effective orientation of the state I_i is determined by the initial orientation of the state I_0, modified by the deorientation coefficients U_k, which depend on the properties of the unobserved radiation.

In general, the angular distribution of the radiation, emitted from an oriented state of spin I_i, is described by [Kra86]

$$W(\theta, \phi) = \sqrt{4\pi}\sqrt{2I_i + 1} \sum_{k,n} \frac{\rho_n^{k*}(I_i) A_k Y_{kn}(\theta, \phi)}{\sqrt{2k + 1}} \qquad (1.17)$$

where ρ_n^k is the statistical tensor; $Y_{kn}(\theta, \phi)$ are the spherical harmonics; the angles θ and ϕ determine the direction of the emission of the radiation with respect to the orientation axis. In this expression we have assumed that the linear polarization of the emitted radiation is not observed.

If the oriented state is *axially symmetrical*, then only the $n = 0$ components of the statistical tensor ρ_n^k are not vanishing, which changes expression (1.17) to

$$W(\theta) = \sum_k B_k(I_i) A_k P_k(cos\theta), \qquad (1.18)$$

where $P_k(cos\theta)$ are the Legendre polynomials and we have used the relation between the statistical tensor and the orientation parameters

$$\rho_n^k(I_i) = \frac{1}{\sqrt{2I_i + 1}} B_k(I_i)\delta_{n0} \qquad (1.19)$$

To describe the orientation of an oriented ensemble of nuclei in general, we use the statistical tensor, which can be derived using the density matrix of the oriented state via the relation

$$\rho_n^k(I_i) = \sqrt{2k + 1} \sum_{m,m'} (-1)^{I_i + m'} \begin{pmatrix} I_i & I_i & k \\ -m' & m & n \end{pmatrix} \langle I_i m|\rho|I_i m'\rangle \quad (1.20)$$

In the case of axial symmetry of the orientation, the density matrix ρ is diagonal in a representation in which the z-axis is chosen as the symmetry axis. Thus only $n = 0$ elements of the statistical tensor are different from zero. In such a case, the diagonal elements of ρ are the population

parameters $p(m)$ of the nuclear magnetic substates and equation (1.20) becomes

$$\rho_0^k(I_i) = \sqrt{2k+1} \sum_m (-1)^{I_i+m} \begin{pmatrix} I_i & I_i & k \\ -m & m & 0 \end{pmatrix} p(m) \qquad (1.21)$$

Using the relation (1.19), we get for the orientation parameters

$$B_k(I_i) = \sqrt{2k+1}\sqrt{2I_i+1} \sum_m (-1)^{I_i+m} \begin{pmatrix} I_i & I_i & k \\ -m & m & 0 \end{pmatrix} p(m) \quad (1.22)$$

If the $p(m)$ are normalized ($\sum p(m) = 1$), then $B_0 = 1$. From the properties of the $3j$ symbols, it follows that B_k identically vanishes for $k > 2I_i$, which sets the limits of the summations in eqs. (1.17) and (1.18).

Often, terms like isotropic distribution, polarization and alignment are used. They can be described as follows:

$$isotropic\ distribution \quad : \quad p(m) = \frac{1}{2I+1} \ \ \text{for all } m; B_k = 0\ (k \neq 0) \qquad (1.23)$$

$$polarization \quad : \quad p(m) \neq p(-m); B_k \neq 0 \text{ for odd } k \qquad (1.24)$$

$$alignment \quad : \quad p(m) = p(-m); B_k = 0 \text{ for odd } k \qquad (1.25)$$

and, furthermore, we can distinguish between two different types of alignment:

$$prolate\ alignment: \quad B_2 \ > \ 0 \qquad (1.26)$$

$$oblate\ alignment: \quad B_2 \ < \ 0 \qquad (1.27)$$

A schematic drawing of the different types of orientation can be found in Fig. 1.4.

In β-decay, due to the parity violation of the weak interaction, we are sensitive to the polarization of the nuclear ensemble. The angular distribution of γ-radiation is symmetrical with respect to $\theta = \pi/2$, so that for γ-radiation, we are only sensitive to the alignment of the nuclear ensemble. Taking into account these differences, we will consider the two cases separately in the following subsections.
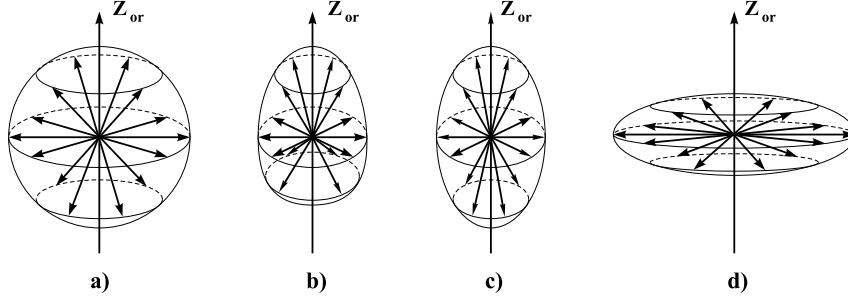
Figure 1.4: *Schematic drawing of a non-oriented (a), polarized (b), and aligned (prolate - c and oblate - d) nuclear ensembles.*

1.3.1 Nuclear orientation observed via γ-radiation

For mixed multipolarity γ-transitions one can write

$$A_k(\lambda\lambda' I_f I_i) = \frac{1}{1+\delta^2}[F_k(\lambda\lambda I_f I_i) + 2\delta F_k(\lambda\lambda' I_f I_i) + \delta^2 F_k(\lambda'\lambda' I_f I_i)] \quad (1.28)$$

where $F_k(\lambda\lambda' I_f I_i)$ is defined as

$$
\begin{aligned}
F_k(\lambda\lambda' I_f I_i) &= (-1)^{1+I_i+I_f}\sqrt{(2\lambda+1)(2\lambda'+1)(2I_i+1)(2k+1)} \\
&\times \begin{pmatrix} \lambda & \lambda' & k \\ -1 & 1 & 0 \end{pmatrix} W(\lambda\lambda' I_i I_i; kI_f) \quad (1.29)
\end{aligned}
$$

λ is the multipolarity of the γ-radiation and $W(\lambda\lambda' I_i I_i; kI_f)$ is a Racah coefficient, and δ is the mixing ratio defined as

$$\delta^2 = \frac{\text{intensity of } \lambda'}{\text{intensity of } \lambda} = \frac{T(\lambda')}{T(\lambda)} \quad (1.30)$$

The sign of δ depends on the relative phase of the two reduced matrix elements, and is thus related to the relevant nuclear wave functions. If a pure transition is observed then, $\lambda = \lambda'$.

Successive propagation of the orientation

Usually, in a nuclear orientation measurement we do not observe the radiation from the initially oriented state I_0 but from states somewhere further in the cascade (see Fig. 1.3). Usually, also more than one path to

get from the oriented state I_0 to the initial state I_i is available. Therefore, the orientation parameters (B_k) for the initial state I_i, are expected to be smaller than the orientation of the parent state I_0 [Mor76]

$$B_k(I_i) \quad = u_k(I_0 \lambda I_i) B_k(I_0)$$

where

$$u_k(I_0 \lambda I_i) \quad \equiv (-1)^{\lambda + k - I_0 - I_i} \sqrt{(2I_0 + 1)(2I_i + 1)} W(I_0 I_0 I_i I_i; k\lambda) \quad (1.31)$$

In the case of a mixed-multipolarity transition, the expression (1.31) is modified to

$$B_k(I_i) = B_k(I_0) \left\{ \frac{1}{1 + \delta^2} u_k(I_0 \lambda I_i) + \frac{\delta^2}{1 + \delta^2} u_k(I_0 \lambda' I_i) \right\} \qquad (1.32)$$

1.3.2   Nuclear orientation observed via β-decay

The Hamiltonian of the weak interaction is rather complex. Therefore, the nuclear orientation formalism for β-decay is much more complicated, than that for γ-decay. To simplify the picture, we will make several assumptions:

- the interaction is of pure V - A (vector minus axial-vector) type, with maximal parity violation;

- time reversal invariance;

- the neutrino is massless with velocity c and fixed helicity;

- we consider only the lowest order multipole contributions to the Hamiltonian - allowed and first-forbidden decays.

Allowed β-decay

In allowed β-decay, the two particles (β-particle and neutrino) do not carry angular momentum L. Their spins add up either to 0 (Fermi) or to 1 (Gamow-Teller). Thus the selection rules for allowed β-decay are

$$I_i - I_f = 0, \pm 1 \qquad \text{and} \qquad \pi_i = \pi_f. \qquad (1.33)$$

If $I_i = I_f = 0$, only the Fermi (vector) matrix element contributes to the decay and no anisotropy can be observed.

For $I_i - I_f = \pm 1$, only the Gamow-Teller (GT) matrix element contributes. In such a case the angular distribution becomes [Van86]

$$W_{\beta^\pm}(\theta) = 1 + A_1(\beta^\pm)B_1(I)cos\ \theta \qquad (1.34)$$

where the angular distribution coefficients are defined as

$$A_1(\beta^\pm) = \begin{cases} \mp\frac{v}{c}\sqrt{\frac{I_i+1}{3I_i}} & \text{for} & I_f = I_i - 1 \\ \pm\frac{v}{c}\sqrt{\frac{I_i}{3(I_i+1)}} & \text{for} & I_f = I_i + 1 \end{cases} \qquad (1.35)$$

In the case of $I_f = I_i \neq 0$, mixed Fermi - Gamow-Teller decay may occur with the mixing ratio defined as

$$y = \frac{C_V M_F}{C_A M_{GT}} \qquad (1.36)$$

where C_V and C_A are respectively the vector and axial-vector coupling constants of the weak interaction and M_F and M_{GT} are the Fermi and Gamow-Teller matrix elements. In this case the angular distribution coefficient becomes

$$A_1(\beta^\pm) = \frac{v/c}{1+y^2}\left\{\frac{\mp 1}{\sqrt{3I(I+1)}} + \frac{2}{\sqrt{3}}y\right\} \qquad (1.37)$$

First-forbidden β-decay

In first-forbidden β-decay, the two particles carry away an orbital angular momentum $L = 1$, which imposes the selection rules:

$$I_i - I_f = 0, \pm 1, \pm 2 \qquad \text{and} \qquad \pi_i = -\pi_f \qquad (1.38)$$

Due to the orbital angular momentum ($L = 1$) carried away in first forbidden β-decay, the situation becomes much more complex with six different matrix elements contributing to the decay. The total angular momentum of a β-particle can be coupled to a maximum value of $J = 3/2$. Therefore, it gives, in principle, rise to three different angular distribution coefficients $A_1(\beta^\pm)$, $A_2(\beta^\pm)$ and $A_3(\beta^\pm)$. The A_1 and A_3 coefficients are associated with parity non-conserving terms, while A_2 is associated with terms deriving from the orbital angular momentum $L = 1$ carried away by the β-particle.

The A_1 coefficient of the first-forbidden β-decay with $I_i - I_f = 0, \pm 1$ obeys the same expression as for allowed β-decay with certain changes

of the matrix elements (see [Van86]). Therefore, the same behaviour is expected for the β-asymmetry, namely, full asymmetry for $I_i - I_f = \pm 1$ and an interference term for the $I_i - I_f = 0$ case.

The A_2 coefficient of a first-forbidden β-decay can be observed only if there is some alignment present in the nuclear spin-oriented ensemble ($B_2 \neq 0$). For the case of $I_i - I_f = 0, \pm 1$, the $A_2(\beta)$ can be found in [Van86].

The A_3 coefficient is expected to be negligible for decays with $I_i - I_f = 0, \pm 1$.

For the special case of first-forbidden β-decay if $I_i - I_f = \pm 2$, there is only one matrix element contributing to the decay and the angular distribution coefficients are uniquely determined

$$A_1(\beta^{\pm}) = \pm \frac{p}{E}\frac{q^2 + 0.6p^2}{q^2 + p^2}F_1(I_f 2 2 I_i) \tag{1.39}$$

$$A_2(\beta^{\pm}) = \frac{p^2}{q^2 + p^2}F_2(I_f 2 2 I_i) \tag{1.40}$$

$$A_3(\beta^{\pm}) = \pm \frac{p}{E}\frac{p^2}{q^2 + p^2}F_3(I_f 2 2 I_i) \tag{1.41}$$

where p and q are the momenta of the β-particle and the neutrino, respectively, and E is the energy of the β-particle.

1.3.3 Nuclear orientation produced in projectile - fragmentation reactions

The spin-oriented nuclear ensemble, which is one of the necessities for most of the methods of nuclear-moments measurements, can be obtained by several means. The methods to produce an oriented ensemble of nuclei can be divided in two major groups: a) orientation obtained from the reaction mechanism via which the nuclear state under investigation is produced and b) orientation of the nuclear spins via their interaction with the surrounding environment after the production of the nuclear state.

One of the oldest methods to produce polarized nuclear spins is the *low temperature nuclear orientation* [Pos86]. It is based on the interaction of the nuclear spins with a very strong magnetic field (of the order of a few T; usually a ferromagnetic host is used) at very low temperature (mK). At such conditions, the Boltzmann distribution of the nuclear spin ensemble causes a different population of the magnetic sub-levels, which,

as a result creates a polarized ensemble. Other methods from group *b*) are those using the interaction of the atomic spins with the nuclear spins. One of these methods is the *tilted-foil polarization* [Ber82b] where, after the passage of the ions through a stack of foils, tilted under an angle with respect to the beam, and using the interaction between the atomic and the nuclear spins, one can obtain a polarized nuclear ensemble. Another method is the *optical pumping* [Arn88, Arn92] where, after multiple absorption and spontaneous emission of photons, one can orient the atomic spins and transfer this orientation to the nuclear ensemble. A further example of orientation produced via the interaction between the atomic and nuclear spins is the use of polarized laser light in a two-step resonant ionization process [Ney97b]. This technique has not been applied yet experimentally for nuclear orientation.

On the other hand, one can obtain an oriented ensemble directly in the production process of the nuclear state. Such an example is the alignment obtained in a fusion-evaporation reaction and also the alignment and/or polarization after a projectile-fragmentation reaction. For the experiments described in this work, we used projectile-fragmentation reactions for the production and the orientation of the nuclear states under investigation. Therefore, in the following section we will try to give a schematic picture of the mechanisms leading to spin orientation in a projectile-fragmentation reaction [Cou99].

In a projectile-fragmentation reaction (the schematic drawing is given in Fig. 1.5), we have a projectile nucleus, impinging on a target, with typical energy from a few tens of MeV/u up to a few GeV/u. As outgoing products of the reaction we obtain a fragment (being part of the projectile nucleus) and some abrazed nucleons. The mass of the produced nuclei can vary from the very light masses up to the very heavy ones, depending on the mass of the primary beam and it is usually smaller than the mass of the projectile. Due to the very high energy of the impinging nuclei, they are not going to fuse with the target nuclei (as in the case of a fusion-evaporation reaction). We can divide the process that occure in two different regimes, depending on the energy. For relativistic energies (from 200 MeV/u to a few GeV/u), the dominating process is the peripheral reaction or abrasion. A simple picture for this type of reaction is the participant spectator model [Gol78, Fri83, Huf81]. This supposes that the target nuclei are an abrazing part of the projectile nucleus (the abrased part is called "participant") and the rest of the projectile (the fragment) flies away with a velocity similar to the one of the primary beam and with a very small angular divergence. The fragment part is
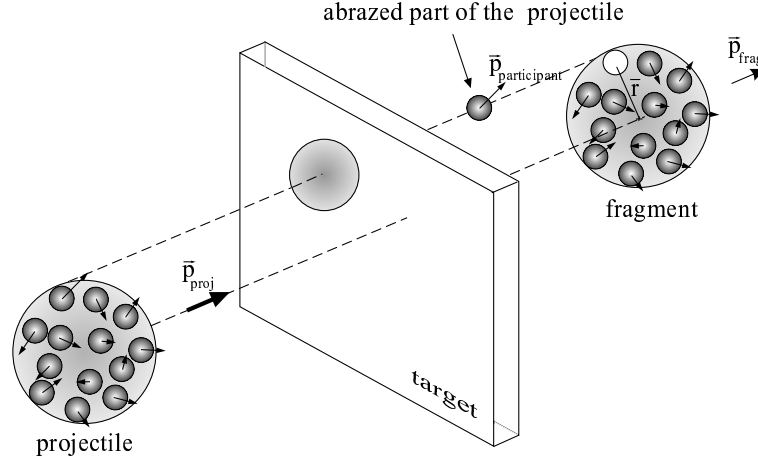
Figure 1.5: *Schematic drawing of the projectile-fragmentation reaction.*
$\vec{p}_{proj}$ *is the momentum of the impinging projectile;* $\vec{p}_{participant}$ *is the momentum of the abrazed nucleons (considered as one part);* $\vec{p}_{frag}$ *is the momentum of the outgoing fragment and* $\vec{r}$ *is the radius-vector between the center of the fragment and the position of the abrazed part before the reaction. The picture is taken from [Cou99]*

called "the spectator" because in the reaction model it does not play an active role.

For energies between 30 MeV/u and 200 MeV/u (intermediate energies), this description is still valid [Mor89]. However, the reaction mechanism is not so simple (it stays somewhere between the transfer reaction at low energy and the pure fragmentation at high energy).

In these models, the momentum transfer to the spectator nucleus is very small as well as the angular momentum transfer. Thus, the probability to obtain a preferential direction of the fragment spins seems very small. It was found experimentally [Asa90, Asa92, Oku93] that, if the secondary fragment beam is selected under a small angle with respect to the primary beam, the nuclear spins of the fragments can be polarized. A beam swinger, usually consisting of two magnets, is used for the selection of the fragments under an angle [Uen96]. This is a magnet with its field in the vertical direction, which deviates the primary beam just before it is impinging on the target (see Fig. 1.6 b)).
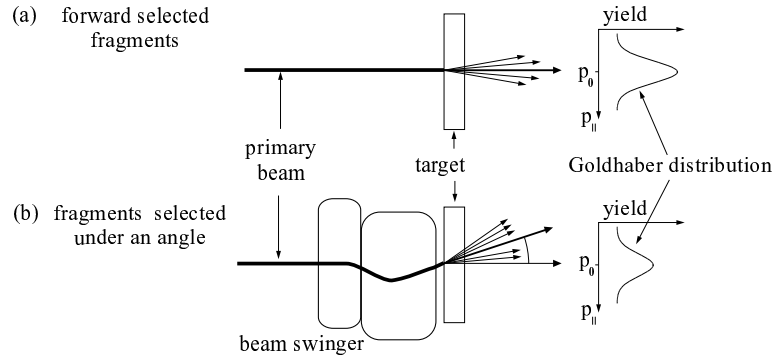
Figure 1.6: *a) Forward selected fragments. b) Fragments selected under an angle α.*

If the fragments are selected in the forward direction (Fig. 1.6 a)), one can obtain an aligned ensemble in the reaction [Asa91, SO94, Ney97a]. Furthermore it was theoretically derived [Asa92], that it is impossible to obtain polarization of the nuclear ensemble in the forward selected fragment beam. In both of these cases, the reaction yield varies as a function of the longitudinal momentum of the fragments. This variation has a Gaussian distribution which is also called Goldhaber distribution [Gol74]. The position of the maximum is determined by the momentum p_0 and the width of the distribution is given by

$$\sigma = \sigma_0 \sqrt{A_f(A_p - A_f)/(A_p - 1)} \qquad (1.42)$$

A_f and A_p are the masses of the fragment and the projectile, respectively, and $\sigma_0 \approx 90 MeV/c$ [Gol74]. The orientation models in projectile-fragmentation reactions are still qualitative and further investigations are needed for the full understanding of the processes.

Alignment

To obtain an aligned ensemble of nuclei in a projectile-fragmentation reaction, we have to select the reaction products flying in a forward direction. The spin orientation can be qualitatively described in the participant spectator model [Asa91]. In this model, it is supposed that the spectator part of the projectile, which will actually form the fragment itself, is not disturbed in the reaction. This means that the momentum,
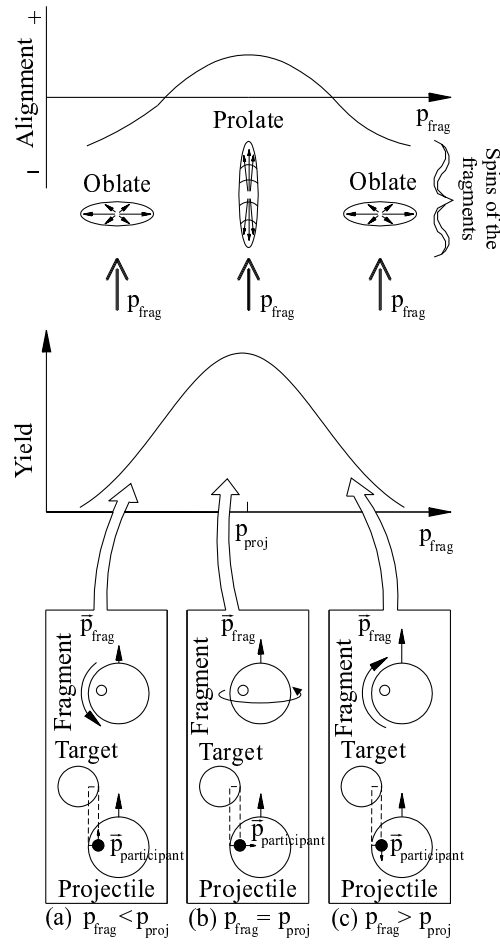
Figure 1.7: *A qualitative picture of the alignment obtained in a projectile-fragmentation reaction in the participant spectator model [Asa91]. The alignment as a function of the fragment's momentum $|\vec{p}_{frag}|$, is shown for three different cases: (a) $|\vec{p}_{frag}| < |\vec{p}_{proj}|$, (b) $|\vec{p}_{frag}| \simeq |\vec{p}_{proj}|$ and (c) $|\vec{p}_{frag}| > |\vec{p}_{proj}|$. $p_{frag} = |\vec{p}_{frag}|$ and $p_{proj} = |\vec{p}_{proj}|$ are the longitudinal projections of the fragment and the projectile momenta, respectively. (picture from [Cou99])*

$\vec{p}_{frag}$, and the angular momentum, $\vec{I}$, of the fragment are the corresponding values of the "spectator" part. Thus taking into account the momentum conservation in the projectile-rest frame, we can write

$$
\begin{aligned}
\vec{p}_{before} &= \vec{p}_{after} \\
\vec{p}_{proj} &= \vec{p}_{frag} + \vec{p}_{participant}
\end{aligned}
\tag{1.43}
$$

The angular momentum conservation law gives

$$
\begin{aligned}
\vec{I}_i &= \vec{I}_f + \vec{l}_{react} \\
\vec{0} &= \vec{I}_f + \vec{r} \times \vec{p}_{participant}
\end{aligned}
\tag{1.44}
$$

where $\vec{r}$ is the radius-vector of the participant part and $\vec{p}_{participat}$ is the momentum of the participant part in the projectile-rest frame.

This model describes the change in the initial alignment (A) of the nuclear spins as a function of the fragment's momentum ($\vec{p}_{frag}$). The amount of the alignment is positive if $p_{frag} = p_{proj}$ and it becomes smaller and changes sign with p_{proj} moving further away from p_{frag}. We can explain this behaviour as shown in Fig. 1.7 where a peripheral collision is assumed. Taking away one or several nucleons from the projectile, which are moving inside the projectile parallel to the beam ($\vec{p}_{participant} \| \vec{p}_{proj}$), corresponds to a decrease of the momentum of the fragment $|\vec{p}_{frag}| < |\vec{p}_{proj}|$ (Fig. 1.7(a)). In this case, a nucleon with an angular momentum $\vec{r} \times \vec{p}_{participant}$ is removed and, therefore, an angular momentum $\vec{I}_f = -\vec{r} \times \vec{p}_{participant}$ is created, which is perpendicular to the beam axis. This gives rise to a negative alignment ($\vec{I}_f \perp$ symmetry axis). Similar arguments are also valid for the $|\vec{p}_{frag}| > |\vec{p}_{proj}|$ case (Fig. 1.7(c)). On the other hand, in the case of $|\vec{p}_{frag}| = |\vec{p}_{proj}|$, the removed nucleons have their momentum perpendicular to the projectile's momentum ($\vec{p}_{participant} \perp \vec{p}_{proj}$), thus $\vec{r} \times \vec{p}_{participant}$ is parallel (or antiparallel)to the beam axis. This gives rise to a positive alignment ($\vec{I} \|$ symmetry axis) (Fig. 1.7(b)).

Polarization

The mechanism of creation of polarization in a projectile-fragmentation reaction can also be described in the participant spectator model (see Fig. 1.8) [Asa92, Oku93]. Similar to the description of the alignment, the polarization in a projectile-fragmentation reaction also changes as function of the fragment's momentum $\vec{p}_{frag}$. We can understand this
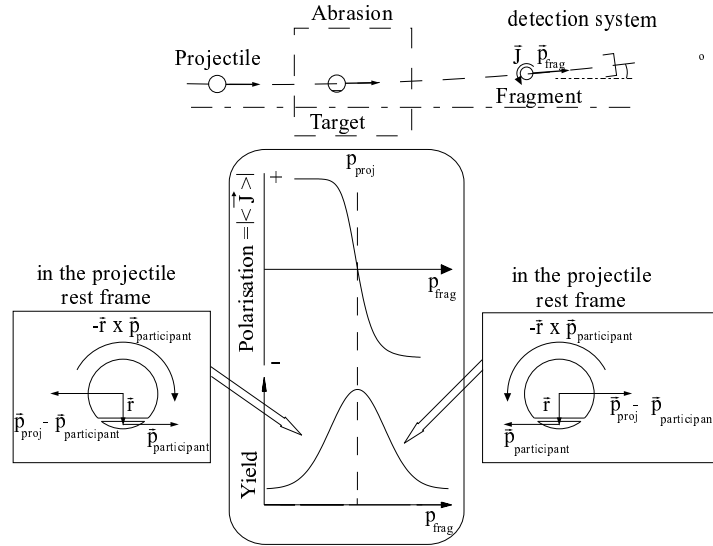
Figure 1.8: *A schematic drawing of the mechanism to obtain polarization in a projectile-fragmentation reaction [Asa92, Oku93]. The polarization is presented as a function of $|\vec{p}_{frag}|$ in three different cases: $|\vec{p}_{frag}| < |\vec{p}_{proj}|$, $|\vec{p}_{frag}| \simeq |\vec{p}_{proj}|$ and $|\vec{p}_{frag}| > |\vec{p}_{proj}|$. (picture from [Cou99])*

dependence using eqs. (1.43) and (1.44). If, during the reaction, a participant part with its momentum parallel to the beam axis is removed from the projectile, then the fragment's momentum is decreased. The removed part obtains an angular momentum $\vec{r} \times \vec{p}_{participant}$ and the fragment obtains an angular momentum $\vec{I} = -\vec{r} \times \vec{p}_{participant}$. If the participant part has its momentum parallel to the beam axis, this creates a negative polarization ($P < 0$). In the same way, if the participant part has its angular momentum anti-parallel to the beam direction, the created polarization is positive ($P > 0$). In the above presented arguments, we assumed that a near-side removal takes place (Fig. 1.9). If a far-side removal occurs, this will change the sign of the obtained
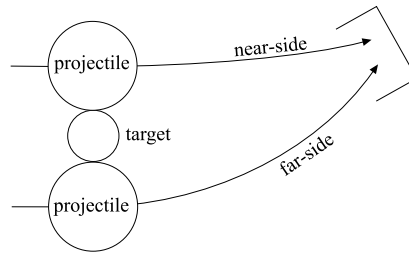

Figure 1.9: *An illustration of near- and far-side trajectories.*

polarization. Which of these two processes will be superior, depends on the dominant interaction between the projectile and the target nuclei (Coulomb repulsion or nuclear attraction). This can be changed by changing the masses of the projectile and the target nuclei. For light target nuclei, the fragmentation most probably will follow the far-side scheme due to the relative weakness of the Coulomb repulsion compared to the nuclear attraction. For heavier target nuclei, the near-side scheme should take over because the Coulomb repulsion becomes stronger. In an intermediate regime, it is possible to observe some transitional effects [Asa92, Oku93].

In summary we can say that one can obtain an aligned as well as a polarized nuclear ensemble in a projectile-fragmentation reaction. It is important to mention that, for the polarization (in certain circumstances also for the alignment), the maximum of the production yield does not coincide with the maximum of the spin-orientation. Moreover, to create a polarized ensemble, one has to select the outgoing fragments under an angle which additionally decreases the production of the nuclei
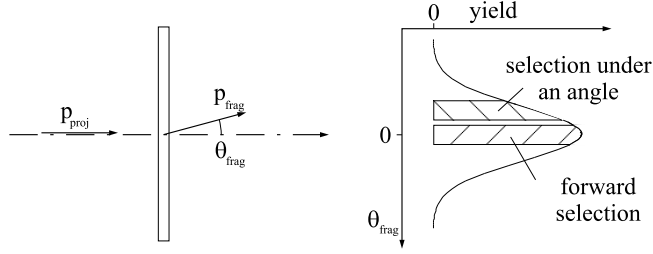
Figure 1.10: *In a projectile-fragmentation reaction, most of the nuclei are emitted in the forward direction ($\theta_{frag} = 0^o$). An increase of the selection angle ($\theta_{frag} \neq 0^o$) leads to a decrease of the production rate [Gol74]. (picture from [Cou99])*

of interest (Fig. 1.10). We also have to say that all models are still qualitative and do not necessarily reproduce the observed orientation in a projectile-fragmentation reaction. Further investigations are needed to fully understand the orientation process.

1.4 Interaction of an oriented nuclear ensemble with an external magnetic field

Let us consider an ensemble of nuclei which are immersed in an external magnetic field. Due to the interaction of the nuclear spins with the magnetic field, the degeneracy of the magnetic substates is removed and the energy difference between the different substates is given by the Hamiltonian:

$$H = -\vec{\mu}\vec{B} = \vec{\omega}_L \hbar \vec{I} \qquad (1.45)$$

where $\vec{B}$ is the magnetic field strength and

$$\vec{\omega}_L = -\frac{g\mu_N}{\hbar}\vec{B} \qquad (1.46)$$

is referred to as the Larmor frequency. In a semiclassical manner, we can represent the picture as a rotation of the nuclear spin vector around the magnetic field with frequency $\vec{\omega}_L$. If the nuclear ensemble is oriented, then we can consider the orientation axis rotating around the magnetic field, assuming that they are not parallel. The dependence of the Larmor

frequency on the g factor of the nuclear state (1.46) is used in experimental techniques to measure the g factor of a nuclear state, such as the Time Dependent Perturbed Angular Distribution (TDPAD) technique or the Nuclear Magnetic Resonance. As both are used in the present work, we will examine them in more detail.

1.4.1 Time Dependent Perturbed Angular Distribution

Let us consider the case when an isomeric nuclear state is populated and simultaneously oriented by a nuclear reaction. The symmetry axis of the aligned nuclear ensemble is parallel to the direction of the beam. The angular distribution of the γ-radiation, produced in the decay of the excited states, is anisotropic for states with spin $I \geq 1$. The details of this angular distribution (eqn. 1.18) depend on the nuclear alignment, the nuclear spins of the levels involved and the multipolarity of the γ-radiation.

Let us now suppose that the nuclear ensemble is immersed in a magnetic field, which is applied perpendicular to the orientation axis. In the further discussions we will assume that the magnetic field is in vertical direction and the orientation axis of the nuclear ensemble in the horizontal plane (an usual case in a TDPAD experiment). This external field will cause a precession of the nuclear magnetic moment, and, hence, a rotation of the angular distribution of the γ-radiation, around the magnetic field with a frequency, equal to the Larmor frequency.

The γ-ray intensity, detected in the horizontal plane at some angle θ with respect to the beam axis, will vary in time according to

$$I(t, \theta, B) = I_0 e^{-t/\tau} W(t, \theta, B) \qquad (1.47)$$

where I_0 is the intensity at time $t = 0$, τ is the life time of the radioactive γ-decay and $W(t, \theta, B)$ is an oscillating term due to the rotating angular distribution. In the case of axially symmetrical ensemble of nuclei we can simplify the general angular distribution formula (1.17) and rewrite it in the form:

$$W(t, \theta, B) = \sum_k B_k A_k(\gamma) P_k[cos(\theta - \omega_L t - \alpha)] \qquad (1.48)$$

Here B_k are the orientation parameters (eqn. 1.22), depending on the degree of alignment produced in the nuclear reaction; A_k are the angular

distribution coefficients (eqn. 1.28) depending on the details of the γ-decay; θ is the angle, with respect to the beam axis, at which the γ-ray intensity is measured (in the horizontal plane) and α is the angle between the orientation and the beam axes. Since we are considering here a γ-decaying isomeric state, only even-k terms will enter in eqn. 1.48. For most cases, the product $A_k B_k$ is negligible for $k \geq 4$, thus, to a good approximation, only second order terms $[B_2(I)$ and $A_2(\gamma)]$ have to be considered for the angular distribution.

The nuclear g factor can be extracted from the ratio of the intensity measurements at two different angles θ and $\theta + \pi/2$

$$R(t,\theta,B) = \frac{I(t,\theta,B) - \epsilon I(t,\theta + \pi/2,B)}{I(t,\theta,B) + \epsilon I(t,\theta + \pi/2,B)}$$

$$(1.49)$$

where ϵ is the relative efficiency of the two detectors. After using eqs. 1.48 and 1.47 we obtain the final formula for the $R(t,\theta,B)$ function:

$$R(t,\theta,B) = \frac{3A_2B_2}{4 + A_2B_2}cos[2(\theta - \omega_L t - \alpha)] \qquad (1.50)$$

Initial phase of the oscillation pattern

An important issue for a TDPAD measurement is the direction of the orientation axis of the nuclear ensemble at the starting moment, t = 0, which is usually the moment of implantation. It determines the phase of the oscillations and it is an additional fit parameter which also depends on the g factor.

In the case of a fusion-evaporation reaction, the produced nuclear species are usually stopped in the production target, so that the orientation axis coincides with the beam axis. In some cases, the nuclear state under investigation is transported through an in-flight mass spectrometer to an implantation host (like in the case of a projectile-fragmentation reaction). The magnetic moment of the nuclear state will interact with the field of the dipole magnets. Due to this interaction, the angle between the orientation axis and the beam is different from zero at the exit of the spectrometer.

When an ion with mass Am_N, charge Qe and velocity $\vec{V}$ is passing through a magnetic field $\vec{B}$, its momentum vector $\vec{p}$ is precessing due to the Lorentz force

$$\vec{F}_L = Qe\vec{V} \times \vec{B} \qquad (1.51)$$
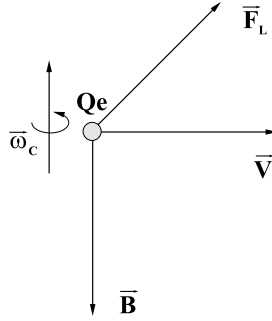
Figure 1.11: *Direction of the Lorentz force and the cyclotron frequency of a positively charged ion passing through a magnetic field.*
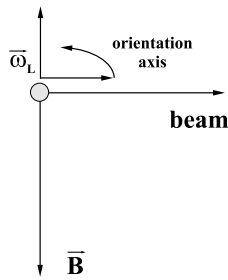
Figure 1.12: *Rotation of the orientation axis of a nuclear ensemble passing through a magnetic field.*

with a cyclotron frequency

$$\vec{\omega}_C = -\frac{Qe\vec{B}}{Am_N} \tag{1.52}$$

where the negative sign reflects the relative direction of the cyclotron frequency ω_C and the magnetic field for positively charged ions (see Fig. 1.11)

At the same moment, due to the Larmor precession of the nuclear spins, the orientation axis of the nuclear ensemble is rotating with $\vec{\omega}_L$ (1.46) in a plane perpendicular to the magnetic field (see Fig. 1.12). Thus, after passing through the spectrometer, the momentum vector of

the ions is deviated from the initial beam direction at an angle θ_C and the deviation of the orientation axis from its initial direction is θ_L (Fig. 1.13). The relation between the two angles is given by

$$\theta_L = \theta_C \frac{\omega_L}{\omega_C}$$

$$\theta_L = \theta_C \frac{g\mu_N}{\hbar} \frac{Am_N}{Qe} = \theta_C \frac{gA}{2Q}. \tag{1.53}$$

Finally, the angle α between the orientation axis of the nuclear ensemble and the momentum vector $\vec{p}$ of the ions coming out from the spectrometer is $\alpha = \theta_L - \theta_C$, defined such that the Z axis is in vertical direction and looking upwards:

$$\alpha = -\theta_C \left(1 - \frac{gA}{2Q}\right) \tag{1.54}$$

α depends on the direction of the magnetic field of the dipole magnets of the spectrometer and also on the sign of the g factor.
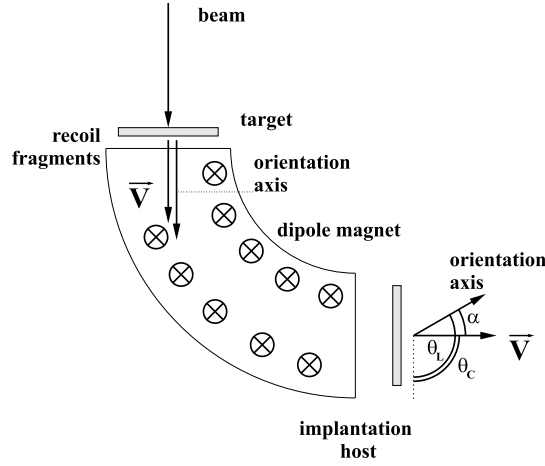

Figure 1.13: *Deviation of the orientation axis from the beam axis after passing of the ions through a spectrometer.*

Sign (un)determination of the g factor

In a TDPAD experiment there are certain setup configurations, at which the determination of the sign of the g factor appears to be impossible. This is a consequence of the internal symmetry of the setup, combined with the symmetry for the spin-oriented ensemble.

To make this clearer, we will have to recall the formula for the $R(t)$ function 1.50 and make therein the explicit substitution of the initial phase of the oscillations (eqn. 1.54), which will lead us to the following expression:

$$R(t, \theta, B) = \frac{3A_2B_2}{4 + A_2B_2} cos \left\{ 2(\theta + \theta_C) - 2g \left(\frac{\theta_C A}{2Q} - \frac{\mu_N B t}{\hbar} \right) \right\} \quad (1.55)$$

This is valid for the general case of two detectors, positioned at 90° with respect to each other. Here, the angle θ denotes the position of the first detector and $\theta + 90^o$ is the angle of the second detector, respectively.

Note that, if $(\theta + \theta_C)$ is a multiple of 90° eqn. 1.55 can be written in the form:

$$\begin{aligned} R(t, (n90^o - \theta_C), B) &= \frac{3A_2B_2}{4 + A_2B_2} cos \left\{ n\pi - 2g \left(\frac{\theta_C A}{2Q} - \frac{\mu_N B t}{\hbar} \right) \right\} = \\ &= \pm \frac{3A_2B_2}{4 + A_2B_2} cos \left\{ 2g \left(\frac{\theta_C A}{2Q} - \frac{\mu_N B t}{\hbar} \right) \right\} \quad (1.56) \end{aligned}$$

where the positive sign comes for even n and the negative sign is for odd-n values. Formula 1.56 does not depend on the sign of the g factor, because the *cos* is an even function. Therefore, one cannot determine the sign of the g factor from a TDPAD experiment, in which the sum $(\theta + \theta_C)$ is a multiple of 90°. We have to mention that the deviation angle of the LISE spectrometer at GANIL is $\theta_C = 90^o$.

1.4.2 Nuclear Magnetic Resonance

One of the earliest methods to measure magnetic moments is the Nuclear Magnetic Resonance (NMR) technique initiated in 1946 by Purcell, Torrey and Pound [Pur46]. It was widely used for studies in solid-state physics and afterwards extended towards magnetic moment measurements of radioactive nuclear states. The NMR is based on the application of a radio-frequency field in the presence of a static magnetic field. The

radio-frequency field induces $|\Delta m| = 1$ transitions between the Zeeman-splitted nuclear m-quantum states, if its frequency matches the Larmor frequency ω_L (1.46). If a nuclear state is oriented for a certain period of time, the NMR will destroy the orientation, which produces a change of the angular distribution of the emitted radiation. A comprehensive theoretical description of the radiative detection of NMR was given by Matthias *et al.* [Mat71]. They consider three different experimental techniques that can be combined with NMR: the nuclear orientation (NMR/ON), perturbed angular correlations (NMR/PAC) and angular distributions following nuclear reactions (NMR/NR). Here we are going to discuss only the last option.

Consider a situation when the orientation axis of the nuclear ensemble is parallel to an applied magnetic field. In such a case, even if all spins of the individual nuclei will rotate around the magnetic field, the orientation axis of the nuclear ensemble as a whole will not rotate but will just remain in the direction of the magnetic field. Thus, such a 'holding' magnetic field will preserve the orientation of the ensemble. The Hamiltonian that describes the interaction of the static magnetic field $\vec{B}$ with the magnetic moment $\vec{\mu} = g\vec{I}\mu_N/\hbar$ of the nuclear state has the form [Mat71]:

$$H = -\vec{\mu} \cdot \vec{B} \tag{1.57}$$

H is diagonal (in the "m-basis") if the direction of $\vec{B}$ is chosen as the quantization axis $\vec{z}$, *i.e.*, if $\vec{B} = B\vec{e}_z$ where $\vec{e}_z$ is a unit vector.

Let us now apply also a radio-frequency magnetic field in the plane (XY) perpendicular to the 'holding' magnetic field $\vec{B}$ (see Fig. 1.14) The radio frequency field $\vec{B}_{rf}$ can be represented in the form:

$$\vec{B}_{rf} = B_{rf}\vec{e}_x cos(\omega_{rf}t) + B_{rf}\vec{e}_y sin(\omega_{rf}t) \tag{1.58}$$

which gives for the total magnetic field acting on the system:

$$\vec{B}(t) = B\vec{e}_z + B_{rf}\vec{e}_x cos(\omega_{rf}t) + B_{rf}\vec{e}_y sin(\omega_{rf}t) \tag{1.59}$$

The time dependent Hamiltonian in the laboratory system is then:

$$H(t) = -\frac{g\mu_N}{\hbar} \left\{ BI_z + B_{rf} \left[I_x cos(\omega_{rf}t) + I_y sin(\omega_{rf}t) \right] \right\} \tag{1.60}$$

In order to solve the Schrödinger equation it is convenient to make the transformation from the laboratory system (XYZ) to a rotating system
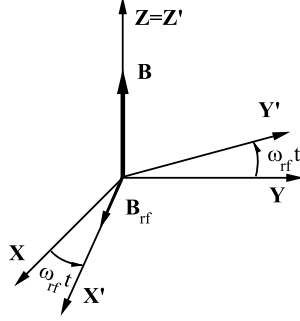
Figure 1.14: *Transformation from the laboratory frame to the rotating frame $X'Y'Z'$.*

$(X'Y'Z')$ (see Fig. 1.14). The Hamiltonian is now time-independently rotating with a frequency ω_{rf} about the Z-axis [Mat71]:

$$H' = -\frac{g\mu_N}{\hbar}\left[(1 - \omega_{rf}/\omega_L)BI_{z'} + B_{rf}I_{x'}\right] \tag{1.61}$$

This Hamiltonian is not diagonal in the m-basis which can be easily seen by observing that $[H', I_{z'}] \neq 0$ because of the presence of $I_{x'}$. H' describes the interaction of the nuclear ensemble with an effective magnetic field $\vec{B}_{eff}$ in the $X'Z'$ plane of the rotating frame:

$$B_{eff} = \sqrt{(1 - \omega_{rf}/\omega_L)^2 B^2 + B_{rf}^2} \tag{1.62}$$

The angle between the effective magnetic field $\vec{B}_{eff}$ and the holding magnetic field is defined by:

$$tan\beta = \frac{B_{rf}}{\left(1 - \frac{\omega_{rf}}{\omega_L}\right)B} \tag{1.63}$$

After a further rotation about Y' under the angle β (Fig. 1.15) we obtain the system $X''Y''Z''$ in which the Hamiltonian is diagonal in the m-bais:

$$H'' = -\frac{g\mu_N}{\hbar}\sqrt{(1 - \omega_{rf}/\omega_L)^2 B^2 + B_{rf}^2}I_{z''} = \omega_{eff}I_{z''} \tag{1.64}$$

As we can see from eqn. 1.63, the angle between the axis around which the nuclear magnetic moment is rotating and the holding magnetic field, depends on the ratio between ω_{rf} and ω_L. The Larmor
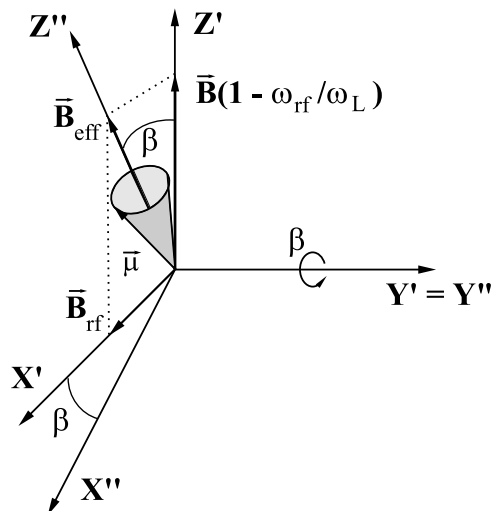
Figure 1.15: *Transformation between the rotating frame $X'Y'Z'$ to the frame $X''Y''Z''$ with $\vec{B}_{eff}$ as Z'' axis.*

frequency depends only on the applied holding magnetic field $\vec{B}$ and the nuclear g factor (1.46) and one can easily change the frequency of the applied RF field. If the two frequencies are equalized, the rotation of the nuclear magnetic moment (the orientation axis of the ensemble) will not be around the holding magnetic field anymore but around an axis perpendicular to it, which is also rotating in the laboratory system. This way, the initial orientation of the nuclear ensemble will be completely destroyed. A resonant change of the angular distribution of the radioactive decay will be observed at the position of $\omega_L = \omega_{rf}$. Provided one knows the strength of the applied holding magnetic field and the frequency of the RF field, the nuclear g factor can be uniquely determined.

Chapter 2

Ground state magnetic moment of ^{32}Cl

2.1   Motivation

The study of nuclei around N = Z, especially as they become further removed from the line of β-stability with increasing mass, has long been an area of great theoretical interest and a testing ground for charge symmetry and charge independence of nuclear forces. Nuclear magnetic moments, particularly in light nuclei, provide a sensitive probe into the single-particle nature of nuclei and the structure of nuclear wave functions. Magnetic dipole moment measurements within isospin multiplets are of particular interest, owing to the first-order similarity of the nuclear structure between members. The roles of protons and neutrons are simply interchanged in two conjugate members of the multiplet, for which the Coulomb force can be neglected in first approximation. The isoscalar and isovector contributions, readily extracted by taking the sum and differences between members of opposite isospin τ_z-projection, provide deeper insight into the structure of the different components of the magnetic moment. This allows us to compare the separate (isoscalar and isovector) components of the magnetic moment to the theoretical calculations. An effective $\overrightarrow{M1}$ operator for the sd shell has been derived by Brown and Wildenthal [Bro87] in an attempt to account for higher order configuration mixing and mesonic exchange currents. Measurements of magnetic moments in the sd shell can serve as a test of the predictive

power of this operator.

Although the ground state magnetic dipole moments for $T = 1/2$ mirror partners have been determined for all bound nuclei up to $A = 41$, only limited magnetic moment information is available for members of $T = 1$ multiplets. The ground state magnetic moments of both the $T_z = +1$ and $T_z = -1$ members of the $T = 1$ multiplet have been experimentally deduced only for $A = 8$, 12, 20, and 36. In the A = 32 system the magnetic moment of ^{32}P is measured and a determination of the magnetic moment of the second member of the multiplet (^{32}Cl) will allow an extraction of the isoscalar and the isovector part of the magnetic moment operator.

Measurements of the magnetic moments of the $T = 1$ multiplets are made difficult by the short half-life and the low production rates for the β-unstable $T_z = +1$ nuclides. With the fast developments in recent years of the radioactive ion beam facilities and the improved radiation detection techniques, more members of these multiplets are becoming reachable for magnetic moment measurement.

These circumstances led to the idea to measure the ground state magnetic moment of ^{32}Cl at the National Superconducting Cyclotron Laboratory (NSCL) of Michigan State University (MSU) with the application of an on-line β-NMR technique on nuclei produced and polarized in an intermediate-energy projectile-fragmentation reaction. The experiment was performed in two stages in the summer and autumn of 1998 and the results will be presented in the following chapter.

2.2   Experimental details and data analysis

2.2.1   Production and selection of ^{32}Cl

A measurement of the ground-state magnetic moment of ^{32}Cl was done using an on-line β-NMR at the NSCL, MSU. A primary beam of ^{36}Ar was accelerated up to 100 MeV/nucleon by the K1200 superconducting cyclotron. A schematic drawing of the experimental devices is shown in Fig. 2.1. The ^{36}Ar ions impinged on a 642 mg/cm^2 ^{93}Nb target at the entrance of the A1200 [She91] fragment separator, which was used to select the secondary beam of interest and to transmit it to the experimental area. The fully stripped ^{32}Cl ions were implanted into a NaCl single crystal, which was mounted at the center of the β-NMR apparatus. Two dipole magnets upstream from the ^{93}Nb target were used to steer the primary beam at an angle of 2.5^o with respect to the
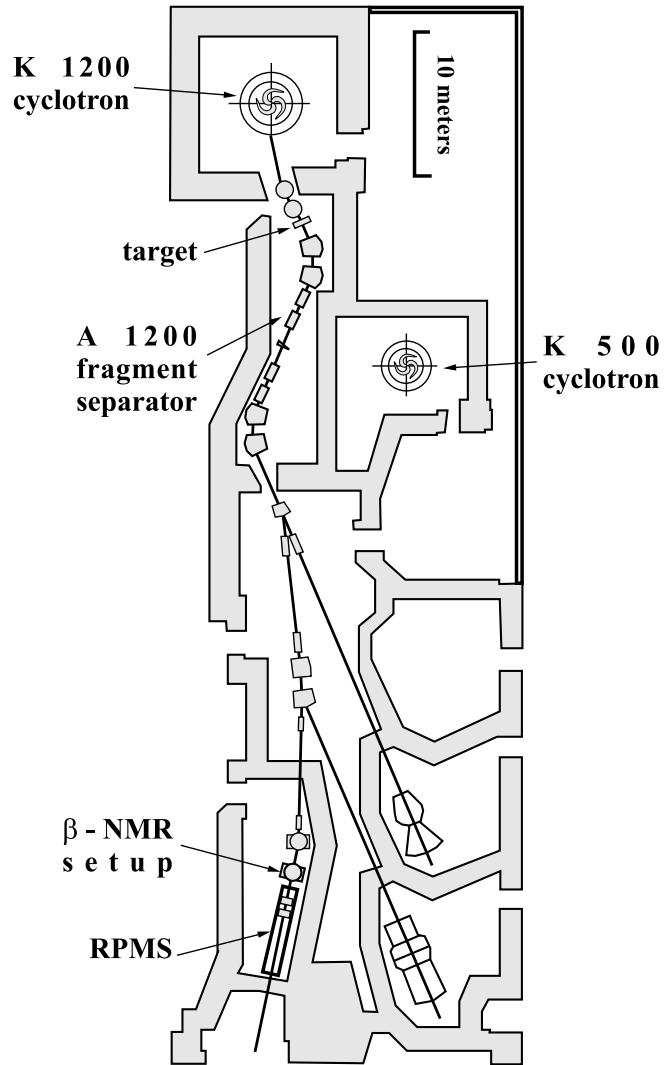
Figure 2.1: *Schematic drawing of the experimental devices at the National Superconducting Cyclotron Laboratory, MSU.*

normal beam axis [Man97] in order to produce a polarized ensemble of nuclei. A 425 mg/cm^2 Al wedge-shaped degrader with a slope angle of 3.5 mrad was placed at the second dispersive image of the A1200 to separate the fragment isotopes with given mass-to-charge ratio based on A and Z. The angular acceptance of the A1200 fragment separator is $\sim 1^o$. The momentum acceptance was set to 1% using the momentum slits placed at the first dispersive image of the device. The center of the momentum distribution was selected.

Under the best conditions, two different nuclides, ^{32}Cl (T$_{1/2}$ = 0.298 s, Q$_{EC}$ = 12.7 MeV, J$^\pi$ = 1$^+$) and ^{31}S (T$_{1/2}$ = 2.572 s, Q$_{EC}$ = 5.4 MeV, J$^\pi$ = 1/2$^+$), were identified in the secondary beam using the fragment energy loss and the time-of-flight information. The ratio of the two nuclides ^{31}S:^{32}Cl at the implantation point was nearly 2:1.

2.2.2 β-NMR on ^{32}Cl

A schematic drawing of the β-NMR setup [Man97] is shown in Fig. 2.2. An electromagnet with pole gap of 10.2 cm provided the holding field in the vertical direction. Two β-telescopes, each consisting of two 4.4 cm × 4.4 cm × 0.3 cm ΔE and a 5.1 cm × 5.1 cm × 2.5 cm E plastic scintillators, were placed between the magnet poles at 0° and 180° with respect to the holding field. Acrylic light guides were used to direct the light from the scintillators to the photomultiplier tubes positioned outside the magnetic field. A 2 mm thick NaCl single crystal with a diameter of 2.5 cm was used as implantation host. Due to its cubic structure, it provided a perturbation-free environment for the implanted radioactive Cl ions, which are expected to occupy a substitutional Cl site in the crystal lattice. Before reaching the NaCl host the secondary beam was passing a 100 μm mylar window and 25 cm of air.

Two RF coils, each of 30-turn loops with a radius of 1.2 cm and a separation of 3 cm, were arranged in a Helmholtz-like geometry around the NaCl crystal. The coil inductance was measured to be 51 μH and they were positioned in such a way that the resulting RF-field was perpendicular both to the applied magnetic holding field and to the direction of the secondary beam.

In order to measure the ground state magnetic moment of ^{32}Cl, we used a continuous implantation of the ^{32}Cl nuclei [Man97] and we measured the β-asymmetry as a function of the frequency of the applied RF field. The RF was switched on and off in intervals of 59.5 s and 60.5 s, respectively. The data-acquisition (DAQ) cycles also consisted of two
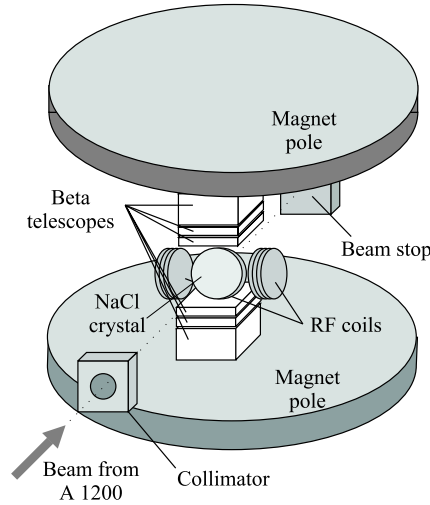
Figure 2.2: *Schematic drawing of the β-NMR setup.*

intervals, RF-on (60 s) and RF-off (60 s). The RF-on application period was 0.5 s shorter than the RF-on DAQ cycle. This allowed for the ^{32}Cl ($T_1/2 = 0.298$s) ions, implanted during the RF-on cycle, to decay during the last 0.5 s of the RF-on DAQ cycle before the RF-off DAQ cycle began. The strength of the RF-field was set to 0.3(1) mT.

Due to the parity violation of the β-decay, the angular distribution of the β-particles (see eqn. 1.34) of a polarized nuclear ensemble is asymmetrical with respect to the orientation axis, which in this case is in the vertical direction. The change in the angular distribution was calculated as the ratio of the counting rates in the 0^o(up) and 180^o(down) β-telescopes. This ratio was measured both for RF-on and RF-off conditions:

$$R = \frac{(up/down)_{RF-on}}{(up/down)_{RF-off}} \tag{2.1}$$

R gives 1 for all points removed from the resonance. Only in the vicinity of the resonance, where the change in the β-asymmetry occurs, this ratio will deviate from 1.

Triple coincidences between β telescopes were used to discriminate against the detection of γ rays. As it was mentioned before two different

$1/2^+$ $t_{1/2}$= 2.572 s

^{31}S

Q_{EC}= 5.4 MeV

3.51 $3/2^+$ 0.01%

3.13 $1/2^+$ 0.03%

1.27 $3/2^+$ 1.09%

0     $1/2^+$ 98.87%   stable

E   **I** ^{31}**P**   **%I** $^+$
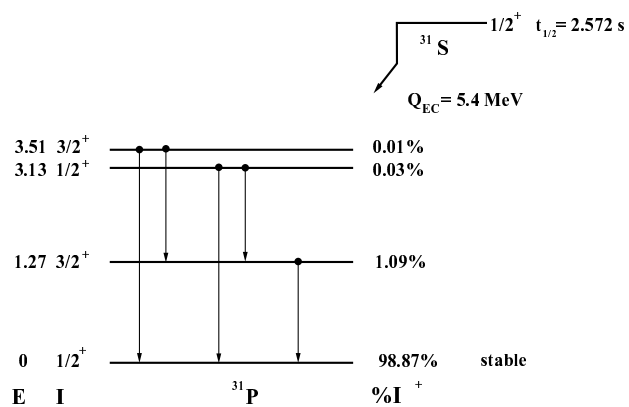
Figure 2.3: *Decay scheme of ^{31}S [Fir96].*

1^+ $t_{1/2}$= 0.298 s

^{32}Cl

Q_{EC}= 12.75 MeV

7.19 1^+ 0.9%

7.12 2^+ 0.5%

7.00 1^+ 20.5%

6.66 $(1,2)^+$ 1.8%

5.55 2^+ 4.1%

                 1.0

4.69 1^+ 6.8%

4.28 2^+ 3.1%

3.78 0^+ 2.6%

0.45   20.5   0.8   2.5   4   3.6

2.23 2^+ 60%

0.4   92   2.8   2.6

         1.6

0   0^+ 1%   stable

E   **I** ^{32}**S**   **%I** $^+$
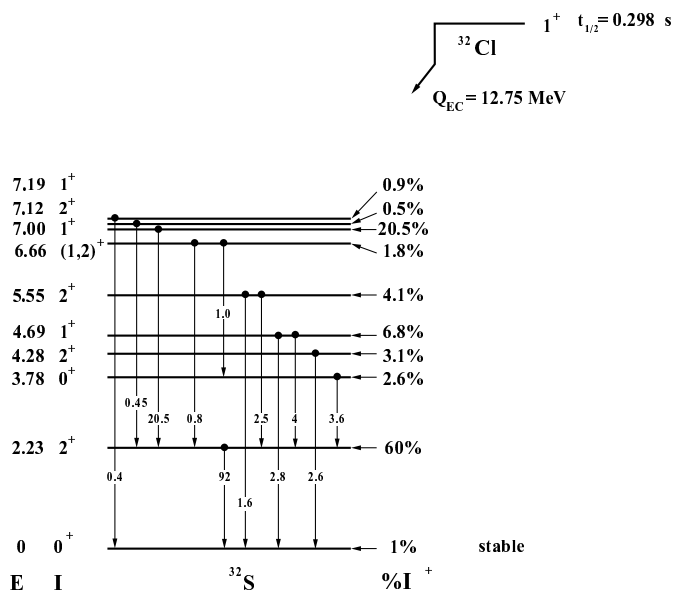
Figure 2.4: *Decay scheme of ^{32}Cl as presented at [Det73].*

nuclides (^{31}S and ^{32}Cl) were simultaneously implanted in the NaCl crystal with a ratio of nearly 2:1. To avoid the influence of the contaminant on our measurement, we used the difference in the Q_{EC} for the two nuclides. As one can see from the decay scheme of ^{31}S (Fig.2.3), nearly all β particles emitted after the decay of ^{31}S have $Q_{EC} = 5.4$MeV while the main branch (60%) of the decay of ^{32}Cl (Fig. 2.4) has $Q_{EC} = 10.52$MeV. Note that a 20% branch from the ^{32}Cl decay has approximately the same $Q_{EC} = 5.75$MeV as the ^{31}S contaminant. For a better understanding of the obtained β-spectra, some simulations were done using the GEANT programme [GEA], in which the real experimental setup was introduced. In two different cases, two pure conditions were simulated: ^{31}S (Fig. 2.5 a) and ^{32}Cl (Fig. 2.5 b) nuclei implanted in the NaCl single crystal. The experimentally obtained β-spectrum of the mixture of ^{31}S and ^{32}Cl (Fig. 2.5 d) demonstrates a pattern, that is very similar to the sum of the two GEANT simulations (Fig. 2.5 c). One can see an edge on the smooth energy curve, marked by an arrow both on Fig. 2.5 c) and d). In the further discussion, the part of the energy spectra which is on the left side of this edge, will be referred to as "low-energy", while the one on the right side will be called "high-energy". The edge is due to the 20% branch in the β-decay of ^{32}Cl ($Q_{EC} = 5.75$MeV) plus the contamination from ^{31}S ($Q_{EC} = 5.4$MeV), superimposed on top of the 60% branch of ^{32}Cl ($Q_{EC} = 10.52$MeV). Thus, if one uses only the high-energy part of the spectrum, the contamination from ^{31}S as well as from the 20% branch of ^{32}Cl will be removed. This has also another advantage. The 20% branch of ^{32}Cl has a mixed Fermi - Gamow-Teller character with unknown mixing ratio. This way it can contribute either positively or negatively to the angular distribution coefficient of the 60% branch, for which $A_1 \approx 0.4$ (see 1.35). The angular distribution coefficient for the high-energy part was calculated to be $A_1 = 0.31$.

Another way to verify if the contaminant of ^{31}S is properly cut away by β-energy selection, is via a life-time measurement. For this purpose, a beam pulsing was introduced in a sequence of 1 s beam-on and 1 s beam-off. Time spectra for triple coincident β-particles were produced for the two energy windows (Fig. 2.6). Afterwards, they were fitted, using fixed half-lives for ^{31}S ($T_{1/2} = 2.572$ s) and ^{32}Cl ($T_{1/2} = 0.298$ s). The yields of the two isotopes were used as free parameters in the fit. The results showed that in the low-energy window the ratio ^{31}S/^{32}Cl = 0.40 ± 0.01, while in the high-energy window the ^{31}S contamination is negligible (^{31}S/^{32}Cl = 0.03 ± 0.01). Note, that in the low-energy window the ratio between ^{31}S and ^{32}Cl is 0.4, while their ratio in the secondary

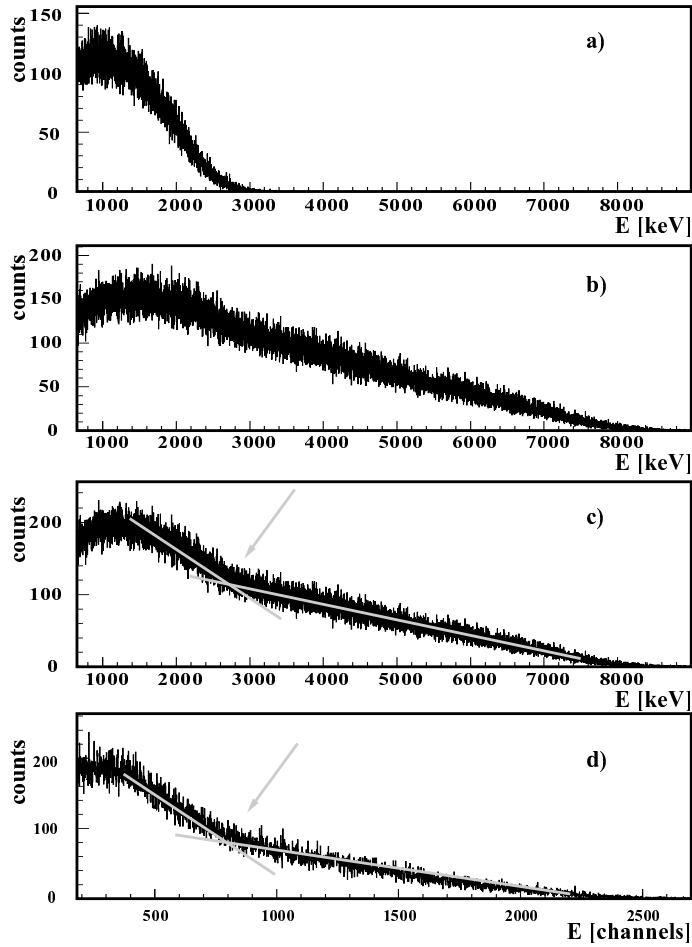Figure 2.5:   a)β-spectrum obtained by a GEANT simulation of a ^{31}S source; b) β-spectrum obtained by a GEANT simulation of a ^{32}Cl source; c) β-spectrum obtained by a GEANT simulation for a 2:1 mixture of ^{31}S and ^{32}Cl sources; d) Experimental β-spectrum in an E-detector, obtained with the condition for triple coincidences between the detectors of the telescope.

beam is approximately $2 : 1$. This difference comes from the fact, that the β-particles have to pass through the implantation crystal and the two ΔE detectors of the telescopes, before their detection in the E detectors. Therefore, a large amount of the low-energetic β particles do not reach the E detectors and this decreases the ^{31}S/^{32}Cl ratio.
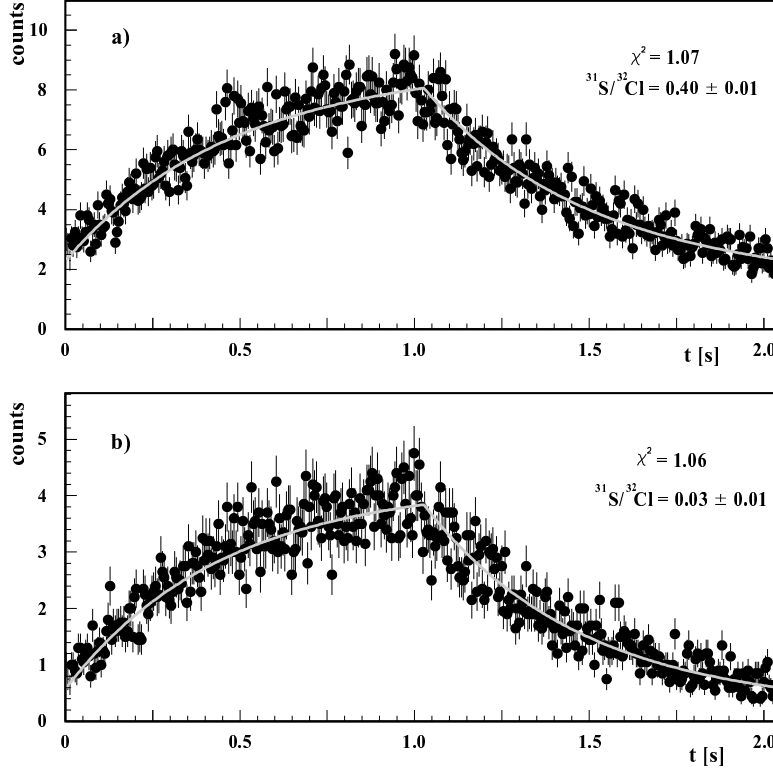
Figure 2.6: *Time spectra for triple coincident β-particles in the a) low-energy window; b) high-energy window.*

We have to mention that the ratios of $^{31}S/^{32}Cl$ in the low-energy and in the high-energy windows is derived for a beam pulsing of 1 s beam on $vs.$ 1 s beam off. However, during the experiment we used a continuous beam implantation. In such a case we can make a rough estimate of the $^{31}S/^{32}Cl$ ratio using Fig. 2.6 a). There we can assume that the

^{31}S activity is constant in time and the ^{32}Cl activity is building up and decaying in time according to the beam pulsing. Taking into account the ratio of the highest decay rate (~ 8) to the lowest one (~ 2), we can say that in a continuous beam the ratio of $^{31}S/^{32}Cl$ (for the low-energy window) should be similar to 0.25.

The search for the position of the NMR resonance was conducted in two stages. During the first one, a frequency modulated (FM) RF-field of $\nu_{RF} = \pm 25$ kHz ($\Delta\nu/\nu \approx 3\%$) was used. The holding field B was set to 100.22(2) mT. A scan of the frequency over the range $[675 \pm 25, 975 \pm 25]$ kHz, corresponding to a total g factor range of $[0.85, 1.31]$, produced the result depicted in Fig. 2.7 a) (open circles). A deviation in the asymmetry signal larger than 5σ unambiguously indicates the resonance position from which we can derive the magnetic moment of $\mu = (1.146 \pm 0.033_{(stat.)} \pm 0.0002_{(syst.)})\mu_N$. The two full circles in the figure were taken during the second stage of the experiment and confirmed the first results. Due to the small difference in the holding magnetic field for the two parts of the experiment, same frequency windows correspond to different g-factor windows. Therefore, there is a small overlap between the resonant point from the first scan and the two points for the second scan. With dashed lines are shown the limits of the overlapping regions between the resonant point from the first scan and the lower frequency point, taken during the second stage of the experiment.

To achieve a better precision on the measured magnetic moment, in the second stage of the experiment, a smaller FM value was applied. The holding field was set to 100.1(1) mT and the modulation was ± 10 kHz ($\Delta\nu/\nu \approx 1\%$). The scanned frequency window was $[835 \pm 10, 895 \pm 10]$ kHz corresponding to a g factor range of $[1.081, 1.186]$. The results from the second scan are depicted in Fig. 2.7 b). Two neighboring points show a change in the β-decay asymmetry and thus define the position of the resonance. Due to the overlap between the region covered by these two points and their neighboring points, which do not show a change in the β-decay asymmetry, the overlapping regions can be excluded as possible resonance windows. Thus only the 10-kHz-wide frequency window (dashed lines in Fig. 2.7 b), shared only by these two points, defines the resonance location. The center of this window, 850 kHz, was used to deduce the ^{32}Cl magnetic moment, yielding $\mu = (1.114 \pm 0.006_{(stat)} \pm 0.001_{(syst)})\mu_N$. The statistical error includes the uncertainty coming from the width of the FM window, while the systematic error is due to the uncertainty of the holding magnetic field.

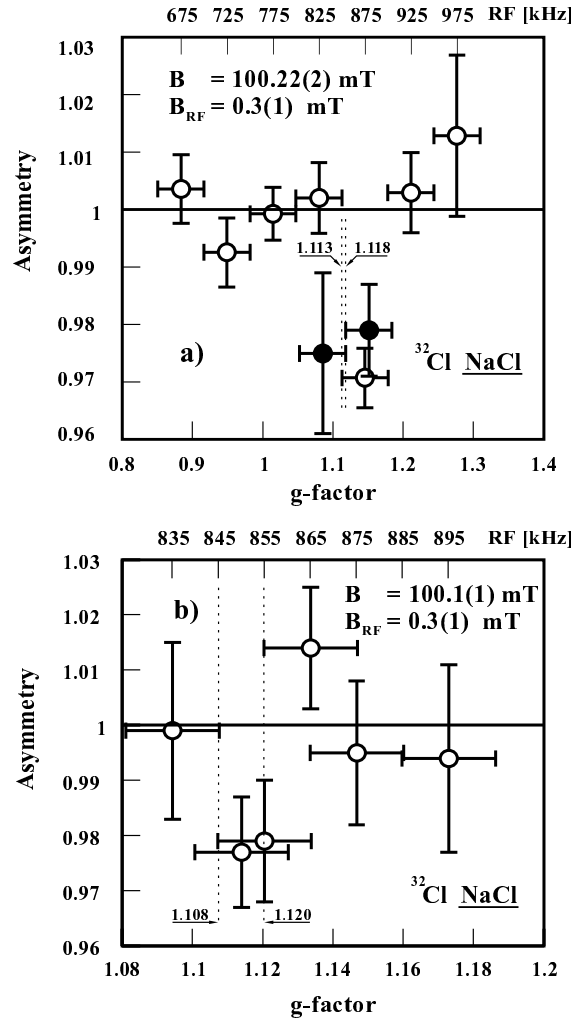Figure 2.7: *Resonance curves obtained for ^{32}Cl implanted in NaCl. The applied frequency modulation was a) ± 25 kHz and b) $\pm 10kHz$. The modulation had a ramp waveform with a 500 Hz repetition rate.*

2.2.3 Estimation of the polarization obtained in the reaction

To estimate the amount of the polarization obtained in the reaction we will have to account for all of the factors, that decrease it. We can

simplify the formula, which we use to calculate the change in the β-asymmetry (eqn. 2.1) and rewrite it in the form:

$$R = \frac{1 + fA_1B_1}{1 - fA_1B_1} \approx 1 + 2fA_1B_1 \qquad (2.2)$$

where we also used formula (1.34) and the fact that our detectors are positioned at 0° and 180°, respectively. Here, A_1 is the angular distribution coefficient (also called asymmetry parameter); B_1 is the orientation parameter, which is related to the reaction created polarization; with f we denote a parameter, which accounts for all possible reasons for decrease of the reaction-created polarization. Thus, the experimentally measured NMR amplitude, $As_{exp.}$ is related to the reaction-induced polarization, P (see, e.g., [Cou01]), as :

$$As_{exp.} = R - 1 \approx -2fA_1\sqrt{\frac{3I}{I+1}}P \qquad (2.3)$$

Some of the processes, which can contribute to the decrease of the experimentally observed β-asymmetry are: i) loss of orientation between the production target and the implantation host (e.g., pick-up of electrons); ii) non-substitutional implantation in the host; iii) purely geometrical factors, accounting for the finite size of the detectors; iv) back scattering of the β particles.

On the first of these points, we can say that an electron pick-up occurs during the passage of the ions through any materials between the target and the implantation host. The spins of the picked up electrons would be randomly oriented in space. The interaction of the spins of the non fully stripped ions with external fields can cause a partial decrease up to full loss of orientation of the nuclear ensemble [Gol82, Vyv00]. In our case, the ^{32}Cl ions are passing a 100 μm mylar window and 25 cm of air, at an energy of ~ 30 MeV/u. According to the calculations performed with the LISE program [Baz01], the probability for electron pick-up at this energy is negligible. Thus, this is not an issue in our experiment.

As it was mentioned before, we have chosen a NaCl single crystal as an implantation host in order to have the ^{32}Cl ions implanted in substitutional sites. Therefore, this should also not decrease the reaction-created orientation of the nuclear ensemble.

To estimate the influence of the geometrical factors and the back scattering of the β-particles, we performed GEANT [GEA] simulations, in which the realistic setup was introduced. In these calculations, we

simulated two cases: i) ^{32}Cl ions implanted in 2 mm NaCl crystal in a "beam spot" of 8 mm (realistic case); ii) the same as the first one but assuming, the ions were implanted "in vacuum". In both cases we used a "polarized source", in which the angular distribution of eqn. 1.34 was simulated. The product of $A_1 B_1$ was set to 0.2. The GEANT simulations gave β-asymmetries in the triple-coincident energy spectra as follows: $R = 1.198(2)$ for the ^{32}Cl ions implanted in NaCl crystal and $R = 1.276(2)$ for a ^{32}Cl source in vacuum. Using formula 2.2 we can calculate from the "in vacuum" asymmetry, that the geometrical reduction factor for the setup is 0.61 and, if one includes also the back scattering of the β-particles in the crystal, the total parameter of decrease of orientation is $f = 0.45$. Using this value and the angular distribution coefficient for the high-energy part of the β-spectrum of ^{32}Cl ($A_1 = 0.31$), we deduce from the experimental NMR amplitude $As_{exp.} = -0.03$ the orientation parameter $B_1 = 0.109$. After applying the relation between the orientation parameter and the polarization of the ensemble, we obtain $P = 8.9\%$.
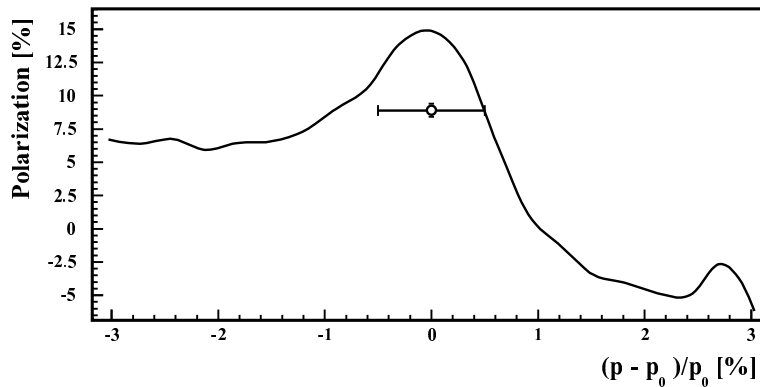
Figure 2.8: *Comparison between the reaction-created polarization, derived experimentally, and the theoretical simulations.*

The comparison of the so deduced reaction-created polarization with theoretical simulations [Dau] is presented in Fig. 2.8. The curve is obtained using the kinematical fragmentation model [Asa91, Oku94, Dau01]. This result shows that a spin-polarized ensemble of nuclei can be obtained also in the center of the momentum distribution.

2.3   Interpretation of the results

To calculate the magnetic moment of the odd-odd nucleus $^{32}_{17}$Cl$_{15}$ for the assumed single-particle configuration $(\nu s_{1/2} \otimes \pi d_{3/2})_{1+}$ we can use the additivity relation (eqn. 1.16) and the free nucleon g factors for the $s_{1/2}$ neutron ($g = -3.8261$) and $d_{3/2}$ proton ($g = 0.08286$). Then we obtain the value $\mu_{sp}(^{32}$Cl$) = 1.06$ μ_N. Comparing this value to the experimentally measured magnetic moment of 1.114(6) μ_N, one might conclude that the configuration of this state is close to the single-particle one. However, a more detailed comparison with the magnetic moments of the neighboring T $= 1/2$ nuclei ^{31}S and ^{33}Cl (see Table2.1), which have ground state spins in agreement with a $\nu s_{1/2}$ and $\pi d_{3/2}$, respectively, shows that the experimental moments are quite far from the singe-particle shell model (SPSM) value. The same conclusion also holds for the magnetic moments of the mirror nuclei ^{31}P, ^{33}S and ^{32}P (see Table 2.1). If the values of the experimentally measured magnetic moment of ^{31}S and ^{33}Cl [Rag89] are used for the calculation of the magnetic moment of ^{32}Cl, we find $\mu_{emp.}(^{32}$Cl$) = 0.871$ μ_N which is very different from the measured value.

A better understanding of the magnetic moment comes from calculations in a full sd $(1s_{1/2}, 0d_{5/2}, 0d_{3/2})$ spherical shell model basis. We have calculated wave functions and magnetic moments with three different effective sd-shell Hamiltonians. All of them consist of one- and two-body parts and are, therefore, defined by all possible one-body (3) and two-body (63) matrix elements, that can be formed with active orbits in the sd shell. The diagonalization of the Hamiltonian yields a set of mixed-configuration shell-model wave functions, which are used to calculate the magnetic moment. For the ^{32}Cl case, the dimension of the matrix is 1413.

First, we compare the results based on the USD (universal sd) Hamiltonian of Wildenthal [Bro88b]. This Hamiltonian has been derived starting from a renormalized G matrix and a fit has been done to linear combinations of two-body matrix elements, using a large set (about 450) of binding and excitation energies of sd-shell nuclei. The USD Hamiltonian includes a mass dependence of the two-body matrix element (TBME) of the form

$$\langle V \rangle(A) = \langle V \rangle(A = 18) \left(\frac{A}{18}\right)^{-0.3} \tag{2.4}$$

The comparison of the magnetic moments for $A = 31 - 33$, obtained with

Table 2.1: Experimental and calculated magnetic moments for the $A = 31 - 33$ isospin multiplets. The calculated moments are based on the SPSM value and on the full sd-shell basis with three effective Hamiltonians USD, SDPOTA and SDPOTB (the last two denoted with A and B, respectively). The $M1$ operator is evaluated with the free-nucleon and the effective sd-shell operator of Ref. [Bro87]. Experimental data are from [Rag89] and [Rog00].

	Hamilt. $M1$		Exp.	SPSM free	USD free	USD eff	A eff	B eff
	Nucleus	I^π						
μ	$^{31}\mathrm{S}_{T_z=+\frac{1}{2}}$	$\frac{1}{2}^+$	-0.488	-1.913	-0.400	-0.431	-0.547	-0.591
	$^{33}\mathrm{Cl}_{T_z=+\frac{1}{2}}$	$\frac{3}{2}^+$	0.752	0.124	0.704	0.799	0.730	0.796
	$^{32}\mathrm{Cl}_{T_z=+1}$	1^+	$1.114(6)$	1.060	1.006	1.157	1.177	1.232
μ	$^{31}\mathrm{P}_{T_z=-\frac{1}{2}}$	$\frac{1}{2}^+$	1.235	2.793	1.023	1.086	1.241	1.288
	$^{33}\mathrm{S}_{T_z=-\frac{1}{2}}$	$\frac{3}{2}^+$	0.644	1.148	0.651	0.643	0.724	0.659
	$^{32}\mathrm{P}_{T_z=-1}$	1^+	-0.252	-0.440	-0.131	-0.238	-0.308	-0.348
μ^{IV}	$\frac{A=31}{T=\frac{1}{2}}$	$\frac{1}{2}^+$	-0.862	-2.353	-0.711	-0.758	-0.894	-0.939
	$\frac{A=33}{T=\frac{1}{2}}$	$\frac{3}{2}^+$	0.054	-0.512	0.026	0.078	0.003	0.069
	$\frac{A=32}{T=1}$	1^+	0.683	0.750	0.568	0.697	0.742	0.790
μ^{IS}	$\frac{A=31}{T=\frac{1}{2}}$	$\frac{1}{2}^+$	0.373	0.440	0.311	0.328	0.347	0.348
	$\frac{A=33}{T=\frac{1}{2}}$	$\frac{3}{2}^+$	0.698	0.636	0.678	0.721	0.727	0.727
	$\frac{A=32}{T=1}$	1^+	0.431	0.310	0.438	0.460	0.434	0.442
$\langle s \rangle$	$\frac{A=31}{T=\frac{1}{2}}$	$\frac{1}{2}^+$	0.324	0.500	0.162	0.204	0.255	0.259
	$\frac{A=33}{T=\frac{1}{2}}$	$\frac{3}{2}^+$	-0.137	-0.300	-0.191	-0.076	-0.060	-0.060
	$\frac{A=32}{T=1}$	1^+	-0.182	-0.500	-0.164	-0.107	-0.172	-0.153

this Hamiltonian using free-nucleon g factors, are presented in Table 2.1 (USD-free). The agreement with the experiment is greatly improved, compared to the single-particle free values. The assumed single-particle configuration is actually only 41% of the full sd-shell wave function. The remaining 59% of the wave function is a complex mixing of many configurations. The deviation between the experimental and the USD-free values of the magnetic moment is up to 0.2 μ_N.

Another approach to compare the experimental magnetic moments with the theoretical calculations, is by calculating the isoscalar and the isovector moments. This is possible to be done only within isospin multiplets, where the magnetic moments of two members are measured. In such a case the isoscalar and the isovector moments are readily extracted:

$$\mu^{IS} = \frac{1}{2}[\mu(T_z = +T) + \mu(T_z = -T)] \tag{2.5}$$

$$\mu^{IV} = \frac{1}{2}[\mu(T_z = +T) - \mu(T_z = -T)]. \tag{2.6}$$

If the isospin is assumed to be a good quantum number and the isoscalar exchange currents are ignored, one can write the following relation between the isoscalar moment and the isoscalar spin expectation value [Sug69, Bro83]:

$$\mu^{IS} = \frac{J}{2} + \left(\frac{g_s^\nu + g_s^\pi - g_l^\pi}{2}\right)\langle s\rangle \tag{2.7}$$

After substituting the free-nucleon g factors $g_l^\pi = 1$, $g_l^\nu = 0$, $g_s^\pi = 5.5855$ and $g_s^\nu = -3.826$, we obtain

$$\mu^{IS} = \frac{J}{2} + 0.38\langle s\rangle \tag{2.8}$$

where

$$\langle s\rangle = \sum_k \langle JM|s_z^{(k)}|JM\rangle_{M=J} \tag{2.9}$$

is the intrinsic spin expectation value.

The isoscalar magnetic moment calculated with USD-free for the three isospin multiplets appear to be in better agreement with the experiment, than the SPSM value but this is due to the trivial J factor which appears in Eqn. 2.8. If the same equation is used to derive the spin expectation value (last three rows of Table 2.1), the deviations are much larger.

Thus, although on first sight it seems that the experimental moments are well reproduced using free-nucleon g factors, a detailed comparison of its isoscalar and isovector components to the free-nucleon values fails. Therefore, to account for the higher order configuration mixing and the mesonic exchange currents, we used an effective $\overrightarrow{M1}$ operator. It was deduced [Bro87] in the form:

$$\overrightarrow{M1}^{\,eff} = \sqrt{\frac{3}{4\pi}}\left[g_s s + g_\ell \ell + g_s \delta(M1)\right]\mu_N \tag{2.10}$$

where the correction $\delta(M1)$ to the magnetic moment operator has been derived by a fit to 49 magnetic moments and 114 $M1$ transitions whose associated matrix elements are measured with an accuracy better than 10%. An additional mass dependence of the form

$$\delta(A) = \delta(A = 28)\left(\frac{A}{28}\right)^{0.35} \tag{2.11}$$

has been also used in the fit. The resulting corrections for the mass $A = 28$ are given in Table 2 of Ref. [Bro87].

The magnetic moments calculated with the effective $M1$ operator of Ref. [Bro87] are compared with the experimental data for $A = 31 - 33$ in Table 2.1 (USD-eff). In most cases, there is some improvement over the USD-free result compared to the experimental values but the changes are not very large and the overall deviation between the experiment and theory still stands. However, a better agreement is obtained for the isoscalar and the isovector components of the magnetic moment. The rather small differences between the USD-free and USD-eff results are due to the complexity of the actual wave functions.

The complexity of the wave functions in the $A = 31 - 33$ region has the consequence that the results are sensitive to the sd-shell Hamiltonian which is used. There are two other "universal" sd-shell Hamiltonians which we have examined: the SDPOTA and SDPOTB from Ref. [Bro88a]. They are based on the adjustment of the strengths of the density-dependent one-boson exchange potentials and are derived under the following conditions:

(1) The wave functions have good isospin quantum number.

(2) The two-body matrix elements used for the values of the poorly determined linear combinations in the fit are those used in Ref. [Hos85].

(3) The two-body matrix elements have the following mass depen-

dence

$$\langle V \rangle (A) = \langle V \rangle (A = 18) \left(\frac{A}{18} \right)^{-0.35} \tag{2.12}$$

(4) The experimental data set used in the fit consists of 447 ground and excited states energies in the sd-shell nuclei.

(5) The one-body and the two-body transition densities are calculated from the same set of wave functions as those used to obtain the USD interaction.

The difference between the two Hamiltonians is in the way they treat the single-particle energies (SPE). In SDPOTA they are taken to be constant over the whole sd-shell while for SDPOTB a linear mass dependence of the SPE is introduced:

$$SPE(A) = SPE(A = 17) + \frac{A - 17}{22} \left[SPE(A = 39) - SPE(A = 17) \right] \tag{2.13}$$

This leads to a 17-parameter fit for SDPOTA and a 20-parameter fit for SDPOTB.

The overall description of binding and excitation energies for the entire sd shell is about the same as for USD. A comparison between the USD, SDPOTA and SDPOTB results gives an indication on the sensitivity of the magnetic moments to the small and energetically undetermined parts of the sd-shell Hamiltonian.

The results from the calculations of the magnetic moments in the $A = 31 - 33$ region using these three Hamiltonians and an effective $M1$ operator [Bro87] are compared with the experimental data in Table 2.1. There are deviations of up to 0.2 μ_N between the results of the different Hamiltonians. The SDPOTA results are in best agreement with the experiment, which suggests that this Hamiltonian would be best for the $A = 31 - 33$ region. However, to make a general conclusion about the Hamiltonian, one has to carry out a broader comparison between experimental data and $M1$ observables calculated with SDPOTA for other sd-shell nuclei. In general, one can conclude that magnetic moment data provides important information for testing and determining the effective Hamiltonian.

Chapter 3

g-factors of isomeric states in the vicinity of ^{68}Ni

3.1   Motivation

Measurements of the g factor of a nuclear state provide unique information on its single particle structure and wave-function composition. The g-factor observable is an important ingredient in the nuclear models and can serve as a testing ground for them. This is especially interesting to be done in the vicinity of shell-closures where the simple picture of one particle (hole) coupled to an inert core is supposed to be the most realistic model and the nuclear wave functions are expected to be quite pure. Under such conditions, the g-factors are expected to be closest to the Schmidt lines.

Due to the fast developments in the nuclear detection techniques and the radioactive beam facilities, a large number of exotic nuclei with extreme values of spin and isospin became available for investigation in the recent years. The study of these exotic species allows us to gain insights into the nuclear structure far from stability, where new features, unobservable close to stability, can be expected. A direct example of this is the evidence of changes in the shell closures at extreme isospin values [Mot95, Oza00]. Being a sensitive probe to the nuclear structure, the g factors can reveal the detailed composition of the wave functions

in such regions.

Recently, the neutron rich region around ^{68}Ni has been the subject of extensive experimental and theoretical investigation. Bernas *et al.* [Ber82a] reported that the first excited state in ^{68}Ni is a 0^+-state and suggested that this is due to the appearance of a sub-shell gap at $N = 40$. Broda *et al.* [Bro95] found that the energy of the first excited 2^+ state in ^{68}Ni increases by more than 500 keV compared to ^{66}Ni (see Fig.3.1), indicating an increased stability of $N = 40$. Recently, many yrast isomers in neighboring nuclei around ^{68}Ni have been identified [Bro95, Paw94, Grz98, Mue99, Ish00]. Their structure is explained (i) as particle-hole excitations from the neutron fp-shell into the $\nu 1g_{9/2}$ orbit across a "sub-shell gap" for $N \leq 40$ Ni isotopes and (ii) by coupling valence protons and/or neutrons to the ^{68}Ni ground state or its $1p1h$ $I^\pi = 5^-$ isomer. In Fig. 3.2 we represent the single-particle levels above the ^{56}Ni core (as deduced from [Gra99, HJ95]), relevant to the structure in vicinity of ^{68}Ni.
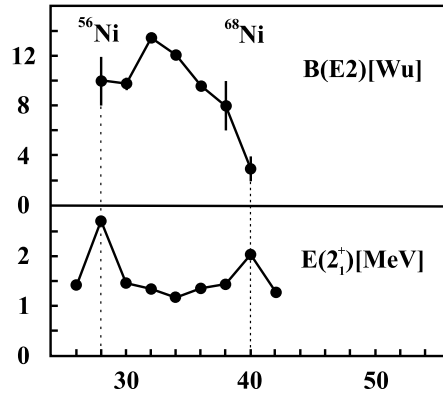

Figure 3.1: *Transition strength B(E2;2$^+$ $\rightarrow$ 0$^+$) and excitation energy E(2$_1^+$) and for Ni isotopes. (picture from [Gra00])*

On the other hand the two-neutron separation energies, S_{2n}, for the Ni isotopes [Sei94] are not consistent with a sub-shell closure (see Fig.3.3). This experimental observation is well reproduced by relativistic mean-field theory only after introducing collective correlations [Rei00], which suggests β-softness for the ^{68}Ni neighbors (^{66}Ni and ^{70}Ni). Another experimental evidence for the weakness of the proposed $N = 40$ sub-shell closure comes from a β-decay measurement of Mueller *et al.*
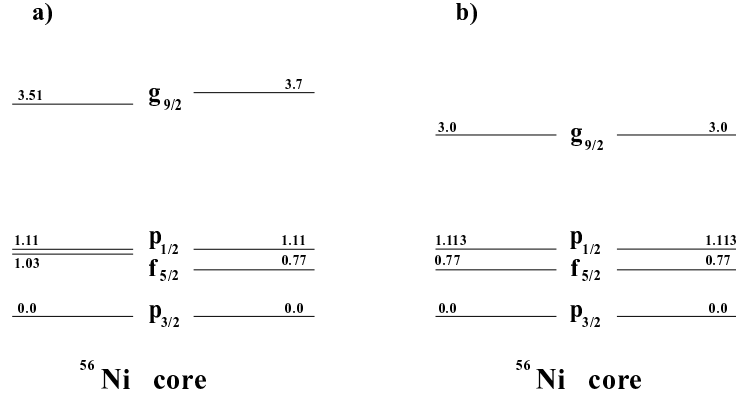
Figure 3.2: *Single-particle energies in the ^{68}Ni region as deduced from a) [Gra99] and b) [HJ95].*

[Mue99], where they deduce a mixing of 9(4)% of the $\pi p_{3/2}^{+1}\nu p_{1/2}^{-2}g_{9/2}^{+2}$ configuration in the ground state of ^{69}Cu, which implies a significant polarization of the ^{68}Ni core with a coupling of a single nucleon.

The g factors are very sensitive probe to particular components of the core polarization, namely, the coupling of spin-orbit partners to form a 1^+ state. On the other hand, if ^{68}Ni is a good shell closure, one would expect that the g factors of single-particle states in the vicinity, are close to the Schmidt limits. Therefore, a g factor measurement of isomeric states in the vicinity should be able to shed light on the structure in the region. We performed an experiment at GANIL, France, on isomeric states in ^{69}Cu, ^{67}Ni and ^{66}Co and the results of the TDPAD measurement will be presented in this chapter.

3.2 Studies of the structure in the ^{68}Ni region

By moving farther away from stability, by increasing the neutron number, the Fermi level is approaching the unbound nuclear states and the interaction of the nucleons with the continuum is expected to have a strong impact on the nuclear properties. Close to the neutron drip-line, due to the large diffuseness of the neutron density and of the central potential, some harmonic oscillator features can be reinforced [Dob94],
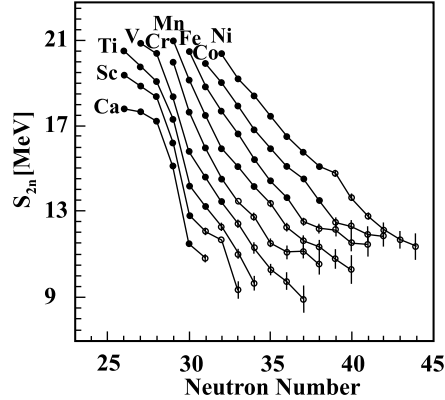
Figure 3.3: *Two-neutron separation energies as presented in [Sei94].*

which can give rise to changes in the magic numbers. As it was mentioned above, the interest towards the neutron-rich region around ^{68}Ni was triggered by the hint of appearance of a new shell-closure at $N = 40$. Different experimental approaches were used to shed more light on the structure in the region. In the following section, we will give an overview on the results.

3.2.1　Transfer reactions

Producing a neutron-rich nuclear species represents a real challenge for the experimentalists. Reaction mechanisms like fusion-evaporation, which are very suitable for the proton rich region of the nuclear chart, cannot go towards neutron-rich nuclei without using radioactive beams.

One of the ways of producing neutron-rich isotopes is by using transfer reactions. In such a type of experiment, one can obtain information on the mass excess of the produced nuclei and, possibly, on their excited states. If the angular distribution of the outgoing particles is measured, one can deduce the orbital angular momentum of the populated states. In specific cases, the angular distribution of the outgoing particles depends not only on L but also on J, so a direct spin assignment can be made. Some of the difficulties of the transfer reactions are: i) an isotopically enriched target is needed (the typical values are of the order of 95% and higher); ii) any contamination of the target can make the

interpretation of the data more complex; iii) the usually obtained energy resolution is of the order of a few 10 keV to a few 100 keV.

Let us now summarize some of the data obtained in transfer reactions for the neutron-rich Ni region.

Ni isotopes

In a study of the even Ni isotopes using a (t,p) reaction, Darcey *et al.* [Dar71] observed for the first time ^{66}Ni in its ground state and managed to identify several 0^+ and 2^+ states as well as a 3^- state. These results were later confirmed by Alford *et al.* [Alf80]. Kouzes *et al.* [Kou78b] determined in a ^{70}Zn(^{4}He,^{7}Be) reaction the mass excess of ^{67}Ni and identified its first three excited states without determining their spins and parities. Bernas *et al.* [Ber81] observed the ground and the first excited state in ^{68}Ni ($E_x = 1.47$ MeV). In a later work [Ber82a], after increasing the isotopic purity of the ^{70}Zn target from 67.6% to 99.9%, they measured the angular distribution for the first excited state ($E_x = 1.77$ MeV; the previously determined 1.47 MeV state appeared to come from some oxygen contamination in the target) and identified it as a 0^+ state. They suggested that this is a sign of magic properties of ^{68}Ni. This suggestion stimulated further investigations in the $N = 40$ region.

Dessagne *et al.* [Des84] observed for the first time the ground state of ^{69}Ni in a ^{70}Zn(^{14}C,^{15}O) reaction and determined its mass. Deriving the two-neutron separation energies (S_{2n}) for the chain of Ni isotopes, they did not observe any deviation from the systematic trend around $N = 40$.

Girod *et al.* [Gir88] studied the spectroscopy of ^{67}Ni and ^{68}Ni using the ^{70}Zn(^{14}C, $^{16-17}$O) reactions. The energies they obtained for the excited states in ^{67}Ni are 10% higher than previous values and their spin assignments are at variance with later determined values.

Cu isotopes

The even Cu isotopes were studied by Sherman *et al.* [She77] via a $(t,^3$He) reaction. They measured the mass excess for ^{68}Cu and ^{70}Cu and also observed a multiplet of highly populated states with systematically decreasing excitation energies as the neutron number approaches 40. They attributed this multiplet to a $\pi p_{3/2} \nu g_{9/2}$ configuration. Since they did not measure the angular distributions of these multiplets, no direct spin determination was done.

The odd-mass Cu isotopes were studied by Zeidman *et al.* [Zei78] via a $(d,^3\text{He})$ reaction in which they also measured the angular distributions for the low-lying states. The energies and spins/parities, which they assigned to the levels observed in ^{69}Cu, are presented in Table 3.1.

Table 3.1: *^{69}Cu states populated in a (d,^{3}He) reaction and their spin assignments [Zei78].*

E_x [MeV]	I^π
0	$3/2^+$
1.11	$1/2^-$
1.23	$5/2^-$
1.74	$7/2^-$
1.87	$7/2^-$

In a later experiment, Ajzenberg-Selove *et al.* [AS81] used polarized tritons in a $^{70}\text{Zn}(t,\alpha)^{69}$Cu reaction and determined unambiguously the spins and parities of the first two excited states in ^{69}Cu and also observed an excited state at $E_x = 2540$ keV, for which they did not make a spin/parity assignment.

Co isotopes

The Co isotopes in the $N = 40$ region are even farther removed from the stability line and they are becoming more difficult to observe in transfer reactions. The mass of ^{64}Co was measured by Flynn *et al.* [Fly72] in a $^{64}\text{Ni}(t,^3\text{He})$ reaction in which they also observed some excited states. They did not make spin/parity assignments. In a $^{70}\text{Zn}(^3\text{He},^8\text{B})$ reaction, Kouzes *et al.* [Kou78a] deduced the mass-excess of ^{65}Co. They also found a hint for an excited state therein. There are no other neutron-rich Co isotopes studied in transfer reactions.

In summary, we can say that the transfer reactions provide basic information on the spin/parity assignments of the populated nuclear states, provided the angular distribution of the outgoing reaction products is measured. They are an important first step approach towards the study of a region. Due to the nature of this reactions, they cannot produce nuclear states very far from stability.

3.2.2 β-decay studies

Another approach towards the understanding of the structure of the neutron-rich nuclei is via β-decay studies. Due to its selective nature, one can deduce information on the nuclear structure of the daughter nuclei. Quite an important point in the β-decay studies is the measurement of the $\beta - \gamma$ and $\gamma - \gamma$ coincidences with the help of which one can deduce the half-life of the decaying nuclei (as this is done in ion - β correlations, see e.g. [Ame98]). It is also possible to build the level scheme of the daughter nucleus and to distinguish between different β-decaying states in the same mother nucleus.

Co isotopes

We will first focus our attention on the extensive studies of the Co isotopes which were done at the Leuven Isotope Separator On Line (LISOL). The results for the even masses are presented by Mueller *et al.* in ref. [Mue00]. The half-life of the ground state of ^{66}Co ($t_{1/2} = 0.18(1)$ s) is determined in this work via the measurement of the β-delayed γ-rays. In the ^{66}Co β-decay, they observe three γ lines (1246 keV, 1426 keV and 1805 keV) and propose the level scheme presented in Fig. 3.4. The ground state of ^{66}Co is proposed to have a $\pi f_{7/2}^{-1} \nu p_{1/2}^{-1}$ configuration with $I^\pi = 3^+$. The favored decay mode of such a configuration would be a Gamow-Teller conversion of an $f_{5/2}$ neutron into $f_{7/2}$ proton. This means that the most strongly fed levels in ^{66}Ni will have $\nu f_{5/2}^{-1} p_{1/2}^{-1}$ as main contribution to their wave functions. Thus the levels at 2672 keV and at 3228 keV are proposed to be respectively the 3^+ and 2^+ members of this multiplet.
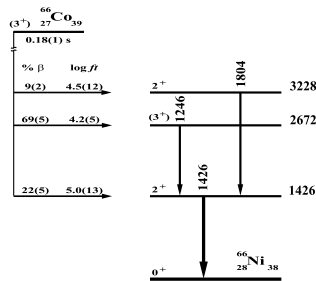

Figure 3.4: *Decay scheme of ^{66}Co as presented in [Mue00].*

From the time analysis of the β-delayed γ-rays in the decay of ^{68}Co, Mueller *et al.* observed two distinct half-lives, indicating two different β-decaying states. The deduced level scheme is presented in Fig. 3.5. The proposed configurations of the two β-decaying states in ^{68}Co are $(\pi f_{7/2}^{-1}\nu g_{9/2})_{7^-}$ and $(\pi f_{7/2}^{-1}\nu p_{1/2}^{-1}g_{9/2}^2)_{3^+}$ with half-lives of 0.23(3) s and 1.6(3) s, respectively. The ^{68}Ni levels at 3120, 3444 and 3557 keV, originating from the decay of the shorter-lived state in ^{68}Co, are interpreted as the 5^-, 6^- and 7^- members of the $\nu f_{5/2}^{-1}g_{9/2}$ multiplet, respectively. Possible direct feeding of the 5^- isomeric state at 2848 keV in ^{68}Ni by the (7^-) β-decaying state of ^{68}Co is not excluded, which favors a significant contribution of a $\nu f_{5/2}^{-1}g_{9/2}$ component to the wave function of the 5^- isomer (assigned to have $\nu p_{1/2}^{-1}g_{9/2}$ as main configuration).
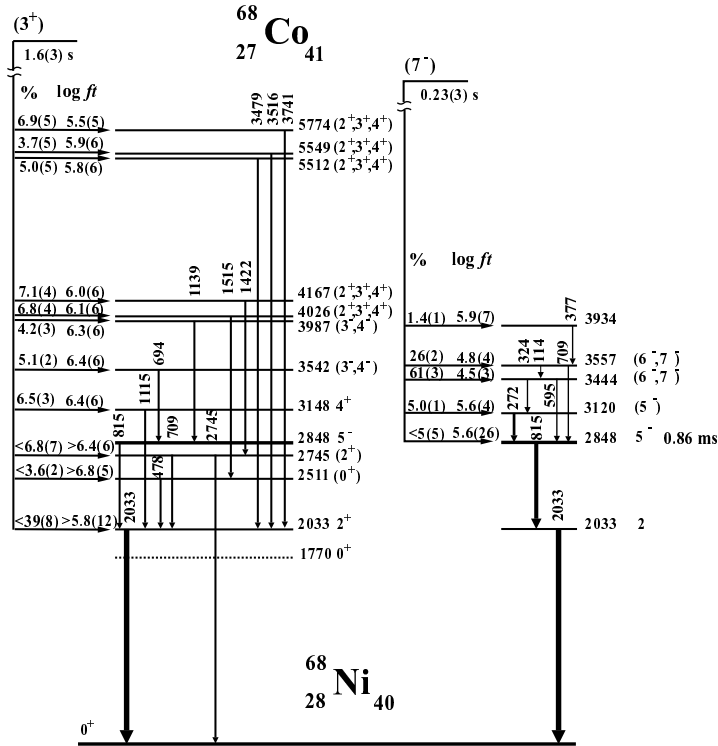
Figure 3.5: *Decay scheme of ^{68}Co as presented in [Mue00].*

The very large fragmentation of the decay of the longer-lived (3^+) state of ^{68}Co suggests that either there are no states in ^{68}Ni with a dominant $\nu f_{5/2}^{-1} p_{1/2}^{-1} g_{9/2}^2$ configuration in its wave function or the configuration of the ^{68}Co isomer is strongly mixed. The most strongly populated states from the longer-lived isomer are grouped around 5.5 MeV. They are interpreted as the 2^+, 3^+ and 4^+ members of the core-excited configuration $\pi f_{7/2}^{-1} p_{3/2} \nu p_{1/2}^{-2} g_{9/2}^2$. The two states at 4026 keV and 4167 keV are proposed to have $\nu f_{5/2}^{-1} p_{1/2}^{-1} g_{9/2}^{+2}$ as main component in their wave function but it is also possible that they represent the $\pi f_{7/2}^{-1} p_{3/2}$ configuration. In the latter case, the lack of a $g_{9/2}$ neutron pair can explain the retarded β-feeding to these levels.

In ^{70}Co, similarly to the case of ^{68}Co, there are also two β-decaying states observed by Mueller *et al.*. Their single-particle configurations are interpreted as $\pi f_{7/2}^{-1} \nu g_{9/2}^3$ and $\pi f_{7/2}^{-1} \nu p_{1/2}^{-1} g_{9/2}^4$ with possible spin assignments of 6^- or 7^- and 3^+, respectively. Due to the very large Q value (≈ 12 MeV) and making an analogy with the complexity of the structure of ^{68}Co, the authors gave the branching ratios and the log ft values only as upper limits. The proposed level schemes are presented in Fig. 3.6.
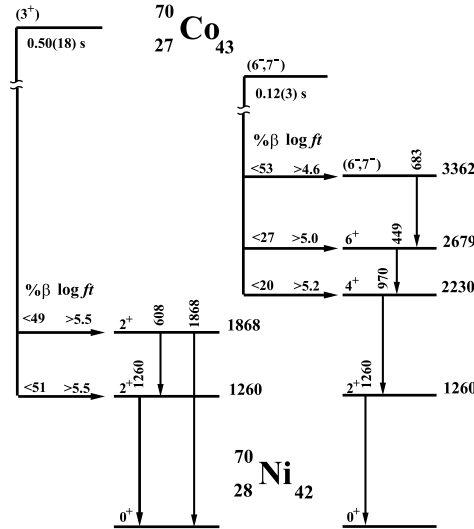

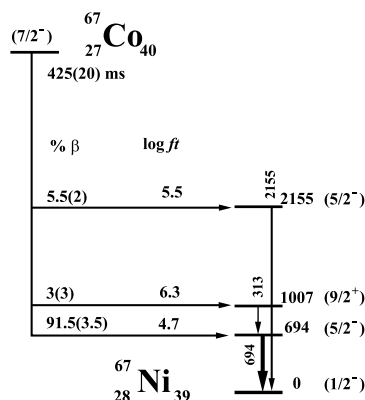Figure 3.6: *Decay scheme of ^{70}Co as presented in [Mue00].*

Figure 3.7: *Decay scheme of ^{67}Co as presented in [Wei99]. The spin/parity assignments of the ground and the first two excited state are confirmed by [Grz98, Rik00, Mac01].*

The β-decay study of ^{67}Co was also performed at LISOL and the results are reported by Weissman *et al.* in ref. [Wei99]. The measured half-life is 0.425(20) s and the deduced level scheme is presented in Fig. 3.7. The main branch of the decay of the ground state of ^{67}Co goes to a 694 keV state with spin assignment of $I^\pi = 5/2^-$, based on the small log ft value. A small branch with relatively low log ft value (5.5) goes to a state at 2155 keV, which is observed to be directly de-excited via a 2155 keV transition to the ground state. This leaves the only possible spin assignment of the state to be also $5/2^-$. Due to the long half-life of the 1007 keV state in ^{67}Ni ($t_{1/2} = 13.3(2)\mu$s [Grz98]), its direct feeding in the β-decay cannot be observed in the $\beta - \gamma$ coincident spectra because of the short correlation window of 1μs. However, in the analysis of the $\gamma - \gamma$ coincidences, the 313 keV and the 694 keV lines appear to be in coincidence, which suggests that the 1007 keV $(9/2^+)$ state is also directly populated in the β-decay. The observation of this l-forbidden decay indicates an admixture of $\pi f_{7/2}^{-1} \nu p_{1/2}^{-2} g_{9/2}^2$ in the $\pi f_{7/2}^{-1}$ ground state configuration of ^{67}Co. The authors proposed two possible configurations of the 2155 keV state: i) a $p_{1/2}$ neutron hole of the ground state of ^{67}Ni coupled to the 2^+ level at 2033 keV in ^{68}Ni and ii) a second excited $f_{5/2}$ hole state at 694 keV coupled to the excited 0^+ state at 1770 keV in the ^{68}Ni core. The realization of the former scenario would require a mixing

of the ground state with the $f_{5/2}$ single-hole state at 694 keV, which is not very probable due to their large separation in energy. For the realization of the latter, it would be necessary to excite a $p_{1/2}$ neutron pair across the sub-shell gap to the $g_{9/2}$ orbital - a situation which is also hinted by the observation of the direct β-decay to the 1007 keV state. Thus this is more realistic according to the authors.

It is worth mentioning that in this type of β-decay studies, due to the specifics of the experimental setup (the requirement of $\beta - \gamma$ or $\gamma - \gamma$ coincidences and no full β-energy spectra recorded), it is not possible to observe a ground state to ground state β-decay if it exists.

^{69}Co is another nucleus whose β-decay was measured at LISOL. The results are reported by Mueller *et al.* in ref. [Mue99]. Only about 70% of the γ-ray intensity, all of which is decaying to states feeding the $1/2^-$ isomer in ^{69}Ni, has been placed in the partial level scheme shown in Fig. 3.8. The remaining 30%, which the authors could not assign unambiguously, are suggested to come from feeding the ground state of ^{69}Ni. The positive parity states in the daughter nucleus come from the coupling of a $g_{9/2}$ neutron to the core-excited states in ^{68}Ni and the negative parity levels are interpreted as arising from the coupling of a $p_{1/2}$ or $f_{5/2}$ hole to the ^{70}Ni core. The proposed assignment of the most strongly populated level in the β-decay (915 keV) is $\nu f_{5/2}^{-1} \otimes ^{70}$Ni. The authors identified the 1518 keV state as a $p_{1/2}$ hole coupled to the 2^+ state of ^{70}Ni and suggested that the low log ft values infer a strong mixing between the two $5/2^-$ states. They also suggested that the 1821 keV state originates from a coupling of a $f_{5/2}$ hole to the 2^+ state of ^{70}Ni.

Ni isotopes

The investigation of the β-decay of the $1/2^-$ isomeric state of ^{69}Ni was reported simultaneously by Prisciandaro *et al.* [Pri99] and by Mueller *et al.* [Mue99], as mentioned before. In both papers, the authors identified a single γ-transition of 1298 keV and deduced similar intensities (an upper limit of 36% and 26(9)%, respectively) of the decay of the isomer feeding directly the ground state of ^{69}Cu. This implies a mixing of the $\pi p_{3/2} \nu p_{1/2}^{-2} g_{9/2}^2$ configuration in the $\pi p_{3/2}$ ground state of ^{69}Cu. The upper limit of the mixing probability is determined in [Pri99] as 15%, while Mueller *et al.* derived it more accurately to be 9(4)%. Using the obtained value, Prisciandaro *et al.* affirmed that such a 'small value (15%)' supports the idea that ^{68}Ni is a "double-magic" nucleus, while
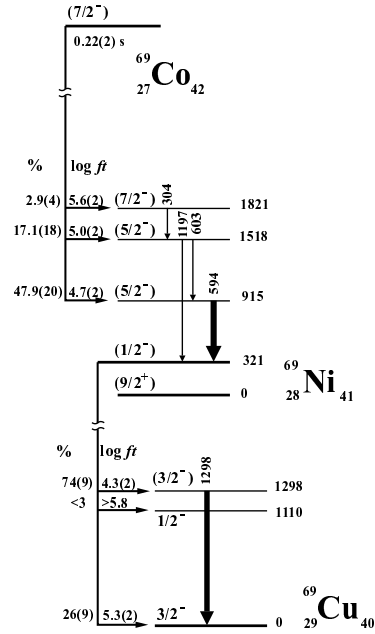
Figure 3.8: *Partial level scheme of the decay of ^{69}Co and ^{69}Ni as it is presented in [Mue99].*

Mueller *et al.* state that, even if ^{68}Ni shows some magic features, the stabilizing effect of $N = 40$ disappears with a coupling of a single nucleon to the ^{68}Ni core.

A detailed β-decay study of the Ni isotopes between ^{68}Ni and ^{74}Ni has been performed by Franchoo *et al.* at LISOL. The results were shortly reported in ref. [Fra98] and a comprehensive paper investigating the properties of ^{69,71,73}Cu is in print [Fra01]. Here, we will examine the results mainly for ^{69}Cu and some of the trends in the structure with the increasing of occupation number of the neutron $g_{9/2}$ orbital.

The level scheme deduced from the β-decay of both the 'high' and 'low-spin' states in ^{69}Ni is shown in Fig. 3.9. The $3/2^-$ ground state of ^{69}Cu is explained by the shell model as a dominating $\pi p_{3/2}$ wave-function component. A direct conversion of the $p_{1/2}$ neutron into a $p_{3/2}$ proton would create the $\pi p_{3/2}(\nu p_{1/2}^{-1} g_{9/2})_{5-}$ and $\pi p_{3/2}(\nu p_{1/2}^{-1} g_{9/2})_{4-}$ multiplets.
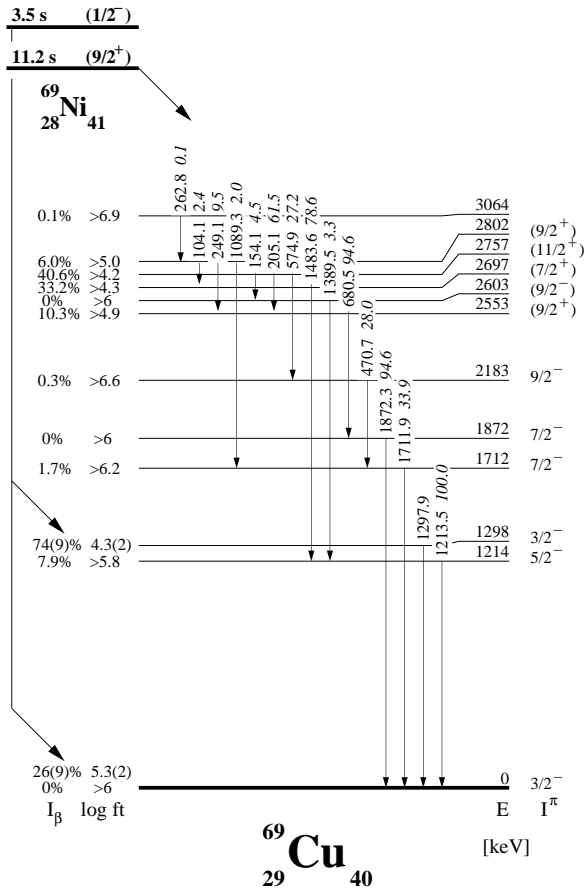
Figure 3.9: *Level scheme of the decay of ^{69}Ni as it is presented in [Fra01].*

The former one is equivalent to the coupling of a $p_{3/2}$ proton to the 5^- isomer in ^{68}Ni. The authors attributed the levels at 2553, 2697, and 2757 keV to the $9/2^+$, $7/2^+$, and $11/2^+$ members of the $\pi p_{3/2}(\nu p_{1/2}^{-1} g_{9/2})_{5^-}$ multiplet, respectively, and the level at 2802 keV as the $9/2^+$ state of the $\pi p_{3/2}(\nu p_{1/2}^{-1} g_{9/2})_{4^-}$ multiplet. Due to the selection rules of the allowed β-decay, the $13/2^+$ isomeric state, known from [Bro98], could not be populated.

The level at 1214 keV was assigned as a $\pi f_{5/2}$ proton particle state. The level at 1712 keV was interpreted as a proton $f_{7/2}$ hole state and the one at 2183 keV was seen as the $9/2^-$ member of a collective band built on this excitation.

The level at 1872 keV according to the authors has predominantly a $\pi p_{3/2}(\nu p_{1/2}^{-2} g_{9/2}^2)_{2^+}$ structure.

Franchoo *et al.* observed a strong downsloping of the proton $f_{5/2}$ orbital, with respect to the proton $p_{3/2}$ orbital, if the occupation of the neutron $g_{9/2}$ orbital increases (see Fig. 3.10). Known as a monopole shift (or monopole migration), this is attributed to the first term of the multipole expansion of the proton-neutron interaction. In two different approaches, Ji and Wildenthal [Ji89] and Sinatkas *et al.* [Sin92] manage to reproduce the known structure in the intermediate nuclei only if they fix the $\pi f_{5/2}$ orbital in ^{79}Cu far below the $\pi p_{3/2}$ state. As we will see later, this changing of the ordering and energy spacing between the proton orbitals could be responsible for some core-polarization effects inferred by some of the measured isomeric g factors.

3.2.3 Deep-inelastic reactions

Another way to produce neutron-rich nuclei is by means of deep-inelastic reactions. In this type of reaction, the energy of the projectile is well above the Coulomb barrier, and, usually, higher Z neutron-excessive materials are used as targets. Due to the tendency of the equilibration of the N/Z ratio between the projectile and the target nucleus (see, e.g., [Bro98]), more neutron-rich species can be produced. The different detection approaches, the results from which gave a significant impact on the structural information in the ^{68}Ni region, are: i) the use of a thick target and a multidetector $\gamma - \gamma$ coincidence technique [Paw94, Bro95, Bro98] and ii) the use of a thin target and an 'isomer scope' [Ish00]. In the former one, the isotope identification is based on the correlation between the γ-rays emitted simultaneously by the projectile- and target-like nuclei while in the latter one the nuclei are identified by means of
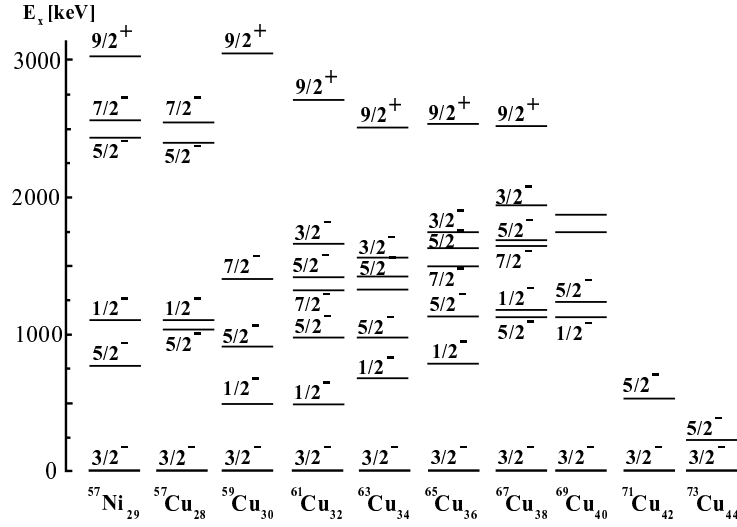
Figure 3.10: *Monopole shift of the 5/2$^-$ level in the Cu isotopes as it is presented in [Fra99].*

the $\Delta E - E$ technique.

Here, we will consider only those results which have a direct impact on the structure of the isomers discussed in this thesis.

The first report about isomers produced in a deep-inelastic reactions in the ^{68}Ni region came from Pawlat *et al.* [Paw94], who studied the neutron-rich Ni isotopes ($A = 64$ to 67) produced in ^{208}Pb + ^{64}Ni collisions. Besides obtaining significant information on the studied isotopes, the authors also reported for the first time a long-lived isomer ($t_{1/2} > 0.3\mu$s) in ^{67}Ni. The peculiarity of the experiment did not allow them to measure the half-life of the isomer with better precision. They defined the excitation energy of the isomer (1007 keV), the two de-exciting γ-ray transitions (313 keV and 694 keV) and made a tentative spin/parity assignment of 9/2$^+$ implying a $\nu p_{1/2}^{-2} g_{9/2}$ structure.

Being proposed as a doubly-magic nucleus, ^{68}Ni attracted great experimental interest. Its studies by deep-inelastic reactions are reported in ref. [Bro95, Ish00]. Broda *et al.* [Bro95] first measured the 2$^+$ state at 2033 keV and also identified a (5$^-$) isomeric state at 2847 keV (see Fig. 3.11). From the measured half-life of the isomeric transition ($t_{1/2} = 0.86(5)$ ms), they deduced its transition rate of $B(E3, 5^- \to$

2^+) = 0.022 W.u. Performing shell-model calculations, using an inert ^{56}Ni core, $p_{3/2}$, $f_{5/2}$, $p_{1/2}$ and $g_{9/2}$ valence orbitals and realistic two-body matrix elements derived by Sinatkas *et al.* [Sin92], Broda *et al.* obtained a quite pure isomeric configuration. The $\nu p_{1/2}^{-1} g_{9/2}$ accounted for 79% of the wave-function while the remaining strength was scattered over several different configurations with less than 10% each.
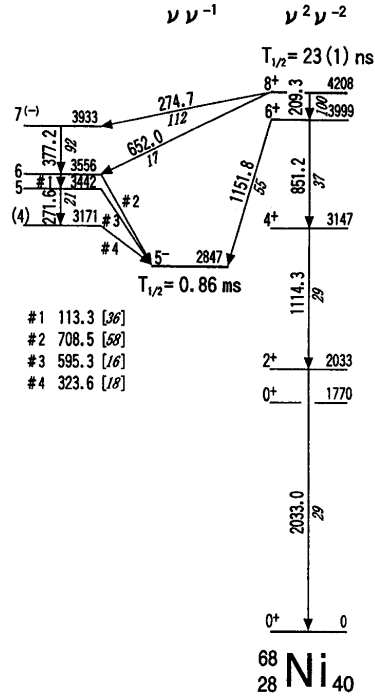

Figure 3.11: *Level scheme of* ^{68}*Ni as presented in [Ish00].*

Another possible isomeric configuration in ^{68}Ni is the $2p-2h$ $(g_{9/2}^2)_{8^+}$ state. It was established in a later work by Ishii *et al.* [Ish00]. The half-life of the 4208 keV isomeric state was measured to be 23(1) ns. Two different paths of the de-excitation of the isomer were observed (see Fig. 3.11): i) a stretched $E2$ cascade ($8^+ \to 6^+ \to 4^+ \to 2^+ \to 0^+$), which identified undoubtedly the proposed isomer configuration, and ii) a decay to a $1p-1h$ structure, connected to the 5^- isomer. The $1p-1h$ structure

was interpreted as a member of the $\nu f_{5/2}^{-1} g_{9/2}$ multiplet, which was later confirmed in β-decay studies [Mue00]. Note that the ordering of the last two γ-ray transitions and the position of the lowest observed state in the multiplet are at variance with those proposed by Mueller *et al.* [Mue00] and discussed in the previous section.

Another isomer, the g-factor measurement of which is a subject of this thesis, is the $13/2^+$ isomer in ^{69}Cu. Considered as one proton coupled to the ^{68}Ni core, ^{69}Cu was also studied in detail in an attempt to shed more light on the structure in the region. In the previous section, we have discussed the results of the β-decay studies of Franchoo *et al.* and here, we will elaborate more on the results of the deep-inelastic-reaction studies. Firstly, Broda *et al.* reported the observation of the isomeric state. They measured its half-life ($t_{1/2} = 0.33(8)\mu$s) and the de-exciting transitions and proposed that the isomer represents a coupling of the $p_{3/2}$ proton to the $(\nu p_{1/2}^{-1} g_{9/2})_{5^-}$ isomer observed in ^{68}Ni. Constructing the level scheme (see Fig. 3.12) and establishing its excitation energy of $E_x = 2742 keV$, they found that this excitation level is not observed in the β-decay studies of ^{69}Ni which populates with quite low log ft values states with similar excitation energies. This was one of their main points to make the assignment of $I^\pi = 13/2^+$ for the isomer, a state which belongs to the $\pi p_{3/2} \nu p_{1/2} g_{9/2}$ multiplet and which cannot be populated in an allowed Gamow-Teller decay. Broda *et al.* also proposed an $f_{5/2}$ proton-particle configuration for the 1213 keV state and an $f_{7/2}$ proton-hole for the 1711 keV. They interpreted the 1871 keV level as arising from a 2^+ ^{68}Ni core excitation, coupled to a $p_{3/2}$ proton.

In the work of Ishii *et al.* [Ish00], the level scheme of ^{69}Cu was extended (Fig. 3.12) and two new isomeric states were discovered. They measured the angular distributions for most of the γ-ray transitions, which gave a firm assignment of their multipolarities. The authors assigned $I^\pi = 19/2^-$ to the 22(1) ns isomer and interpreted it as a coupling of a $p_{3/2}$ proton to the 8^+ isomer in ^{68}Ni. Ishii *et al.* called the $13/2^{(-)}$ to $7/2^-$ levels a $\pi^2 \pi^{-1}$ band and interpreted it as a proton $2p - 1h$ excitation with a $\pi(p_{3/2}^2, p_{3/2} f_{5/2}, f_{5/2}^2)\pi f_{7/2}^{-1}$ configuration, as also suggested by Broda *et al.*. They concluded that this band has a collective character with a significant $E2$ strength competing with the dominating $M1$ transitions. This interpretation, as we will see in section 3.3.3, can have a significant impact on the angular distribution measured via TDPAD.

With this we will conclude with the results of the deep-inelastic reactions studies and will consider some other information on the structure
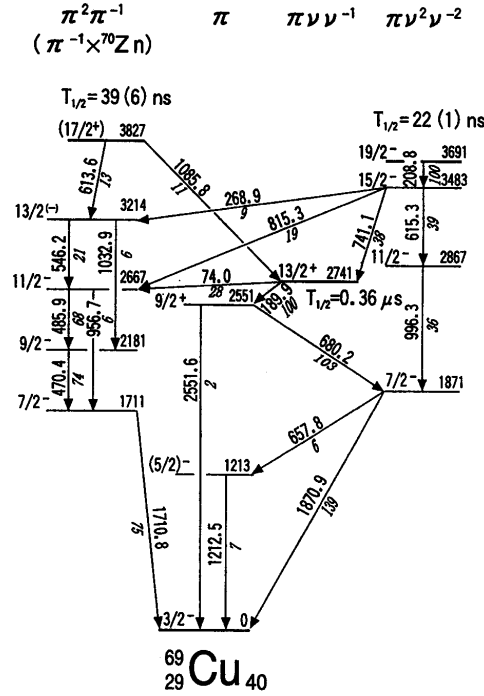
Figure 3.12: *Level scheme of ^{69}Cu as presented in [Ish00].*

of the isomers under investigation.

3.2.4   Projectile-fragmentation reactions

Studies of neutron-rich nuclei, produced in projectile-fragmentation reactions, have several advantages as well as some disadvantages. The advantages are that one can go much farther away from the stability and that the production and separation mechanism itself can be used for precise ion identification. On the other hand, there is a limit on the half-life of the nuclear states which can be investigated. This limit is imposed by the time of flight of the radioactive ions from the production target through the separator to the experimental setup and is usually of the order of a few tens to a few hundreds of ns.

Grzywacz *et al.* [Grz98] reported the observation of a number of isomeric states in the vicinity of ^{68}Ni produced in a projectile-fragmentation

reaction. Besides all new isomers, they also measured more precisely the half-life of the $13/2^+$ state in ^{69}Cu ($t_{1/2} = 0.36(5)\mu$s) and the $9/2^+$ state in ^{67}Ni ($t_{1/2} = 13.3(2)\mu$s). From the latter one they derived the transition strength as $B(M2) = 0.047$ W.u., which fixed undoubtedly the interpretation of this isomer as a $\nu g_{9/2}$ state decaying to the $\nu f_{5/2}^{-1}$ level. In the same work also two new isomeric states in ^{66}Co were identified. For the shorter-lived state, the half-life was measured and the multipolarity of the de-exciting 175 keV transition was inferred as $E2$. For the longer-lived state, only a lower limit of 100 μs was obtained and three de-exciting transitions of 252 keV, 214 keV, and 175 keV were measured.

Another experiment in which a projectile-fragmentation reaction was used for the production of nuclei in the vicinity of ^{68}Ni is the one reported in Ref. [Mac01]. There, an array of four BaF$_2$ detectors was employed to search for level half-lives in the nanosecond and sub-nanosecond region (from 20 ns down to ≈ 10 ps). Between the measured half-lifes in the transitions below the isomeric states in ^{67,69,70}Ni and ^{71,72}Cu, is also the 694 keV transition in ^{67}Ni. From the obtained half-life of $t_{1/2} = 157(10)$ ps, the authors derived a transition rate of $B(E2) \approx 1.4$ W.u., which is in very good agreement with the theoretical calculations, and which is an additional confirmation of the type of the assigned $E2$ character of the $5/2^- \rightarrow 1/2^-$ transition.

To conclude with the overview of the experimental data on the structure in the ^{68}Ni region, we also have to mention the magnetic dipole moment measurements of the ground states in ^{67}Ni and ^{69}Cu. The results reported by Rikovska *et al.* [Rik00], $\mu(^{67}$Ni; $I^\pi = 1/2^-) = +\, 0.601(5)$ μ_N and $\mu(^{69}$Cu; $I^\pi = 3/2^-) = +\, 2.84(1)$ μ_N, have been reproduced very well by the theoretical calculations and firmly assigned the ground state configurations as $\nu p_{1/2}$ and $\pi p_{3/2}$, respectively.

3.3   Experimental details

3.3.1   Production and selection of the isomeric states of interest

For the production of the nuclear states of interest we used a projectile-fragmentation reaction mechanism. A primary beam of ^{76}Ge was accelerated, by the two coupled cyclotrons at GANIL, to 61.4 MeV/u and it impinged on a 145 mg/cm^2 ^{9}Be target, which was positioned at the entrance of the LISE [Ann87] fragment separator. The target was mounted on a rotating target wheel, which was inclined at 47.7^o to obtain an effective thickness of 145 mg/cm^2 - an optimal value for the production of the desired nuclides. A 220.5 μm Be wedge-shaped degrader was used to select the fragments with given mass-to-charge ratio. A schematic drawing of the experimental areas at GANIL can be found in Fig. 3.13. In order to diminish the in-flight decay of the isomeric states, we tried to shorten their path between the production and the implantation point by positioning our setup at the first focal plane after the second dipole magnet of LISE (see Fig. 3.13). This way, the total time of flight of the ions from the target to our setup was estimated to be $\sim$ 200 ns.

The nuclei around ^{68}Ni were separated in-flight using the LISE spectrometer and were implanted in a stopper foil in the center of the TDPAD setup. With this experiment, we were aiming at three different isomeric states (see Fig. 3.14) in ^{69}Cu ($t_{1/2} = 0.35\mu s$, $E_x = 2740$ keV), ^{67}Ni ($t_{1/2} = 13.3\mu s$, $E_x = 1007$ keV) and ^{66}Co ($t_{1/2} = 0.839\mu s$, $E_x = 175$ keV), whose half-lives and expected g factors were suitable for a TDPAD measurement. Since the production cross-section for ^{66}Co was the smallest between the three of them, we made the selection with LISE in a way that the center of the momentum distribution (highest yield) was selected for ^{66}Co. This gave us in the same setting also ^{69}Cu and ^{67}Ni with a reasonable intensity. A schematic drawing of the simulations done by the LISE programme [Baz01] for the momentum distribution and selection can be found in Fig.3.15. In these calculations we use a constant fragment velocity ($V_{fragment}/V_{beam} = 1$). This gives a production of the different isotopes in agreement with the experimental results. The other options (like calculations of the fragment velocity by different methods) give production rates, not consistent with the experimentally observed ones.

Let us now consider in more detail the TDPAD setup (see Fig. 3.16). It consisted of a silicon ΔE detector, an implantation host, γ-ray detec-
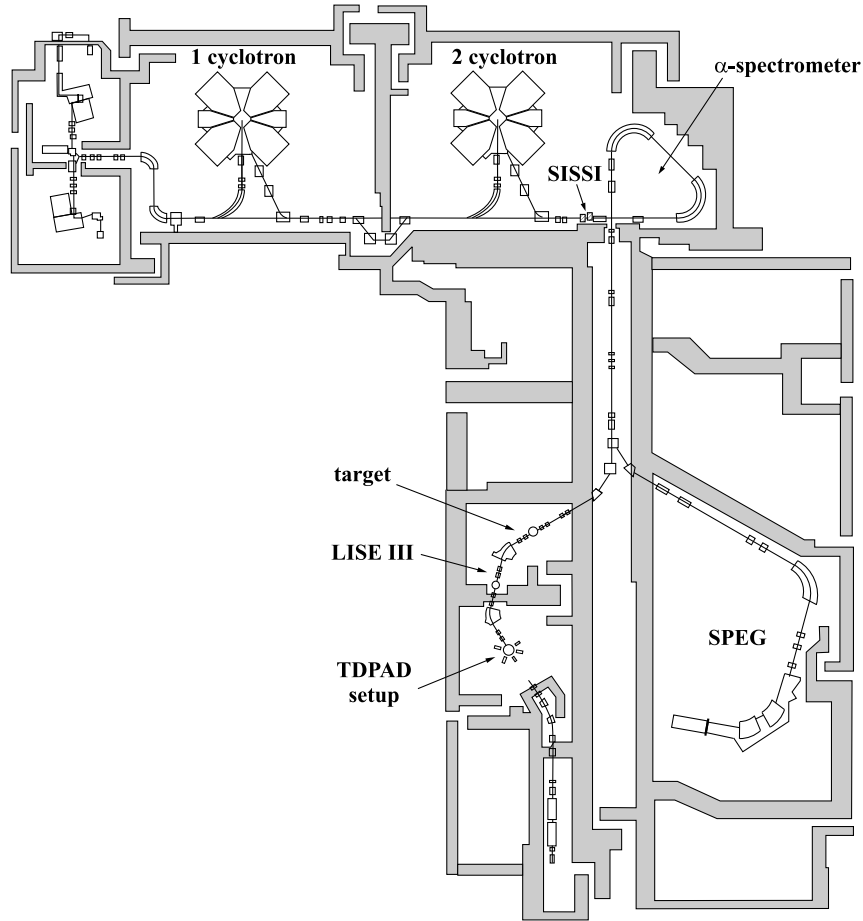
Figure 3.13: *Schematic drawing of the experimental areas at GANIL.*

tors and an electromagnet, producing a constant magnetic field in the vertical direction. The value of this field was set to $B = 0.375(7)mT$ during the experiment. The quoted error on B includes also its inhomogeneity over the beam spot (1.5 cm × 1.5 cm). The rotation of the spin-oriented ensembles, caused by the vertical magnetic field, was monitored by the γ-ray detectors positioned in the horizontal plane. Two of them were high-efficiency Ge Clovers [Duc99, She99], which were at 0°
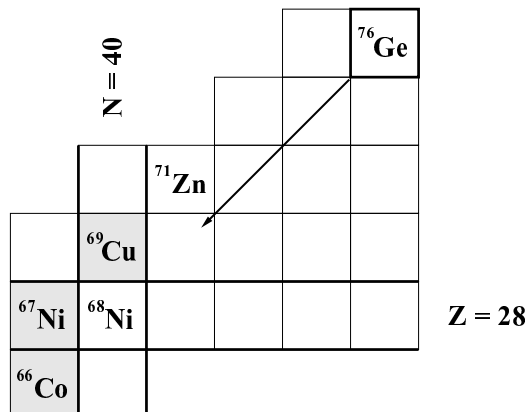
Figure 3.14: *Part of the nuclear chart with the relative position of the primary beam (^{76}Ge) and some of the selected isotopes. The isomers, which g factors were measured, are shadowed.*
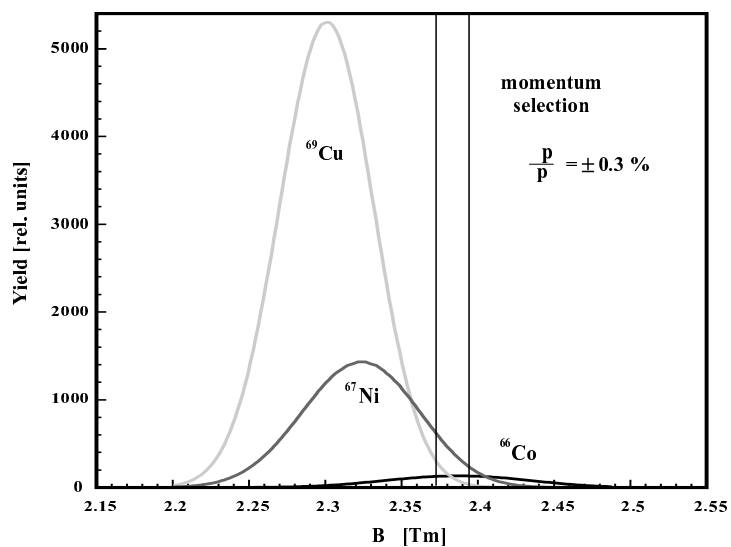

Figure 3.15: *Momentum selection.*

and 90° with respect to the incoming beam. Three BaF$_2$ detectors were positioned at $\pm 45^o$ and -135°, respectively. We have chosen a 125 μm high purity ($> 99.99\%$) Cu foil as an implantation host. It was annealed in order to decrease any possible defects created during its production. The Cu has a cubic crystal structure and the ions of Cu, Ni and Co are expected to implant well in copper as they have the same electronegativity and very similar atomic radii [HR69]. In front of the stopper a 250 μm Al foil was used as a beam degrader. The stopper and degrader foils and the 300 μm silicon detector in front of them were positioned in a vacuum chamber connected to the beam line.
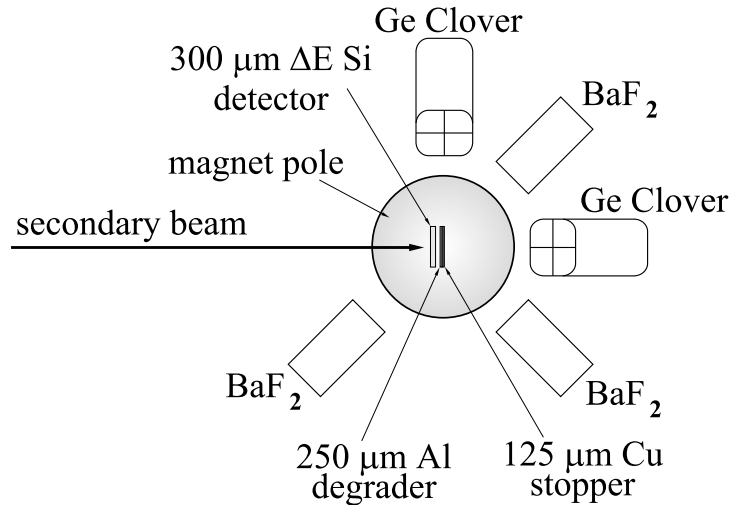
Figure 3.16: *A schematic drawing of the TDPAD setup (top view).*

Each of the ions passing through the ΔE detector gave a starting signal for the time spectra, triggering the data acquisition system (DAQ) and opening a 20 μs time-window. A γ-ray registered within this time-window by any of the Ge or BaF$_2$ detectors gave a validation for the DAQ. The ΔE detector was also used for the ion-identification, based on the energy-loss *vs.* time-of-flight technique [Baz90]. The start signal for the time-of-flight was given by an ion detected in the ΔE detector and the stop signal came from the HF of the cyclotron. A two-dimensional histogram with a sample run from the experiment is presented in Fig. 3.17. The calculations, performed with the LISE program for the energy-

loss *vs.* time-of-flight showed, that there are some contaminations from lighter isotopes also present in this plot. They are transmitted through the fragment separator as lower charge state (non fully stripped). However, the intensity of the charge state contaminations is 3 to 4 orders of magnitude lower, compared to the fully stripped ions. The cuts, created on the base of these two-dimensional histograms, were used to impose isotope conditions on the energy and the time spectra for each of the γ-ray detectors. These projections for the different nuclides were used for the γ-ray and the time analysis and also to obtain the TDPAD curves.
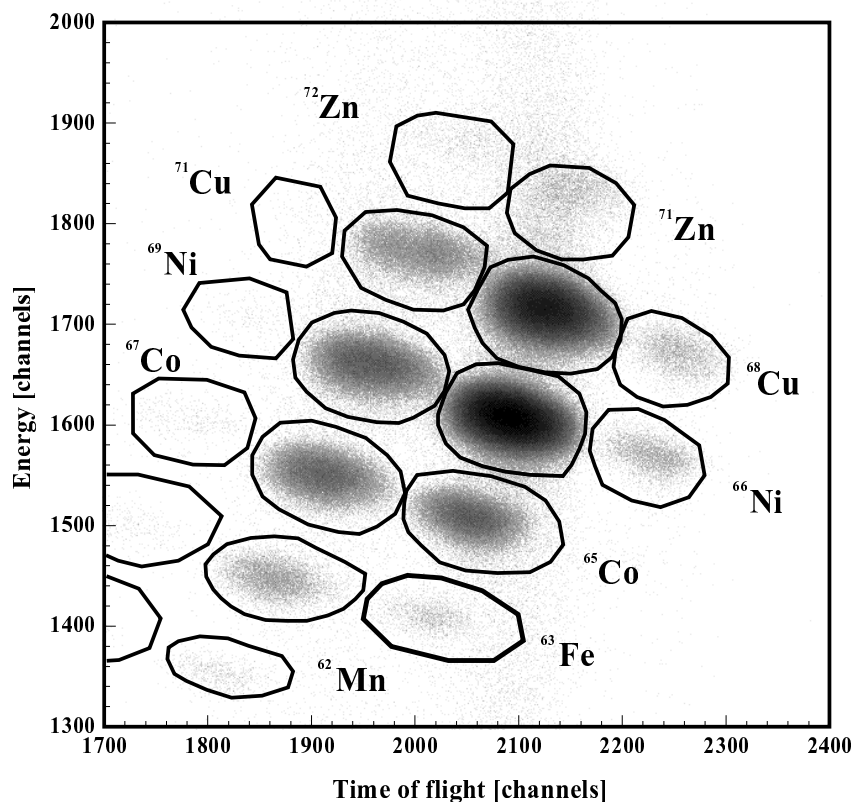

Figure 3.17: *Two-dimensional histogram of energy-loss vs. time-of-flight. The Z-axis is in logarithmic scale. The full variety of nuclides, implanted in the Cu foil during the experiment, is identified.*

3.3.2 γ-ray and time analysis

As it was mentioned in Chapter 1, to deduce the g factor of an isomeric state by applying the TDPAD method, one has to measure the intensity of the isomeric decay as a function of the time. Thus the time structure of the data acquisition, the $t = 0$ identification and the time calibration are important issues. Furthermore, the proper selection of the correct γ-ray transition is also important. In this section we are going to discuss these two issues for the whole variety of nuclides, identified in the experiment (see Fig. 3.17).

Time structure and time calibration

As it was mentioned before, each of the heavy ions, implanted in the Cu foils, passed through the silicon ΔE detector where its energy and time signals were registered. The time signal was used to open a 20 μs window of the data-acquisition cycle (see Fig. 3.18). During this time window, the data acquisition (DAQ) was waiting for a validation signal from any of the γ-detectors. If such a signal would arrive, the event would be recorded on the tape, otherwise it would be rejected.
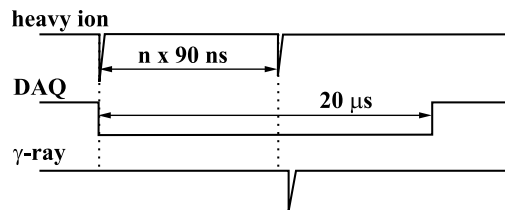
Figure 3.18: *Time structure of the events and the data acquisition cycle. Every γ-ray, detected in the 20 μs time window after the start given by arrival of the heavy ion, is accepted as an event.*

This time structure of the data acquisition has the following consequences:

- it is possible that within this time window a second heavy ion is implanted. Taking into account the structure of the cyclotron beam, the time difference between the incoming ions is a multiple of 90 ns (the HF of the cyclotron was 11.1100 MHz). In such a case, if a γ-ray is detected, it is unclear from which of the heavy ions

it came. If the second ion is the source of the detected γ-ray this will create a random background (both in energy and time), the intensity of which depends on the implantation rate. We estimated the significance of such random event for the case of ^{67}Ni - the most intensely produced and having the longest half-life isomer. With a typical total rate of 5000 - 8000 implanted heavy ions (of which 2700 ^{67}Ni) per second and $\approx$ 10 counts/s of the 313 keV line (^{67m}Ni), detected in the photopeak in a Ge Clover detector, we estimated that less than 5% of the events are with a 'wrong' time stamp and contribute to the background. For this calculation we used the standard formula for accidental coicidences (see *e.g.* [Leo94])

$$Accidentals = \sigma N_1 N_2 \qquad (3.1)$$

where N_1 and N_2 are, respectively, the single counting rates for the for the two branches, whose accidental coincidence we calculate, and σ is the time resolution of the system (20 μs in this particular calculation). Since the other implanted isotopes had lower implantation rate compared to ^{67}Ni, the percentage of the random events in any of their γ-lines should be lower.

- each of the implanted heavy ions creates a flash of prompt radiation with a broad energy spectrum. If one creates a time spectrum with very broad energy conditions, then the spikes of the prompt flash will appear regularly in time intervals of 90 ns (see Fig. 3.19 b)). Using this feature, we could make a very precise time calibration (better than 0.1%) and we eventually obtained time spectra with 5 ns/ch. This gave us a 'working interval' of the time-to-amplitude converters (TAC) of 17 μs.

- there is a probability that a heavy ion triggers the DAQ system and does not create a γ-ray, which is detected by the γ-ray detectors. If during the 20 μs after the implantation of the ion a γ-ray with different source is detected by the detectors, it will be wrongly correlated with the implanted heavy ion. In this way, we also got in our spectra γ-lines from long-lived activities like β-decay or long-lived isomers.

For the $t = 0$ identification we used the prompt flash from the triggering ion (see Fig. 3.19 a)) and all time spectra were shifted, so that the prompt peak for each of the TAC spectra appeared at one and the same channel. We chose this to be channel 50.
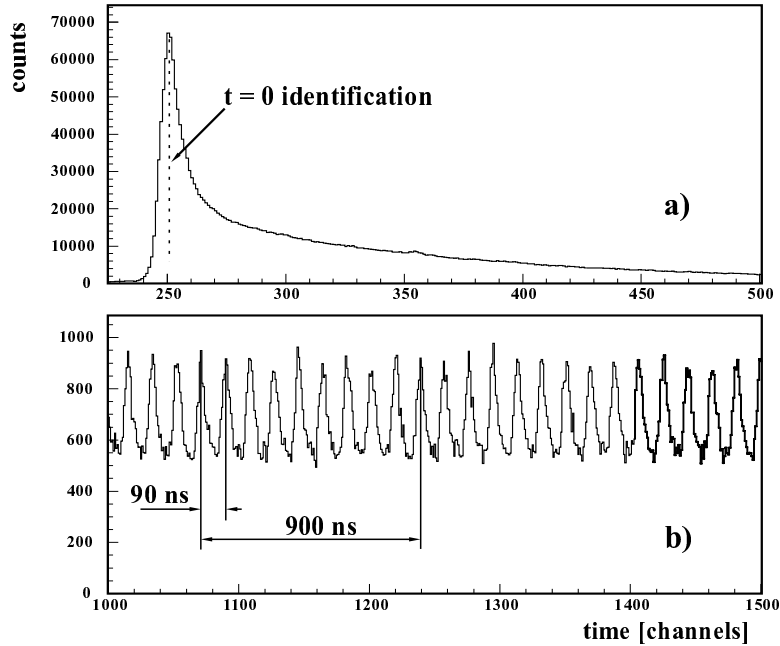
Figure 3.19: *A "raw" time spectrum from a Ge Clover detector, produced with broad energy conditions (50 keV - 2500 keV) in order to make (a) the t = 0 identification, using the first few hundred channels of the TAC range and (b) the time calibration, using the γ-flash seen every 90 ns after most isomers have decayed.*

The energy calibration of the γ-detectors was done using an ^{152}Eu source. The typical energy resolution of the Ge Clover detectors was 2.7 - 2.9 keV (FWHM) at $\sim$ 1200 keV.

To proceed further, we will examine the results for the different isotopic chains, observed in the experiment. We created energy and time-spectra for each of the isotopes presented in Fig. 3.17. As a first step the energy spectra were produced for two different time windows: i) the full time window (0 - 17 μs); and ii) a much shorter time window including the immediate ion implantation (0 - 1 μs). Comparing the relative intensity of the γ-lines in the two spectra, one should be able to distinguish between γ-rays produced by short and long-lived states. The shorter-

lived states should show enhanced intensities, with respect to the other γ-lines, in the narrow time window. Afterwards, we produced time spectra for each of the observed isomeric transitions and their half-life was derived. With this procedure we are limiting ourselves to shorter-lived isomeric states. Here, we will present the results only for the isotopes, in which isomeric transitions were observed.

Zn isotopic chain

Two Zn isotopes were observed in this experiment: ^{72}Zn and ^{71}Zn. No isomeric transitions were found for ^{72}Zn. However, in the energy spectra gated on ^{71}Zn, we found a γ-line which was clearly enhanced in the short time window (see Fig. 3.20). Its energy (128 keV), was not observed in any other energy spectra and was also not identified as coming from a known contamination. There were no other γ-lines found to be in coincidence with this transition.
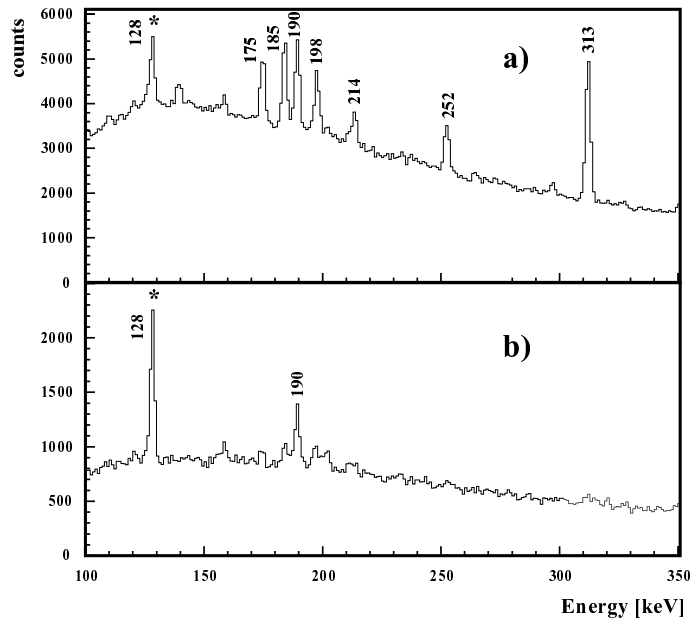

Figure 3.20: *Energy spectra for ^{71}Zn produced (a) for the full time window and (b) for the first 1 μs only.*

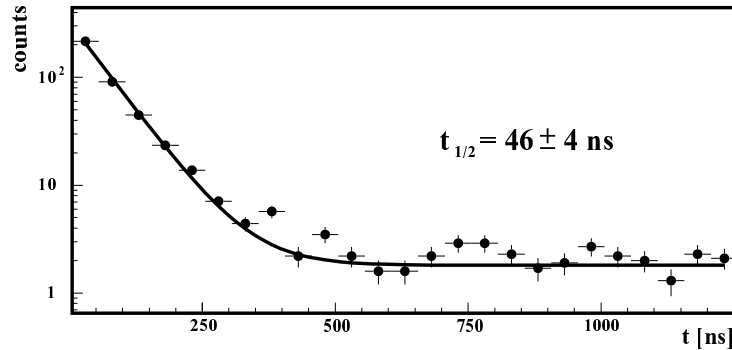The time spectrum, gated on the 128 keV line (see Fig. 3.21) revealed a half-life of $t_{1/2} = 46 \pm 4$ ns.

Figure 3.21: *Time spectrum for the 128 keV transition of ^{71}Zn.*

^{71}Zn was studied in transfer reactions [Ehr67] and also via the β-decay of ^{71}Cu [Run83]. Von Ehrenstein and Schiffer identified in their work the ground state of ^{71}Zn as $J^{\pi} = 1/2^{-}$, an excited state at 157 keV with $J^{\pi} = 9/2^{+}$ and also a state at 285 keV, for which they measured the angular momentum transfer $l = 2$. Here, we will not consider the rest of the states measured by them. The tentative assignment which they gave for the 285 keV state was $J^{\pi} = 5/2^{+}$.

Runte *et al.* [Run83] studied ^{71}Zn via the β-decay of ^{71}Cu and derived the level scheme presented in Fig. 3.22. They measured only relative β-intensities and they did not deduce log ft values. They also tentatively confirmed the $J^{\pi} = 5/2^{+}$ assignment of the 486 keV level in ^{71}Zn, based on the relatively high β-decay branch to it. The measured magnetic moment of the 158 keV state ($\mu = (-)1.035(18)\mu_N$ [Her89]) also confirms its $9/2^{+}$ assignment.

We can conclude that the 128 keV γ-line, which we observed in our experiment, is identical with the transition between the 286 and 158 keV levels observed both in transfer reactions and in β-decays studies. The half-life which we measured ($t_{1/2} = 46(4)ns$) is consistent with the assumption of an $E2$ transition. We calculated the reduced transition probability to be $B(E2) = 16.4 \pm 1.4$ *W.u.*, using for this calculation the internal electron conversion coefficient $\alpha = 0.26$ from Ref. [Ros78]. Other transition multipolarity assignments are much less probable. Thus our lifetime measurement confirms the $5/2^{+}$ assignment of the 286 keV
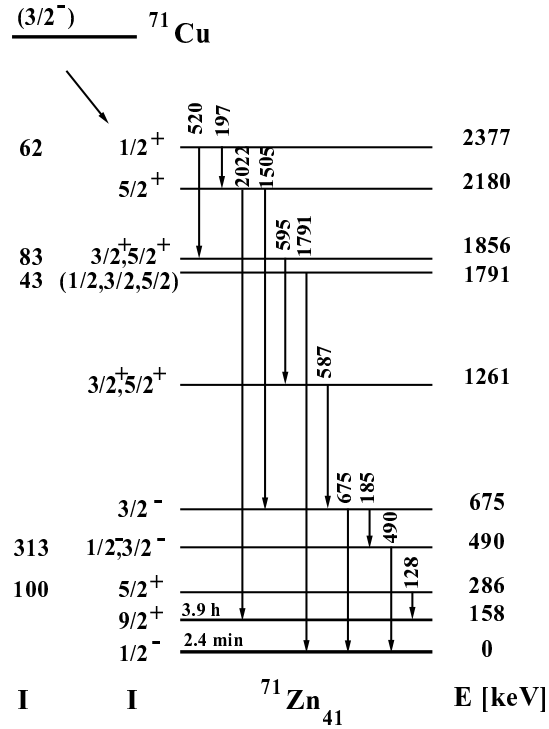
Figure 3.22: *The level scheme of* ^{71}*Zn from the* β*-decay study of Runte et al. [Run83].*

level in ^{71}Zn.

Cu isotopic chain

In this experiment, we selected the Cu isotopes with mass from 68 to 71. We did not detect any γ-rays, correlated with the implantation of ^{68}Cu and ^{70}Cu. However, isomers were observed in the odd-mass Cu isotopes.

The $t_{1/2} = 275(14)$ ns isomer in ^{71}Cu was previously known from an isomer search after a projectile-fragmentation reaction [Grz98]. The production of ^{71}Cu in our experiment was very low, which allowed us only to observe some of the most intense γ-lines (see Fig. 3.23).

The time spectrum, produced by the selection of the four most intense γ-lines (133 keV, 494 keV, 939 keV and 1189 keV), is shown in Fig. 3.24.

Figure 3.23: *Energy spectrum of ^{71}Cu, produced for the first one microsecond time window. Only the most intense γ-lines from the decay of the isomer (marked with asterisk) can be observed.*

From the fit of this spectrum, we obtained a half-life ($t_{1/2} = 252(35)$ ns) which is in agreement with the previously measured value ($t_1/2 = 275(14)$ ns) [Grz98].

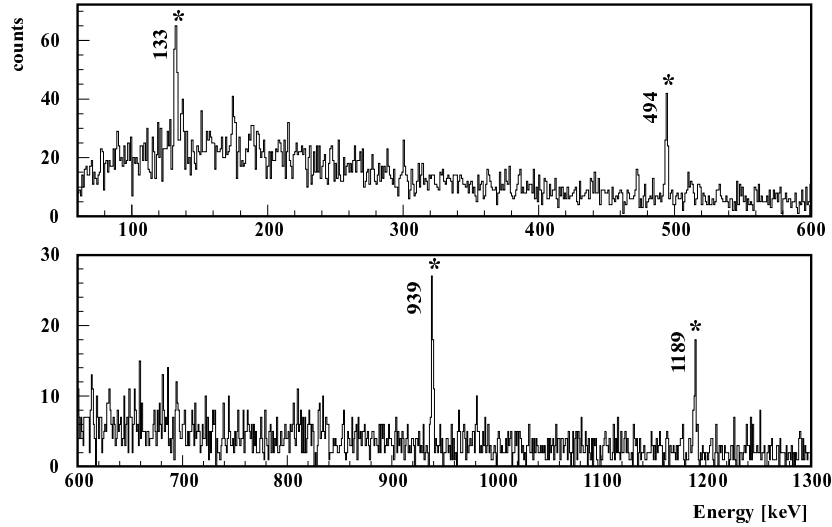^{69}Cu was one of the most intensely produced isotope in our experiment. We also measured the g factor of its $13/2^+$ isomer. Therefore, we will examine the energy and the time spectra of ^{69}Cu in more detail.

The energy spectrum obtained by a gate on the arrival of the ^{69}Cu ions and summed over all crystals of the Ge CLOVER detectors is shown in Fig. 3.27. Note that the spectrum is plotted in logarithmic scale in order to show all contaminations. The identification of the different γ-lines is presented in Table 3.3.2.

Gating on the energies of the isomeric transitions, we produced the time spectra for each of the isomeric γ-lines. These time spectra were afterwards analyzed to obtain the decay time of the isomer. A typical picture of a time spectrum, consisting of a sum of all crystals of the Ge CLOVER detectors, is shown in Fig. 3.25.

The range of the time-to-amplitude converters (TAC) was set to 20 μs. Note that due to the different $t = 0$ positions, which were usually
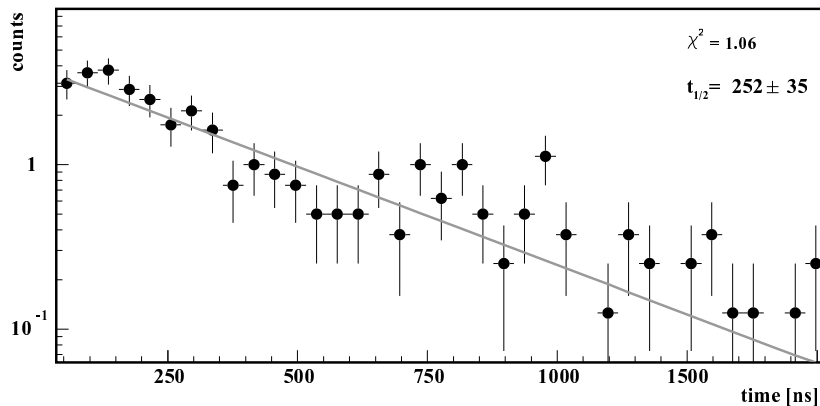
Figure 3.24: *Time spectrum of ^{71}Cu, produced by a gate on the four most intense γ-lines (133 keV, 494 keV, 939 keV and 1189 keV).*

set at a few hundred channels from the start of the TAC (see Fig. 3.19), their useful range is ≈ 17 μs. One can clearly identify two different regions in the spectrum - a) an exponential decay of the isomer and b) a constant background.
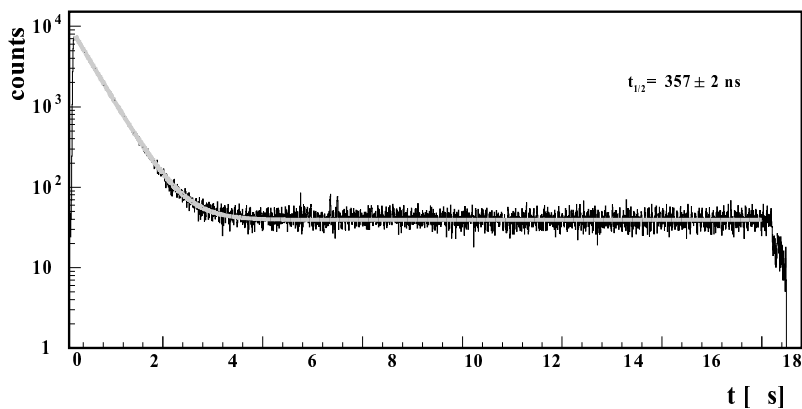
Figure 3.25: *Time spectrum obtained for the sum of the 4 segments of the second CLOVER detector for the 190 keV transition. The line is from a fit using an exponential function plus constant background.*

Analyzing all isomeric transitions, we obtained the half-lives depicted in Fig. 3.26. From their weighted mean value, we derived the average half-life of the isomer $t_{1/2} = 357(2)$ ns, which has a much higher precision compared to the previously obtained value of 360(50) ns [Grz98].

To check the influence of the recovery time of the Ge detectors on the obtained half-life, we made several fits of the 190 keV transition time spectrum, changing the starting time of the fit. The resulting change of the half-life obtained form these fits was less than 1 ns while the difference in the starting time of the fits was up to 350 ns. This shows that the influence of the recovery time of the Ge detectors on the obtained half-life is negligible.
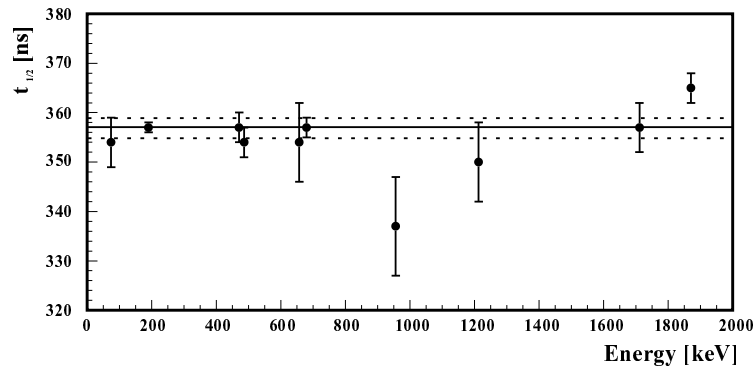
Figure 3.26: *Life-time measurements for the different transitions from the decay of the isomer in ^{69}Cu. The full line represents the mean value and the dashed lines are the uncertainties of the derived half-life of the isomer.*

Table 3.2: *Most intense γ-lines observed in the energy spectrum with a gate on ^{69}Cu. The transitions coming from the decay of the isomer are marked in bold.*

E_γ [keV]	origin	E_γ [keV]	origin
74	^{69m}**Cu**	835	^{72}Ge(n,n'γ)
175	^{66m}Co	844	^{27}Al(n,n'γ)
190	^{69m}**Cu**	847	^{56}Fe(n,n'γ)
198	^{71m}Ge	868	^{74}Ge(n,n'γ), ^{73}Ge(n,γ)
205	^{69}Ni (9/2$^+$) β-decay	885	^{70}Cu β-decay
214	^{66m}Co	901	^{70}Cu β-decay
252	^{66m}Co	**957**	^{69m}**Cu**
313	^{67m}Ni	1007	^{69}Cu β-decay
386	^{71m}Zn β-decay	1040	^{70}Ge(n,n'γ)
470	^{69m}**Cu**	1077	^{68}Cu β-decay
486	^{69m}**Cu**	1129	^{62}Co β-decay (charge state)
511	annihilation	**1213**	^{69m}**Cu**
531	^{69}**Cu** β-decay	1251	^{70}Cu β-decay
575	^{69}Ni (9/2$^+$) β-decay	1298	^{69}Ni (1/2$^-$) β-decay
596	^{74}Ge(n,n'γ), ^{73}Ge(n,γ)	1360	escape peak of 1871 keV
658	^{69m}**Cu**	1460	^{40}K
680	^{69m}**Cu**	**1710**	^{69m}**Cu**
694	^{67m}Ni	**1871**	^{69m}**Cu**
814	^{68m}Ni		
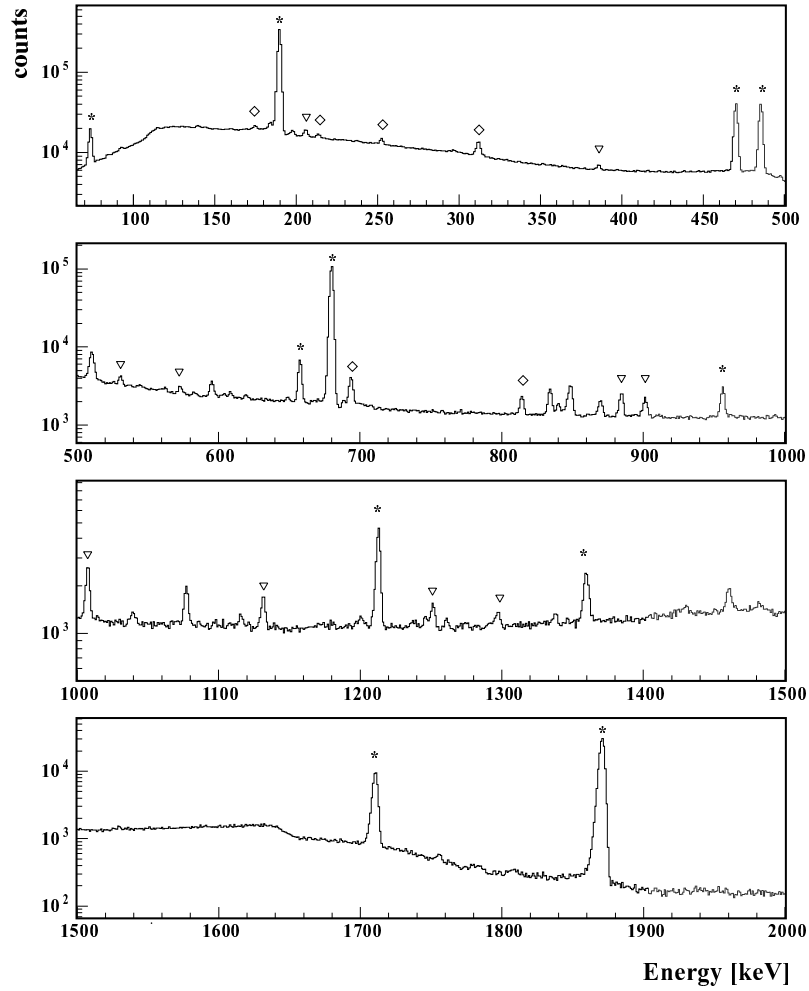
Figure 3.27: *Energy spectrum for the γ-rays correlated to the arrival of ^{69}Cu ions. * -transitions belong to the decay of the 13/2$^+$ isomer; ◇- lines come from other isomers selected in the same settings of the spectrometer; ∇ - contamination lines from β-decay; the unmarked lines mostly come from (n, n'γ) reactions and from natural radioactivies.*

Ni isotopic chain

The Ni isotopes, which we detected in our experiment are $^{66-69}$Ni. We did not find any isomeric transitions in ^{66}Ni. However, we did observe the already known isomeric transitions in the other three isotopes.

The isomer in ^{69}Ni ($t_{1/2} = 439(3)$ ns) was discovered by Grzywacz *et al.* [Grz98]. In our experiment we detected all of the γ-lines previously assigned [Grz98] to ^{69m}Ni. The energy spectrum, shown in Fig. 3.28, was produced for the first one microsecond time window. Using all observed
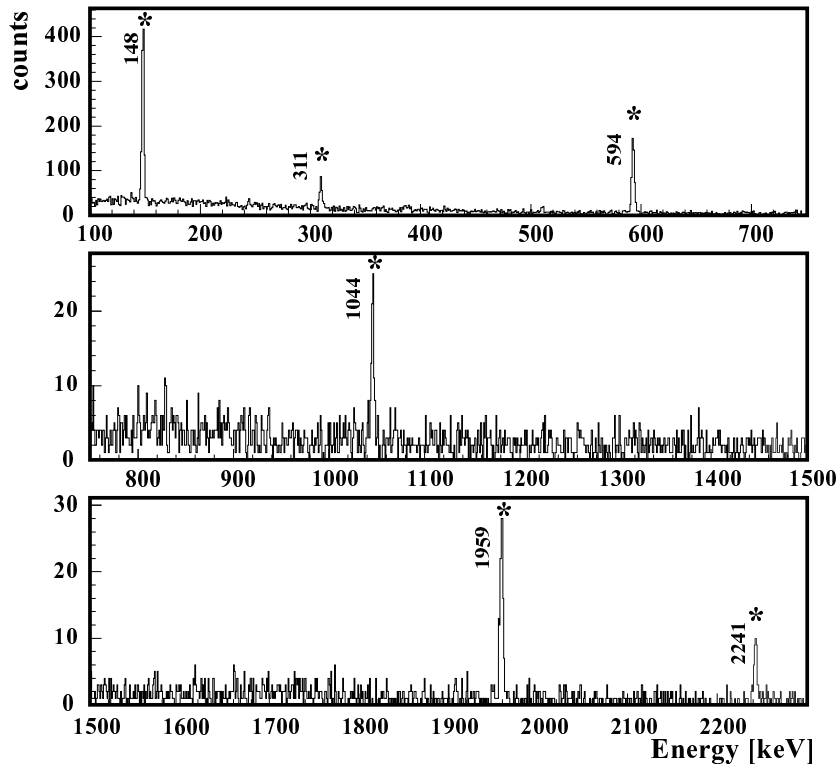
Figure 3.28: *Energy spectrum, gated on the implantation of ^{69}Ni ions, for the first one μs time window. The γ-lines, originating from ^{69m}Ni are marked with asterisk.*

γ-lines we obtained the time spectrum depicted in Fig. 3.29. Its fit gave a half-life for the isomer of $t_{1/2} = 397(20)$ ns, which is a bit smaller value

but in agreement with the previous reported $t_{1/2} = 439(3)$ ns [Grz98].
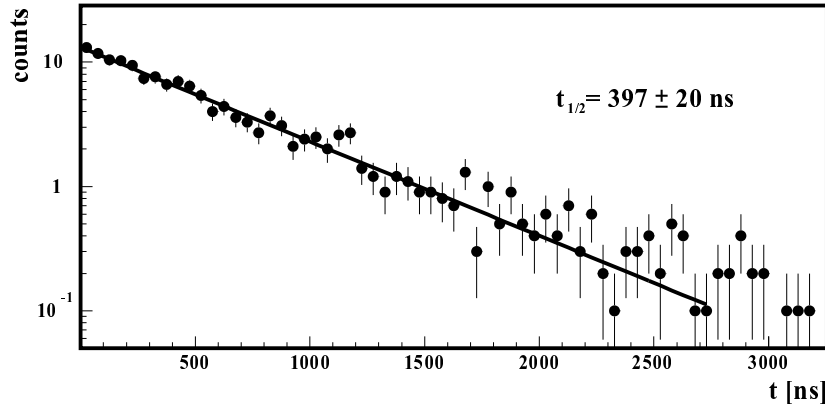
Figure 3.29: *Time spectrum, produced by a gate on all observed γ-lines in* ^{69}Ni *(148 keV, 311 keV, 593 keV, 1044 keV, 1959 keV and 2241 keV).*

The γ-decaying isomer in ^{68}Ni was discovered by Broda *et al.* [Bro95] in deep inelastic reactions. They also measured its half-life, $t_{1/2} = 0.86(5)$ ms. Since this isomer is very long-lived compared to the time-window of observation in our experiment ($\sim 17\mu$s) we could not give any value for its half-life. The energy spectrum, obtained for the full time-window (0-17 μs) is presented in Fig. 3.30. Among the other γ-lines, coming from long-lived contaminations, we clearly observe the two γ transitions from the 5^- isomer in ^{68}Ni (814 keV and 2033 keV).

^{67}Ni was very intensely produced in our experiment. We also measured the g factor of its $9/2^+$ isomeric state. Therefore, we will examine its energy and time-spectra in more detail.

The energy spectrum, shown in Fig. 3.31, comes from the full time window (0 - 17 μs). One can clearly distinguish the two transitions (313 and 694 keV) belonging to the decay of the $9/2^+$ isomer. The other lines which one can also observe are contaminants either from other isomers selected in the same settings of the fragment separator or coming from β-decay, $(n, n'\gamma)$ reactions or natural radioactivity. Their complete identification is presented in Table 3.3.2.

To check the half-life of the isomeric transition we produced the time spectra for the two γ-transitions (313 and 694 keV). The results are shown in Fig. 3.32. Due to the relatively long half-life of the isomeric state (13.3(2) μs) compared to the observation time window (≈ 17 μs),

Table 3.3: *Most intense γ-lines observed in the energy spectrum with a gate on ^{67}Ni. The transitions coming from the decay of the isomer are in bold.*

E_γ [keV]	origin	E_γ [keV]	origin
175	^{66m}Co	885	^{70}Cu β-decay
184	^{67}Cu β-decay	901	^{70}Cu β-decay
190	^{69m}Cu	910	^{71}Zn β-decay
198	^{71m}Ge	964	^{65}Co β-decay
214	^{66m}Co	993	^{69}Cu β-decay
252	^{66m}Co	1007	^{69}Cu β-decay
313	**^{67m}Ni**	1040	^{70}Ge(n,n'γ)
386	^{71m}Zn β-decay	1077	^{68}Cu β-decay
470	^{69m}Cu	1116	^{65}Ni β-decay
486	^{69m}Cu	1180	^{69}Cu β-decay
511	annihilation	1251	^{70}Cu β-decay
531	^{69}Cu β-decay	1261	^{68}Cu β-decay
596	^{74}Ge (n,n'γ), ^{73}Ge (n,γ)	1273	^{65}Co β-decay
609	^{65}Ni β-decay	1294	^{68}Cu β-decay
620	^{71m}Zn β-decay	1424	^{66}Co β-decay
649	^{69}Cu β-decay	1429	^{69}Cu β-decay
680	^{69m}Cu	1460	^{40}K
694	**^{67m}Ni**	1482	^{65}Ni β-decay
814	^{68m}Ni	1710	^{69m}Cu
835	^{72}Ge(n,n'γ)	1870	^{69m}Cu
847	^{56}Fe(n,n'γ)		
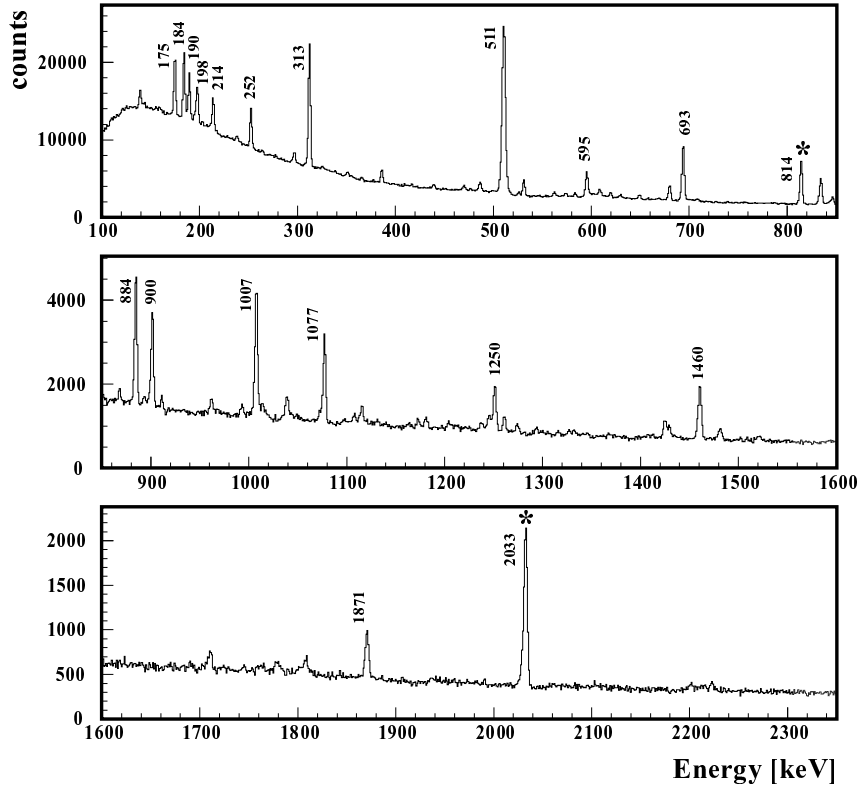
Figure 3.30: *Energy spectrum, gated on the implantation of ^{68}Ni ions, for the full time window. The γ-lines, originating from ^{68m}Ni are marked with asterisk.*

the fit of the half-life of the isomer was not so straightforward procedure. To make a reliable fit with a exponential function plus a constant background, it is necessary to apply some restrictions on the background. This we did using the energy spectra in the following way. We fitted the γ-line (313 keV) of the full-time-window energy spectrum, from where we obtained its net area. We integrated the total number of counts in the energy spectrum in the same energy window, which was used to produce the time spectrum for the particular γ-line. From these two numbers we derived the number of the background counts in the time-spectrum. The uncertainties of this estimation were the limits, within which we varied

Figure 3.31: *Energy spectrum for the γ-rays correlated to the arrival of ^{67}Ni ions. ∗ -transitions belong to the decay of the 9/2$^+$ isomer; ⋄- lines come from other isomers selected in the same settings of the spectrometer; ∇ - contamination lines from β-decay; the unmarked lines mostly come from (n, n'γ) reactions and from natural radioactivities.*

the background for the fit of the time spectrum. As a result we deduced

the half-life of the isomer $t_{1/2} = 13(1)$ μs, which is in good agreement
with the previously measured value $13.3(2)$ μs [Grz98]. To check the ve-
racity of the so obtained value, we applied the same method background
determination on shorter-lived isomers (e.g., ^{69m}Cu). This gave results,
consistent with the directly obtained background value from last part of
the time spectrum.
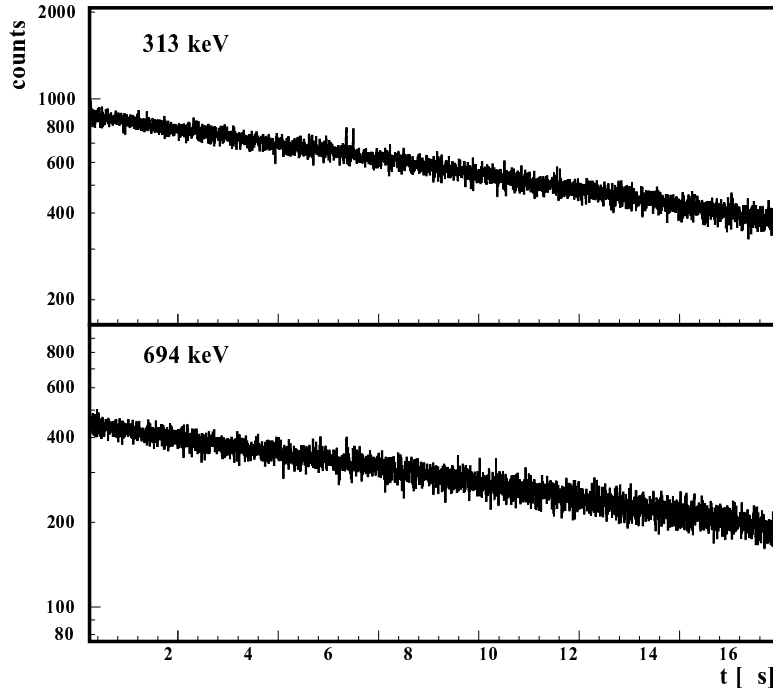
Figure 3.32: *Time spectra for the two γ-transitions in the decay of the*
$9/2^+$ isomer in ^{67}Ni.

Co isotopic chain

In our experiment we produced three different isotopes of Co (^{65}Co, ^{66}Co and ^{67}Co). However, we observed a γ-decaying isomer only in ^{66}Co.

The energy spectrum gated on the implantation of ^{66}Co ions is presented in Fig. 3.34. The peak at 175 keV originates from the short-lived isomer discovered by Grzywacz *et al.* [Grz98], while the other two peaks at 214 keV and 252 keV come from the long-lived isomer (100μs) observed in the same work. Due to the very long half-life of the longer-lived isomer, compared to the range of our time spectra ($\sim 17\mu$s), we cannot deduce its half-life from our experiment.
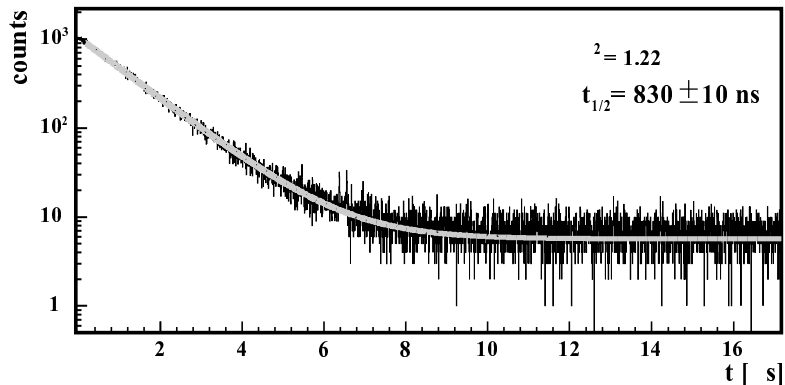
Figure 3.33: *Time spectrum for the 175 keV γ-line of ^{66}Co. The line is a result of a fit, using an exponential decay plus a constant background.*

The contaminating γ-lines, observed for the ^{66}Co case are the same as in the ^{67}Ni case. Therefore, we will not present their identification here but will refer to table 3.3.2.

A time spectrum for the 175 keV transition is presented in Fig. 3.33. From the fit we derived the half-life of the isomer $t_{1/2} = 830(10)$ ns. This is at variance with the value quoted by Grzywacz *et al.* 1.21 μs and the difference is a factor of $ln(2)$, which hints that the value reported in ref. [Grz98] is actually the life-time (τ) of the isomer.
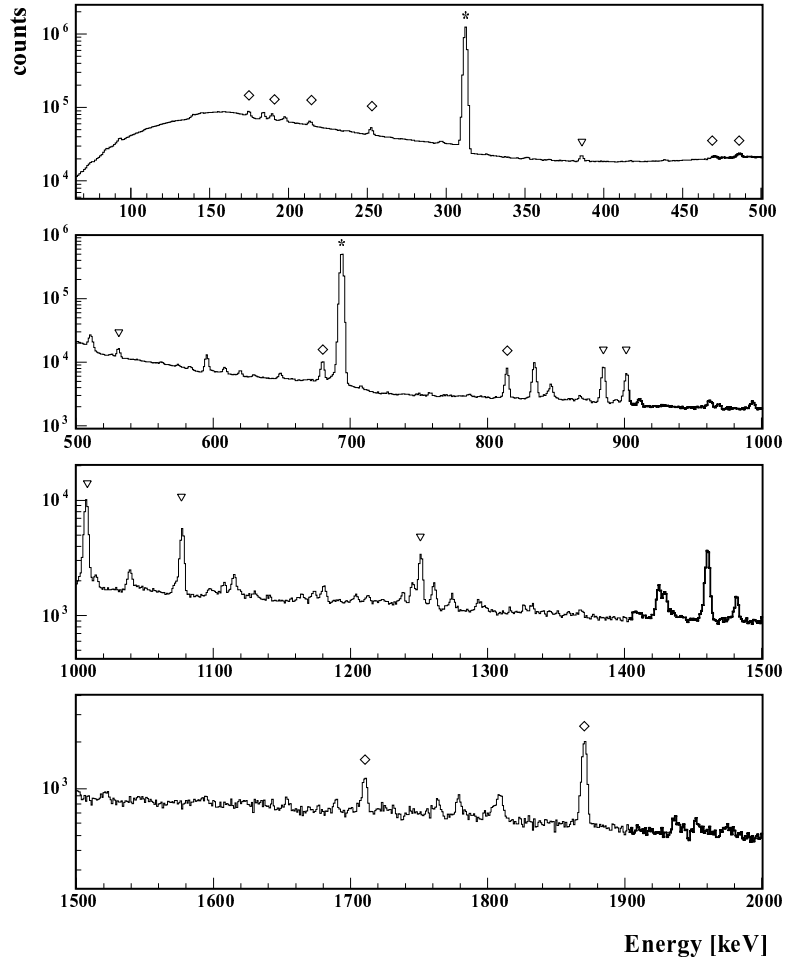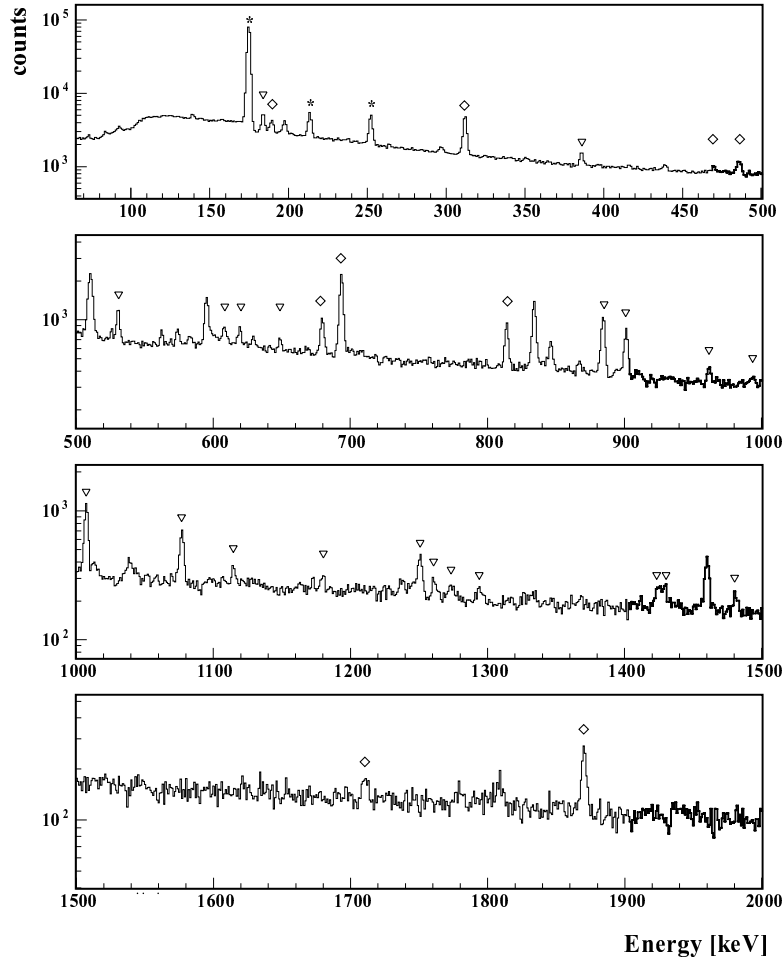
Figure 3.34: *Energy spectrum for the γ-rays correlated to the arrival of ^{66}Co ion. * -transitions belong to the decay of the isomers in ^{66}Co; $\diamond$- lines come from other isomers selected in the same settings of the spectrometer; ∇ - contamination lines from β-decay; the unmarked lines mostly come from $(n, n'\gamma)$ reactions and from natural radioactivies.*

Fe isotopic chain

In our experiment we produced $^{63-65}$Fe. We found isomeric γ-lines, correlated with the implantation of two of them, ^{65}Fe and ^{64}Fe.

The isomer in ^{65}Fe was discovered by Grzywacz *et al.* in projectile-fragmentation reactions. They observed a single γ transition of 364 keV and measured the half-life of the isomer ($t_{1/2} = 0.43(13)\mu$s). The energy spectrum of ^{65m}Fe, which we observed in our experiment, is shown in Fig. 3.35. The time spectrum, produced by a gate on the 364 keV transition is presented in Fig. 3.36.
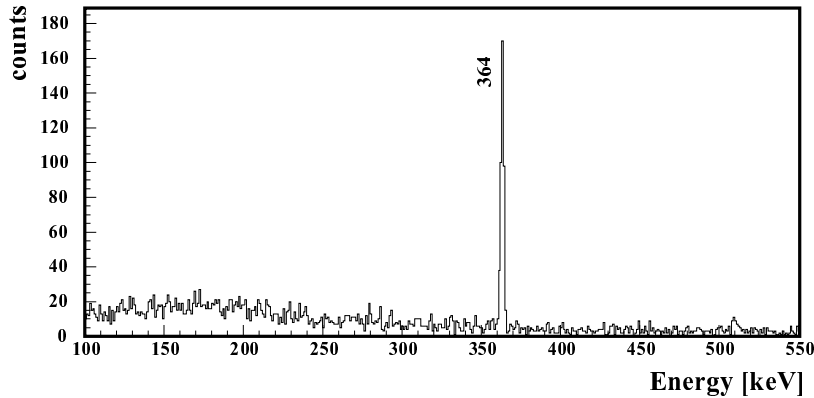
Figure 3.35: *Energy spectrum of ^{65}Fe for the first one μs time window. No other γ-lines, except the previously know 364 keV transition, were observed.*

With an exponential decay fit, we obtained the half-life of the isomer $t_{1/2} = 434(35)$ ns, which is in agreement with the previously reported value ($t_{1/2} = 430(130)$ ns [Grz98]) but is much more precise.

We found isomeric γ-transitions, correlated with the implantation of ^{64}Fe. At a first glance, this would mean a discovery of a new isomer. However, a more detailed overview on the region showed that an isomer with the same transitions and half-life was already discovered in ^{61}Fe. A check with the LISE program showed, that indeed on the energy-loss *vs.* time-of-flight plot the spots, produced by the fully stripped ions of ^{64}Fe and the first charge state (25+) of ^{61}Fe would overlap. So the isomeric transitions, which we found are actually originating from ^{61m}Fe. Thus, one have to conclude that, when looking for new isomers, one has to be careful with the different charge states of the heavy ions. This is usually done by using a full-energy detector, which can discriminate between the different charge states. However, in a *g* factor measurement, this is not such a serious issue. If one implants a different charge state, as
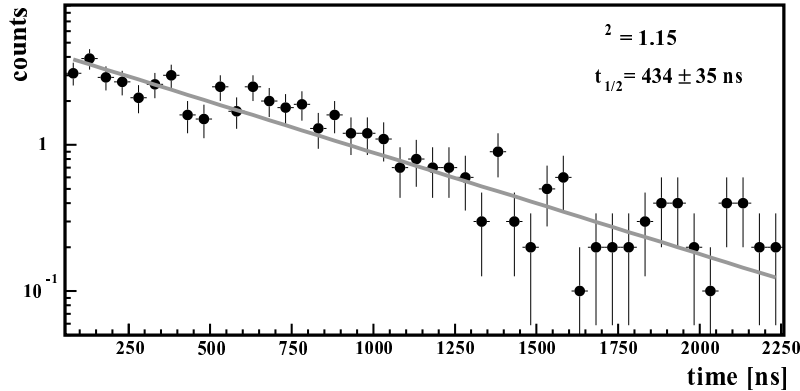
Figure 3.36: *Time spectrum for the 364 keV γ-line of ^{65}Fe. The line is a result of a fit, using an exponential decay.*

well as fully stripped nuclei, the fully stripped nuclei and other charge states of the same isotope will have different positions on the energy-loss *vs.* time-of-flight plot. Thus, even if the orientation of the non fully stripped ensemble of nuclei is completely destroyed by the interaction of the electron and the nuclear spins [Gol82, Vyv00], they will not influence the amplitude of our signal. However, an identification of a new isomeric state should be done very carefully.

The energy spectrum of ^{61m}Fe is shown in Fig. 3.37. No other lines, except for the previously known 207 keV and 654 keV transitions, were observed. The half-life of the isomer (see Fig. 3.38) which we observed ($t_{1/2} = 226(25)$ ns) is in agreement with the previously measured value ($t_{1/2} = 250(10)$ ns [Grz98]).

Mn isotopic chain

In our experiment we observed two Mn isotopes, ^{62}Mn and ^{63}Mn. Isomeric γ-rays were found only in correlation with ^{62}Mn. This isomer was previously identified [Lew99] and a single γ-ray of 113 keV was found.

The energy spectrum, gated on the implantation of ^{62}Mn, is shown in Fig. 3.39. We also found only one γ-ray and its time spectrum is shown in Fig. 3.40. From a fit with an exponential decay, we derived the half-life of the isomer $t_{1/2} = 90(4)$ ns, which is in agreement with the previously measured value $t_{1/2} = 95(2)$ ns [Lew99].
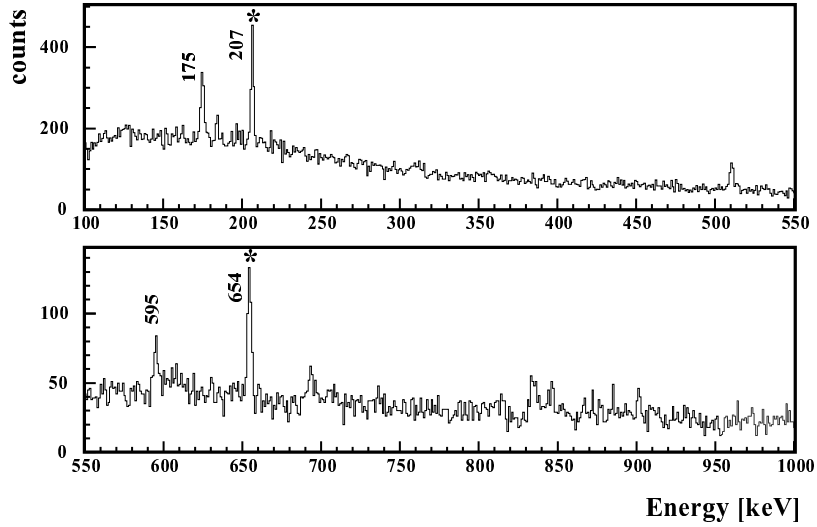
Figure 3.37: *Energy spectrum of ^{61m}Fe for the first one μs after the implantation. The two γ-lines (207 keV and 654 keV), originating from the isomer are marked with asterisk.*
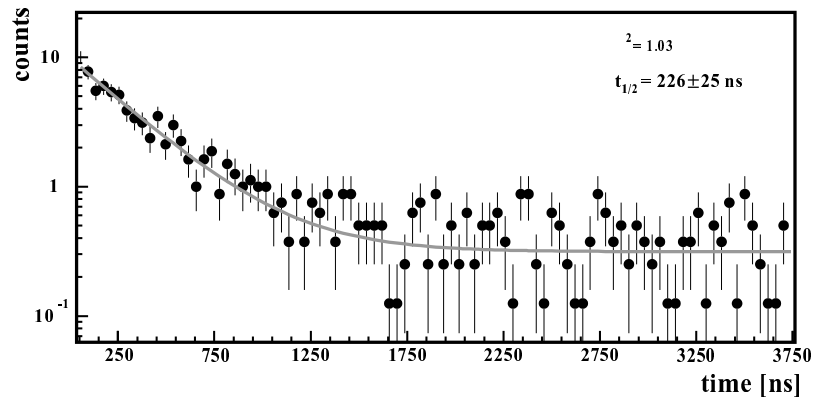
Figure 3.38: *Time spectrum, gated on the 207 keV and 654 keV transitions. For the fit we used an exponential decay plus a constant background.*
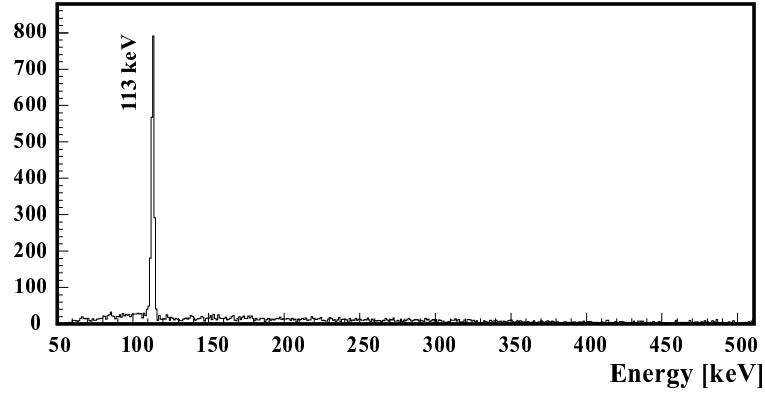
Figure 3.39: *Energy spectrum of ^{62m}Mn for the first one μs after the implantation.*
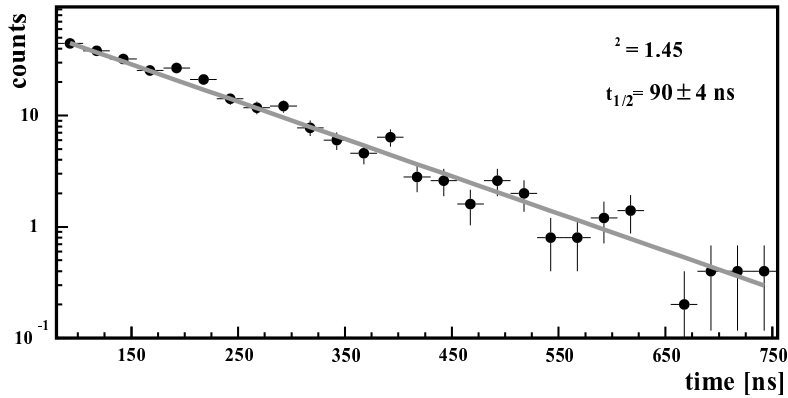
Figure 3.40: *Time spectrum, gated on the 113 keV transition. For the fit we used an exponential decay.*

With this we would like to conclude the analysis of the energy and time-spectra for the different nuclides, observed in our experiment. In the following sections we will continue with the TDPAD analysis of the three isomers in ^{69}Cu, ^{67}Ni and ^{66}Co, whose g factors we measured.

3.3.3   TDPAD analysis of the 13/2$^+$ isomer in ^{69}Cu.

The next step of the TDPAD analysis is to construct the $R(t)$ function, described in Chapter 1 (see eqn. 1.49). At this point, we had two different approaches which we will now describe briefly.

We will call the first approach "PAW analysis", coming from the name of the analyzing programme used [PAW]. In the PAW analysis, we produced time spectra for each of the crystals of the Ge detectors, imposing a gate on the energy of the events. Such time spectra were produced for each of the isomeric γ-transitions. The advantage of this method is that we can work with the full time resolution of the spectra.

We will name the second approach "FITEK analysis", based on the program used to fit photopeak intensities in γ-energy spectra [Sto84]. In this approach, we first produced time bins, with a width consistent with the half-life of the isomer under investigation. We created energy spectra for each of the time bins. Afterwards, the intensities of the isomeric γ-lines in the energy spectra were determined by a Lorentzian-fit of the peaks. In this way, the background γ-radiation could be subtracted, which is not possible in the PAW analysis.

Let us now consider some peculiarities of the PAW analysis. The $R(t)$ function was derived in Chapter 1 with the assumptions that both detectors have the same efficiency and that there is no background contributing to the spectra. Unfortunately, these assumptions are not always valid in an experimental work and we had to correct for this. We can distinguish two different ways of doing this. In the first, simple case, we assume that the background in each of the time spectra is taken to be proportional to the efficiency of the detector. After correcting for the relative efficiency of the two detectors, we will obtain the same level of background for the time spectra. Constructing the $R(t)$ function by simply taking the difference divided by the sum of the two time spectra should then represent a proper treatment of the data.

In the second, more realistic case, the ratio between the background in the two time spectra is not proportional to the relative efficiency of the detectors. In that case, if we apply the procedure described above, we will end up with a picture similar to the one shown in Fig. 3.41. There we see that during the first few μs in which the isomer is still decaying, the base-line is around zero. After the complete decay of the isomer, the different background in the two time spectra causes a drift of the base-line away from zero.

To correct for this effect, one first has to subtract the background
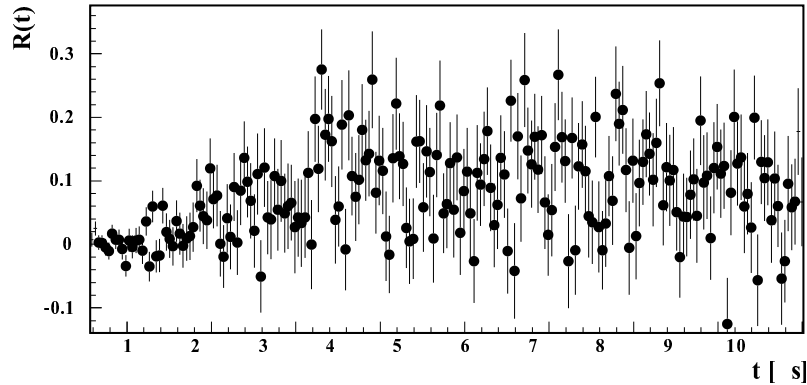
Figure 3.41: *R(t) function for the 486 keV transition in ^{69}Cu obtained without initial corrections for the background.*

component for each of the time spectra and correct only afterwards for the different efficiency of the two detectors.

Another way to correct for such an effect is by inverting the direction of the magnetic field and using only one detector to produce the $R(t)$ function. However, in such a situation one has to take care for possibly different detector response depending on the magnetic field. It is also possible to make such a correction only during the experiment and two times more measuring time is necessary to obtain the same statistics.

We applied the PAW analysis to each of the isomeric transitions in ^{69}Cu. A clear oscillation pattern was observed in three of them - 190 keV, 471 keV, and 680 keV (see Fig. 3.12 on page 68). The resulting $R(t)$ functions are shown in Fig. 3.42. Note that the amplitude of the oscillations in the 190 keV transition has opposite sign compared to those in the 471 keV and 680 keV transitions. This is in very good agreement with the spin/parity assignments of the connected levels in these transitions and with their assumed multipolarities ($E2$ for 190 keV, $M1$ for 471 keV and $E1$ for 680 keV).

A normal question which one can put at this point is why do we observe oscillation patterns only in three of the transitions. Any of the remaining γ-lines (with the exception of the 486 keV line), originating from the $13/2^+$ isomer, have poorer statistics than the three mentioned above. Thus the non-observation of wiggles in them can be attributed to
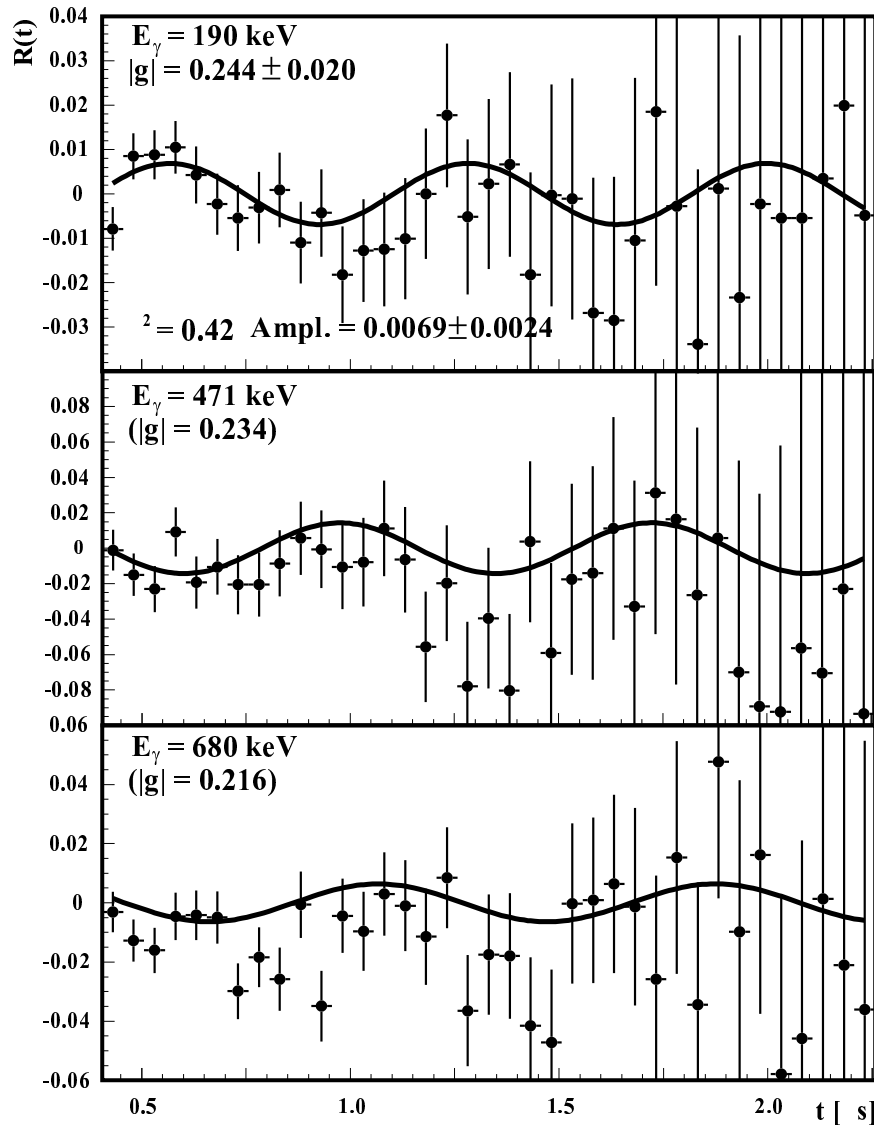
Figure 3.42: *R(t) function for the 190 keV, 471 keV, and 680 keV transitions in ^{69}Cu, obtained using the PAW analysis.*

lack of statistics. However, the 486 keV line has very similar intensity to the 471 keV line. Yet, we do not observe a clear oscillation pattern there. The reason for this can be looked for in the amplitude of the radiation parameter of the transition. Ishii *et al.* [Ish00], as well as Broda *et al.* [Bro98], assign the structure to which this transition belongs as a collective band. In such a case we can derive the mixing ratio δ for the $M1/E2$ transition, using the strong-coupling limit [Boh75]:

$$\frac{\delta^2}{1+\delta^2} = \frac{2K^2(2J-1)}{(J+1)(J-1+K)(J-1-K)} \times \frac{E^5_{\gamma\ \Delta J=1}}{E^5_{\gamma\ \Delta J=2}} \times \lambda \qquad (3.2)$$

where K is the projection of the nuclear spin on the symmetry axis of the nucleus; J is the initial spin of the transition; and $\lambda = \frac{I_\gamma(J \to J-2)}{I_\gamma(J \to J-1)}$ is the ratio of the intensities of the two transitions and $E_{\gamma\ \Delta J=1}$ and $E_{\gamma\ \Delta J=2}$ are, respectively, the energies of the two transitions (in MeV). In our case we can assume that $K = 7/2$ (the spin of the band head), $J = 11/2$, $E_{\gamma\ \Delta J=1} = 486$ keV, $E_{\gamma\ \Delta J=2} = 957$ keV and $\lambda = 6/68 = 0.088$ (see Fig. 3.12, the ratio of the amplitudes which we observed in our experiment was very similar). After substituting all of the above values in formula 3.2 we obtain $|\delta| = 0.11$, with which we can calculate the radiation parameter A_2 for the transition (using formula 1.28). Finally we obtain $A_2(486keV) = 0.083$, which is four times smaller than the radiation parameter for the 471 keV transition $A_2(471keV) = 0.303$. This explains why no oscillation pattern was observed in the $R(t)$ function for the 486 keV transition.

Trying to reduce the influence of the background on the $R(t)$ function, we applied the FITEK analysis. For the ^{69}Cu case, each of the created time bins had a width of 25 ns. The results of this analysis are shown in Fig. 3.43. All curves depicted in Fig. 3.42 and 3.43 are produced by a χ^2 method using the formula 1.50. In this expression, both the frequency and the phase of the oscillations depend on the isomeric g factor. However, due to the specific position of the Ge Clover detectors in our experiment (see Fig. 3.16), we are not sensitive to the sign of the measured g factor (see section 1.4.1).

A more detailed examination of the results of the two methods of analysis, shows that the PAW analysis gives slightly higher values for the g factor. In general one can expect that the FITEK analysis would give more confident value since the influence of the background on it has been removed. However we do not have any reasons to reject completely the PAW analysis. Therefore, to derive the final value for the g factor
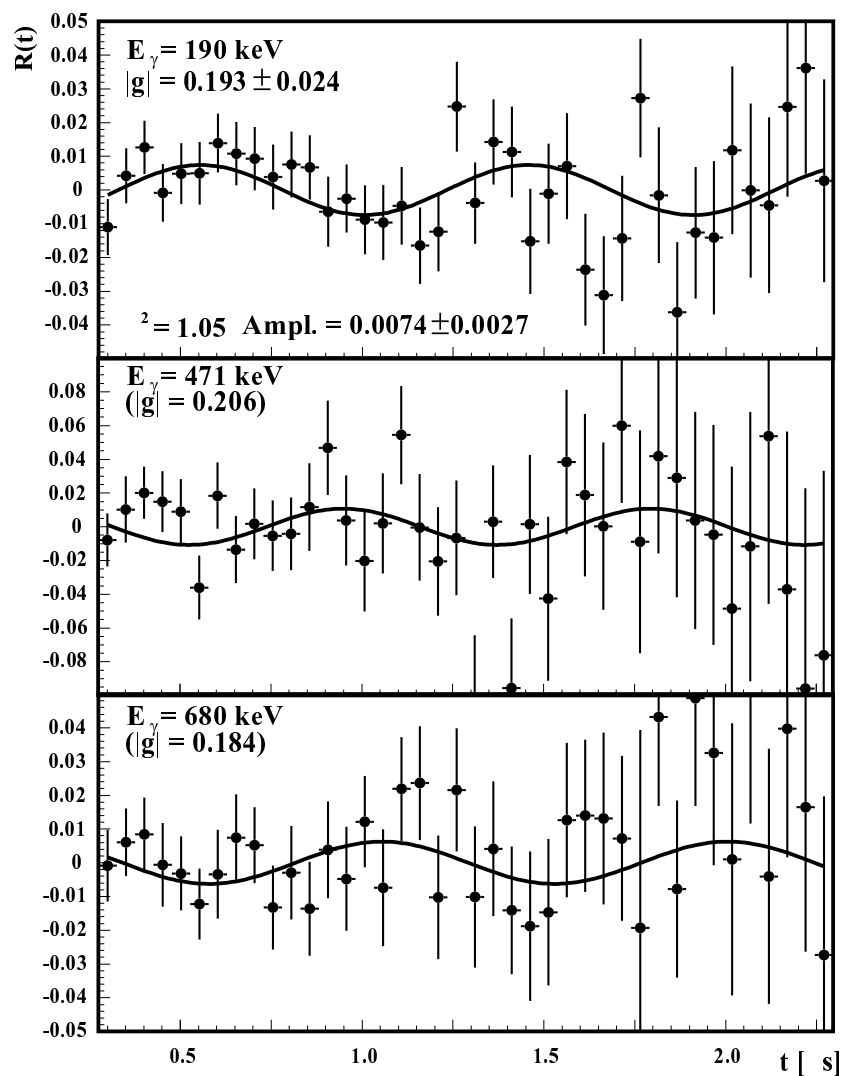
Figure 3.43: *R(t) function for the 190 keV, 471 keV, and 680 keV transitions in ^{69}Cu obtained by the FITEK analysis.*

of the ^{69}Cu isomeric state, we will take the average value of the two types of analysis for the 190 keV line. The other two transition (471 keV and 680 keV) only confirm the results from the 190 keV fit but due to their poorer statistics they should not influence the final result. Thus, we can conclude that the $13/2^+$ isomeric state in ^{69}Cu has a g factor of $|g| = 0.219 \pm 0.022_{stat.} \pm 0.025_{syst.}$ where the systematic error accounts for the difference in the two methods of analysis and the statistical uncertainty comes from the average of the fit results (the double usage of the same data is properly taken into account). The uncertainty of the magnetic field and the corrections for the Knight-shift and paramagnetic corrections [Haa] are negligible compared to the quoted errors.

3.3.4   TDPAD analysis of the $9/2^+$ isomer in ^{67}Ni.

In the TDPAD analysis of the $9/2^+$ isomer in ^{67}Ni (see Fig. 3.7) we can construct the $R(t)$ function for the two isomeric transitions, the 313 keV and the 694 keV. Here we also applied the two methods of analysis, described before, ad the results are presented in this section.

The result from the PAW analysis for the 313 keV transition shows the pattern presented in Fig. 3.44 a).

The constructed $R(t)$ function for the 694 keV line does not show evidence for an oscillation pattern (Fig. 3.44 b)). This is at variance with the expectations for pure $M2$ (313 keV) and $E2$ (694 keV) transitions. One can explain the lack of a clear pattern in the 694 keV line invoking two reasons: i) due to the very small amplitude of the oscillations and the poorer statistics of the higher energy transition, we cannot distinguish the oscillation pattern; ii) one can speculate about a possible $M2/E3$ mixing in the 313 keV transition. A mixing amplitude of $\delta = 0.2$ would lead to a difference in the expected amplitudes of the oscillations for the two transitions of about $3 : 2$.

The time bins which we created for the FITEK analysis of ^{67}Ni were 75 ns each. The result is shown in Fig. 3.45.

Similarly to the ^{69m}Cu analysis, here we again find that the PAW analysis gives a slightly higher value for the g factor. However, the difference for the ^{67m}Ni case, is not significant.

As one can observe from the figures (3.44 and 3.45), in both analyses we use only the first few μs of the full time window. As the period of the Larmor precession is much shorter than the half-life of the isomer, it is possible to fold back the information of the full 17 μs window into
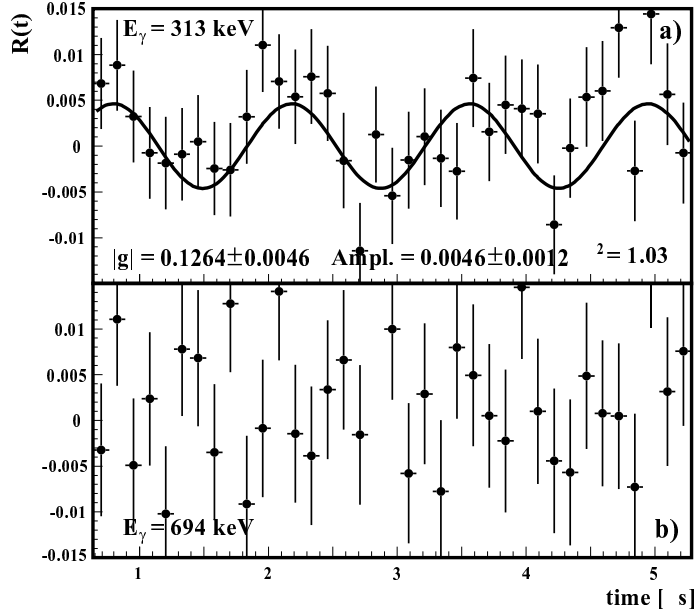
Figure 3.44: *R(t) function, obtained for the 313 keV and 694 keV transitions in ^{67}Ni using the PAW analysis method.*

the first ~ 5 μs using an autocorrelation function. This method is well known and widely used, especially in signal processing (see, e.g., [Lan67] or [Ben66]). Here, we will discuss only some of its main characteristics.

The autocorrelation function of a data set, finds a correlation between the data at the moment t and the values at the moment $t + \tau$. In integral expression it has the form:

$$X(\tau) = \lim_{T \to \infty} \frac{1}{T} \int_0^T f(t)f(t + \tau)dt \qquad (3.3)$$

The quantity $X(\tau)$ is a real function with a maximum at $\tau = 0$. If the data, treated by the autocorrelation function, represent a harmonic function, then the autocorrelation function will have the same period as the harmonic function. Using the autocorrelation procedure one loses the phase information. Thus, for any phase of the harmonic fluctuations the autocorrelation function will be a cosine function. In the overall case,
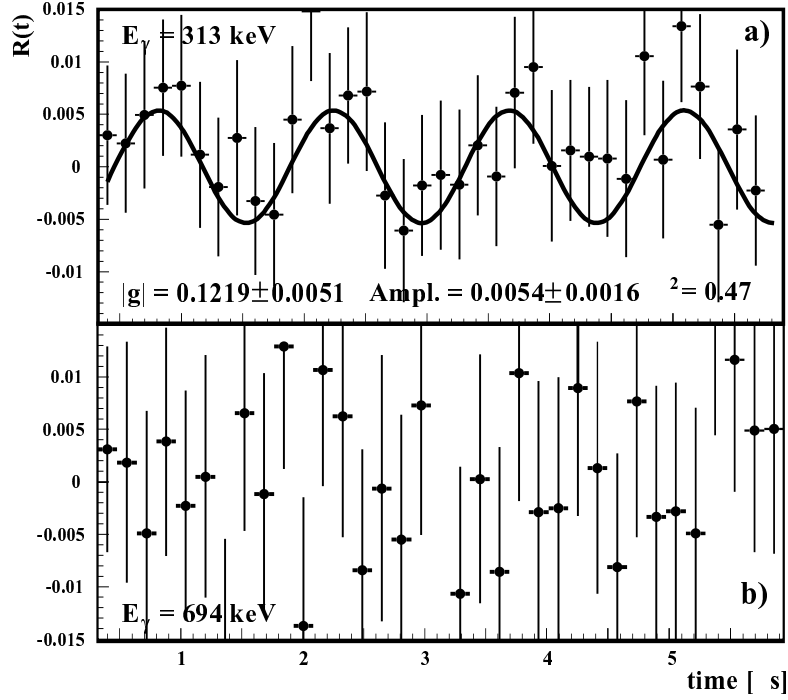
Figure 3.45: $R(t)$ function for the 313 keV and 694 keV transitions in ^{67}Ni obtained by the FITEK analysis.

the amplitude of $X(\tau)$ does not coincide in any way with the amplitude of the harmonic function $f(t)$.

Since in our case we are going to deal with discrete data points it is more convenient to transform the autocorrelation function from an integral to a discrete expression and also to normalize it:

$$X(n) = \sum_{k=k_1}^{k_2-n} \frac{f(k)f(k+n)}{k_2 - k_1 - n} \Big/ \sum_{k=k_1}^{k_2} \frac{f^2(k)}{k_2 - k_1} \qquad (3.4)$$

After the normalization, in the ideal case of treating a strictly harmonic function without any noise components, one should obtain a pure cosine function with an amplitude of 1, independently on the amplitude of the original function.

It is also a general rule that the maximum value of n, in which the function is presented, should be much smaller than the full observation window $(k_2 - k_1)$.

Applying the autocorrelation analysis to the 313 keV data, we obtained the wiggles shown in Fig. 3.46 a). The application of the same technique to the 694 keV transition (see Fig.3.46 b)) did not give any clear result.
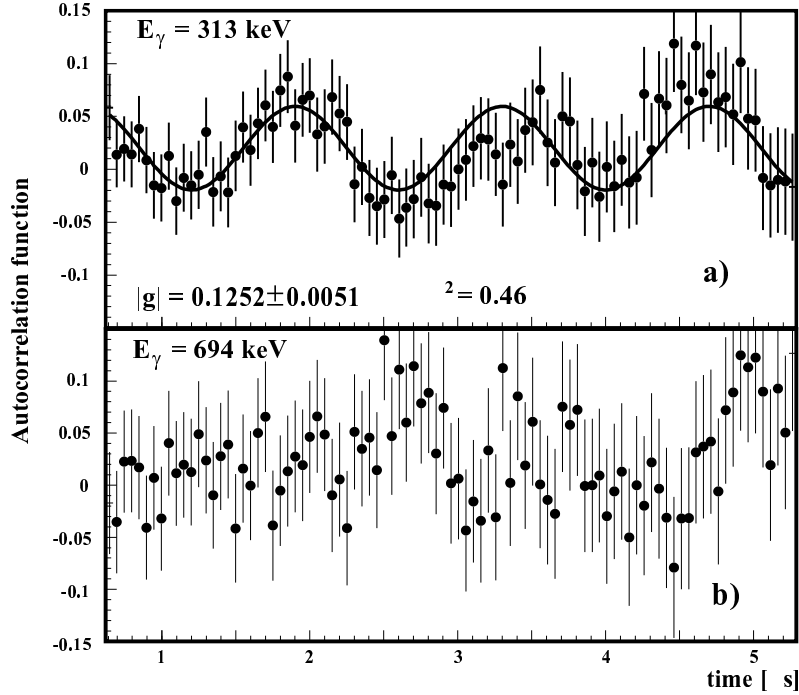
Figure 3.46: *Autocorrelation function of the 313 keV (a) and the 694 keV (b) transitions in ^{67}Ni, applied to the PAW data.*

By using this technique we observe a much clearer pattern. The amplitude of the oscillations is increased by a factor of ~ 10 and the statistics is also improved by using a broader time window. However, as it was mentioned before, the amplitude of the autocorrelation function does not correspond to the real amplitude of the Larmor precession. We also lost any phase information contained in the initial $R(t)$ function.

As a result of the three different methods of analysis, we could derive the mean value for the g factor of the isomeric state $|g(^{67}\text{Ni},9/2^+)|$ = 0.1245 $\pm 0.0049_{stat.} \pm 0.0035_{syst.}$. In the quoted statistical error is included the uncertainty obtained from the fit of the three methods of analysis (PAW, FITEK and autocorrelation) and the usage of the same data three times is taken into account. In the systematic error is included the difference between the PAW and the FITEK analysis and also the uncertainty of the magnetic field. Its inhomogeneity over the implantation spot is negligible. The Knight-shift and paramagnetic corrections are negligible, compared to the mentioned uncertainties.

3.3.5 TDPAD analysis of the isomer in ^{66}Co

There is only one isomeric transition (175 keV) in the short-lived isomer of ^{66}Co. The results from the PAW analysis, depicted in Fig. 3.47, show a clear oscillation pattern.
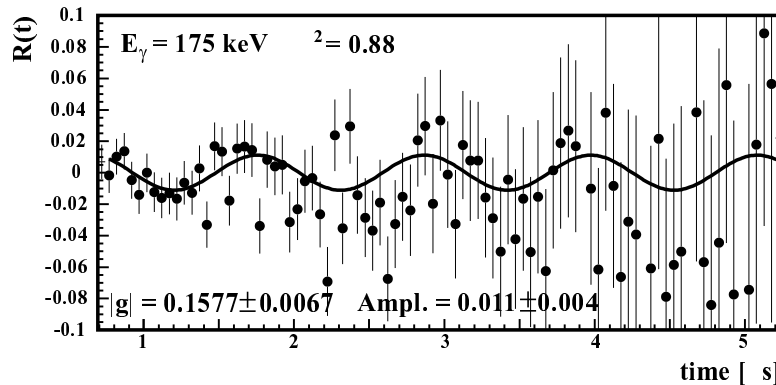
Figure 3.47: *Oscillation pattern for the 175 keV γ-line of ^{66}Co (PAW analysis).*

For the FITEK analysis of ^{66}Co, we created time bins of width 50 ns each. The observed wiggles are shown in Fig. 3.48. The g factor which we obtained as an average of the two methods, is $|g|$ = 0.157 $\pm$ 0.009. The quoted error includes the statistical error of the χ^2 fit (the usage of the same date twice is properly taken into account), as well as the 2% uncertainty of the magnetic field. The Knight-shift and the paramagnetic corrections are expected to be smaller than the mentioned uncertainties.
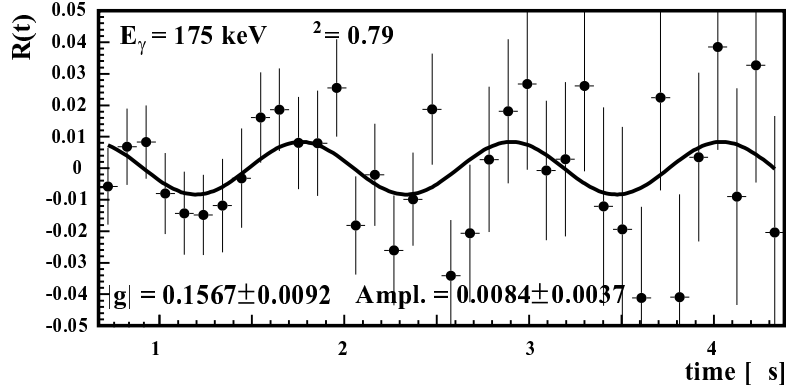
Figure 3.48: *Oscillation pattern for the 175 keV γ-line of ^{66}Co (FITEK analysis).*

3.3.6   Points to improve in follow up experiments

After discussing the results of the data analysis we would like to mention a few points, which should improve in future experiments of this type.

The usage of BaF$_2$ detectors

The BaF$_2$ detectors have a very good time resolution ($\Delta t \leq 1$ ns) and, from this point of view, they are superior to the Ge detectors ($\Delta t \geq 10$ ns). Their energy resolution, however, they have much worse characteristics (see Fig. 3.49). In our experiment, we positioned three detectors at $\pm 45^o$ and at -135°. However, we could not derive any valuable results from them. This was mainly attributed to their bad energy resolution combined with the relatively complex character of the decay schemes of some of the isomers. Also the rather high background of the energy spectra played an important role by decreasing the peak-to-background ratio, so that a significant amount of random events was introduced into the time spectra.

Another important issue is the different energy resolution of each pair of the BaF$_2$ detectors which have to be combined to obtain the $R(t)$ function. This plays an important role, especially in the analysis of long-lived states (like the case of ^{67}Ni) for which one does not observe in a time window, consisting of a pure background. This complicates enormously the background correction.
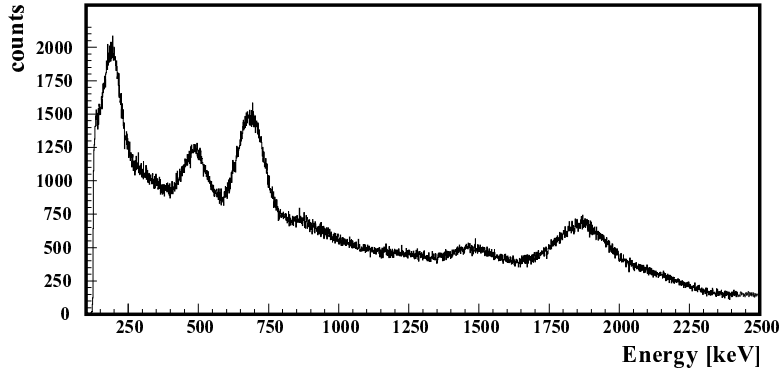
Figure 3.49: *Energy spectrum of one of the BaF_2 detectors gated on the implantation of ^{69}Cu ions. Note that the 471 keV and 486 keV as well as the 1710 keV and 1871 keV lines are not resolved.*

The influence of different factors on the amplitude of the observed oscillations

A major point, concerning the feasibility of TDPAD measurements on nuclei produced in projectile-fragmentation reactions, is the amplitude of the observed oscillations. This amplitude depends on the amount of orientation initially produced in the reaction mechanism itself and on all factors which decrease the actually produced alignment. The first observation of spin alignment of isomeric states in projectile-fragmentation reactions was reported by Schmidt-Ott *et al.* [SO94] for ^{43m}Sc fragments produced after the fragmentation of a 500 MeV/u ^{46}Ti beam. At intermediate energies, prior to the current work, alignment has only been reported for light nuclei in their ground state [Asa91, Ney97a].

To discuss this issue in more detail, it will be convenient to rewrite formula 1.50 in the form (here we have neglected the $k = 4$ component):

$$R(t, \theta, B) = \frac{3fA_2B_2U_2Q_2}{4 + fA_2B_2U_2Q_2}cos[2(\theta - \omega_L t - \alpha)] \qquad (3.5)$$

Here, A_2 is the angular distribution coefficient, which depends on the spin/parities of the nuclear states connected by the observed γ-radiation (see eqn. 1.28); B_2 is the orientation parameter, which depends on the reaction mechanism; U_2 is the deorientation coefficient (see eqn. 1.31);

Q_2 is the geometrical factor; f is the fraction of aligned nuclei, which retain their orientation until the isomeric decay.

The angular distribution coefficient A_2 of a γ-transition can be calculated (formula 1.28), if the spin and multipolarity (also the mixing ratio in case of a mixed transition) of the γ-ray are known.

The orientation parameter B_2 can be calculated theoretically in the participant-spectator model (see Chapter 1). It is related to the spin-alignment A via the following expression (see, e.g., [Cou01]):

$$B_2 = \frac{\sqrt{5}|\alpha_2(max)|}{\sqrt{I(I+1)(2I+3)(2I-1)}}A \qquad (3.6)$$

where $\alpha_2(m) = I(I+1) - 3m^2$ is defined in a way, that $-1 \leq A \leq 1$. For maximum oblate alignment ($A < 0$), all nuclei are in the lowest m state ($m = 0$ or $\pm 1/2$) and for maximum prolate alignment ($A > 0$) all nuclei are in the highest m state ($m = I$).

To be able to compare the theoretically calculated alignment to the experimentally observed one, we will have to estimate the geometrical correction factor Q_2 and the f-factor for our experiment.

The geometrical correction factor (Q_2 from eqn. 3.5) for a circular detector of radius r at a distance h from the source is given by the approximate formula [Sie65]:

$$\begin{aligned} Q_2^d &= \frac{1}{2}cos\alpha(1 + cos\alpha), \qquad (3.7) \\ \alpha &= tan^{-1}(r/h) \end{aligned}$$

Accepting the approximation that the Ge CLOVER detectors are circular with radius 46 mm and considering a distance between the detectors and the implantation spot $h \sim 9$ cm, we obtained the correction factor for each of the detectors to be $Q_2^d = 0.84$. The final geometrical factor is actually the product of the correction factors for the two detectors, $Q_2 = 0.71$.

Since the Ge CLOVER detectors [She99] do not have a circular shape and also the implantation spot, which is our source in this case, had a size of approximately 1.5×1.5 cm we performed GEANT simulations [GEA] for the realistic case. The results for the dependence of the geometrical factor on the distance between the detectors and the implantation point are presented in Fig. 3.50. The total realistic geometrical factor, estimated for the particular setup conditions, is $Q_2 = 0.82(3)$.
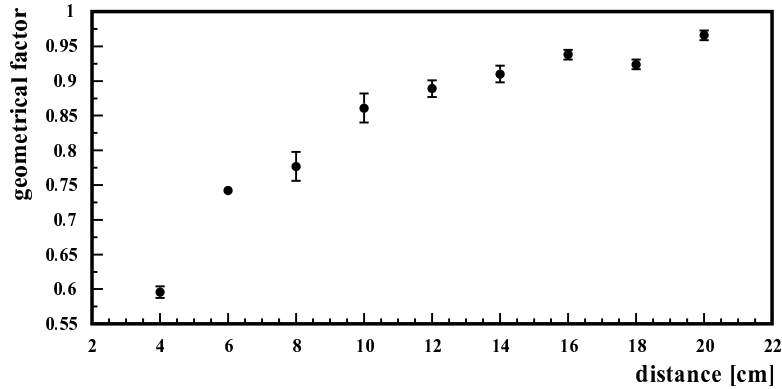
Figure 3.50: *Results of the GEANT simulations for the dependence of the total geometrical factor on the distance between the implantation spot and the GE CLOVER detectors.*

Another factor which can have a significant influence on the observed alignment is the electron pick up of the heavy ions before their implantation. This should be related to the f coefficient in formula (3.5). The electron pick up of the heavy ions can occur during their passage through the silicon ΔE detector. The pick-up of electrons in the Al-degrader is neglected because the Al-degrader was clamped on the Cu foil. The coupling of the electron and the nuclear spins and their interaction with external magnetic fields can significantly decrease or even completely destroy the orientation of the nuclear ensemble [Gol82, Vyv00].

We estimated the probability for electron pick up of the @40 MeV/u fragments during their passage through the 300 μm Si detector with the LISE [Baz01] and ETACHA [Roz96] programs. The calculations of the charge distribution in the LISE program are based on the work of Leon *et al.* [Leo98] in which a semi-empirical formula is derived and adjusted to experimental data in the following limits: atomic number of the projectile $36 \leq Z_p \leq 92$ in the energy range 18 MeV/u $\leq E \leq 44$ MeV/u.

The ETACHA program calculates the charge state distribution of ions with up to 28 electrons, distributed over $n = 1, 2$ and 3 subshells. Its model is based on an independent electron model taking into account electron loss, capture and excitation from and to all subshells. The calculations are usually performed by solving a set of differential ("rate")

equations.

The results from the two different approaches, a semi-empirical one and a model calculation, clearly show that the electron pick up issue is a serious problem in this region of fragment energies (see Table 3.3.6). In the higher energy region, like the case reported by Schmidt-Ott *et al.* [SO94], the situation is quite different. Schmidt-Ott *et al.* observed a decrease of 20% of the alignment for a fragment energy of about 50 MeV/u and a full conservation of the spin orientation at higher energies (80 - 90 MeV/u). The calculation performed by the LISE program for these cases showed a 20% probability for one electron pick up at 50 MeV/u and only fully stripped nuclei at the higher energies. The ETACHA calculations showed no electron pick up at any of the cases of the Schmidt-Ott *et al.* experiment. Assuming, that all isomers which are not fully stripped are randomly oriented at the moment of implantation, we deduce from Table 3.3.6 that we had a reduction of the reaction-created orientation due to electron pick up by a factor of 1.5 to 3.5, the higher values being more probable.

Table 3.4: *Results from the LISE and ETACHA calculations for the percentage of fully stripped, 1 electron pick up and pick up of more electrons during the passage of the 300 µm silicon detector.*

ion	energy	LISE			ETACHA		
	[MeV/u]	fully str.	1 e$^-$	> 1 e$^-$	fully str.	1 e$^-$	> 1 e$^-$
^{66}Co	39.7	31 %	42 %	27 %	64 %	31 %	5 %
^{67}Ni	41.4	30 %	42 %	28 %	64 %	32 %	4 %
^{69}Cu	41.9	27 %	43 %	30 %	58 %	35 %	7 %

From these results, we can conclude that the electron pick up of the heavy ions passing through the silicon ΔE detector is a serious issue and one has to find a way to deal with it. One of the manners to deal with this problem is by increasing the velocity of the fragments. This can be done either by increasing the energy of the primary beam or by selecting a projectile nucleus close to the primary beam nucleus.

Coming to the end of this point, we can say that the experimentally observed alignment in our case is decreased by a factor of $\sim$ 5 compared to the reaction-generated one. Using this correction factor and the amplitude of the oscillations, which we observed in our experiment, we can derive the reaction-created alignment for ^{66}Co, ^{67}Ni and ^{69}Cu

and compare it to the model predictions.

According to the participant spectator model [Asa91] (described in more details in Chapter 1), we should expect a positive alignment in the center of the momentum distribution (see Fig.1.7) which goes through zero in the middle wing of the momentum distribution to negative values in the far wing of the momentum distribution. Thus for our case of momentum selection (see Fig. 3.15) we should observe a positive alignment for ^{66}Co and negative values for ^{69}Cu and ^{67}Ni.
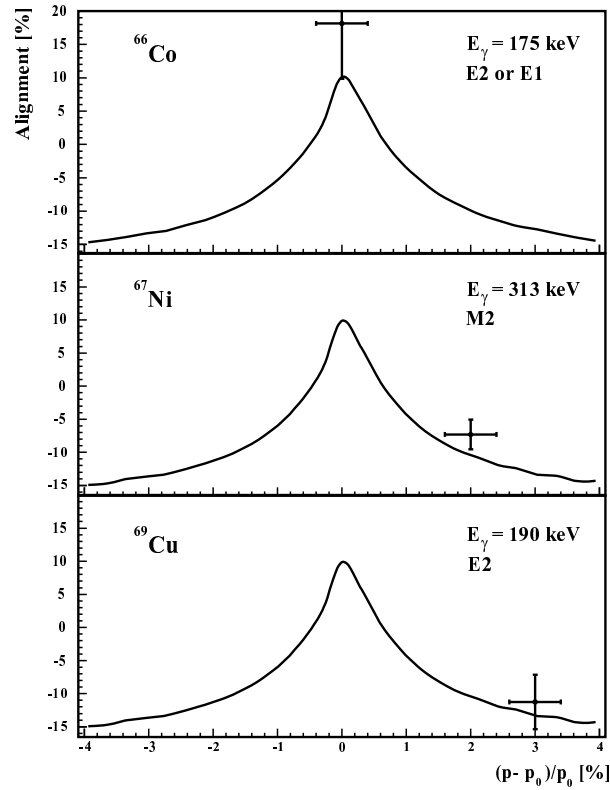
Figure 3.51: *Results from the simulations for the reaction-created alignment, compared with the corrected experimentally observed values. The sign of the experimental alignment is assumed in accordance to the simulations.*

The simulations for the reaction-created alignment [Dau] showed the

results presented in Fig. 3.51. The curves represent the results of the simulations using the kinematical fragmentation model [Asa91, Oku94, Dau01], rescaled with a factor of 1/2. The experimental points for ^{66}Co, ^{67}Ni and ^{69}Cu are derived from the amplitudes of the observed oscillation patterns for the 175 keV, 313 keV and 190 keV transitions and corrected by a factor of 5 as derived before. Thus the model predicts 2 times higher alignment than what we observed in our experiment.

3.4   Interpretation of the results

In this part, we will try to find out how the obtained results fit into our understanding of the nuclear structure in the ^{68}Ni region. Before discussing the three obtained g factors separately, we would like to systematize the g factors for the different single-particle orbits, which we are going to use here. They are presented in Table 3.5

Table 3.5: *Table of the different g factors, which we use in our calculations. The effective g factors are $g_l^{eff.} = g_l^{free}$ and $g_s^{eff.} = 0.7 g_s^{free}$. The empirical values are from Ref. [Rag89, Mul89]. The last two columns are the orbital and the spin parts of the empirical g factors. They are derived by the empirical values of the spin-orbit partners.*

single-particle orbit	free	eff.	emp.	$g_l^{emp.}$	$g_s^{emp.}$
$\pi f_{5/2}$	0.345	0.584	0.669	1.0235	3.505
$\pi f_{7/2}$	1.655	1.412	1.378	1.0235	3.505
$\nu p_{3/2}$	-1.275	-0.893	-0.50	0.330	-2.16
$\nu p_{1/2}$	1.275	0.893	1.16	0.330	-2.16
$\nu f_{5/2}$	0.547	0.383	0.301	-0.0465	-2.479
$\nu g_{9/2}$	-0.425	-0.298	-0.269	0.10	-3.230

3.4.1 ^{69}Cu case

Our first attempt to evaluate the obtained g factor for the $13/2^+$ isomer in ^{69}Cu ($|g| = 0.219(33)\ \mu_N$) is by comparing it to the g factor, calculated in the weak-coupling approach. We have calculated the g factors of two possible pure configurations, using the additivity relation eqn. 1.16, using the free, effective and empirical g factors as shown in Table 3.5. The results from these calculations are presented in Table 3.6.

Table 3.6: *Calculated 13/2⁺ g factors for three different values of the single particle g factors.*

	free	eff.	emp.
$g(\pi p_{3/2}\nu p_{1/2}g_{9/2})_{13/2^+}$	+ 0.387	+ 0.317	+ 0.244
$g(\pi p_{3/2}\nu(f_{5/2}g_{9/2})_{5^-})_{13/2^+}$	+ 0.43	+ 0.348	+ 0.237

They clearly show that the two $13/2^+$ configurations have very similar g factors. The measured g factor of ^{69m}Cu has a value very close to the calculated empirical g factors, indicating that one of these configurations is probably the main component in the wave function of the $13/2^+$ isomer.

To get a deeper insight into the structure of ^{69m}Cu, we have performed a full shell-model calculation in a spherical basis, using realistic interactions and single particle energies fitted to the data in this mass region to correct for the monopole term. The calculations were done with the OXBASH [Bro] and ANTOINE [Cau89] codes with the S3V [Sin92] and the modified Hjorth-Jensen *et al.* [HJ95] interactions, respectively.

We will first examine the results from the OXBASH calculations. They have the following features:

- the interaction is in the proton-neutron formalism;

- the active orbits of the interaction are $p_{3/2}, f_{5/2}, p_{1/2}$ and $g_{9/2}$ thus ^{56}Ni is considered as an inert core;

- we truncated additionally the interaction space (see Table 3.7). This was imposed by the time and memory requirements for completion of the job. In this manner, the actual core became ^{62}Ni.

As a result from these calculations, we obtained two $J^\pi = 13/2^+$ states separated only by a few 100 keV. The detailed composition of their wave functions is presented in Table 3.8. As one can see, the wave function of the first $13/2^+$ state is dominated by a configuration in which one neutron is excited from $f_{5/2}$ to $g_{9/2}$, while in the second observed state the neutron excitation is coming from the $p_{1/2}$ orbital.

After deriving the nuclear wave functions, we calculated the g factors of the two $13/2^+$ states using, respectively, free and effective g factors. We also calculated an empirical g factor, using empirical orbital and spin g facotrs for each pair of $L - S$ orbital (last two columns of Table 3.5).

Table 3.7: *Additional constraints on the number of particles on each individual orbit used in the OXBASH calculations.*

	protons		neutrons	
	min.	max.	min.	max.
$p_{3/2}$	0	1	4	4
$f_{5/2}$	0	1	2	6
$p_{1/2}$	0	1	0	2
$g_{9/2}$	0	1	0	4

Table 3.8: *Detailed composition of the nuclear wave functions obtained by the OXBASH calculation using the S3V interaction.*

first $13/2^+$ state		second $13/2^+$ state	
$\pi p_{3/2} \otimes \nu f_{5/2}^5 g_{9/2}$	77.4%	$\pi p_{3/2} \otimes \nu p_{1/2} g_{9/2}$	58.7%
$\pi p_{3/2} \otimes \nu p_{1/2} g_{9/2}$	6.3%	$\pi p_{3/2} \otimes \nu f_{5/2}^4 p_{1/2} g_{9/2}$	14.2%
$\pi p_{3/2} \otimes \nu f_{5/2}^3 g_{9/2}^3$	5.9%	$\pi p_{3/2} \otimes \nu f_{5/2}^5 g_{9/2}$	8.9%
$\pi p_{3/2} \otimes \nu f_{5/2}^4 p_{1/2} g_{9/2}^3$	3.0%	$\pi f_{5/2} \otimes \nu f_{5/2}^5 g_{9/2}$	5.0%

The obtained *g* factors for the $13/2^+$ isomer are presented in Table 3.9. They clearly show that the calculations performed using the free-nucleon *g* factors are quite far from the experimentally measured value. The agreement becomes better when effective *g* factors are used. Using empirical *g* factors for each pair of orbitals, we obtained much smaller values. The comparison of the experimental *g* factor with the OXBASH calculations shows that the two $13/2^+$ states in ^{69}Cu have strongly mixed configurations and very similar *g* factors. Therefore, with the measured *g* factor we cannot distinguish between them.

Table 3.9: *Calculated g factors for the two $13/2^+$ states as presented in Table 3.8.*

	free	effective	empirical
first $13/2^+$ state $(f^{-1}g)$	+ 0.268	+ 0.228	+ 0.147
second $13/2^+$ state $(p^{-1}g)$	+ 0.309	+ 0.256	+ 0.197

We performed the calculations also with the ANTOINE code using the modified Hjorth-Jensen *et al.* interaction, which is in the isospin

formalism. In this case, ^{56}Ni was the actual inert core and up to six-nucleon excitations were allowed to the $g_{9/2}$ orbital. No restrictions were imposed on the minimal number of particles on any of the $p_{3/2}, f_{5/2}$ and $p_{1/2}$ orbitals. Similarly to the previous calculations, there are again two $13/2^+$ states which appear very close in energy. The compositions of their wave functions are presented in Table 3.10. Note that the energy ordering of the two $13/2^+$ states is changed compared to the S3V calculations. The state with predominant $\pi p_{3/2} \otimes \nu p_{1/2} g_{9/2}$ configuration is lower in energy.

Table 3.10: *Detailed composition of the nuclear wave functions obtained by the ANTOINE calculation using the modified Hjorth-Jensen interaction.*

first $13/2^+$ state		second $13/2^+$ state	
$\pi p_{3/2} \otimes \nu p_{1/2} g_{9/2}$	44.4%	$\pi p_{3/2} \otimes \nu f_{5/2}^5 g_{9/2}$	55.0%
$\pi p_{3/2} \otimes \nu f_{5/2}^5 g_{9/2}$	25.3%	$\pi p_{3/2} \otimes \nu p_{1/2} g_{9/2}$	13.0%
$\pi p_{3/2} \otimes \nu f_{5/2}^4 p_{1/2} g_{9/2}^3$	9.6%	$\pi p_{3/2} \otimes \nu f_{5/2}^4 p_{1/2} g_{9/2}^3$	7.3%
$\pi p_{3/2} \otimes \nu p_{3/2}^3 g_{9/2}$	4.1%	$\pi p_{3/2} \otimes \nu f_{5/2}^3 g_{9/2}^3$	4.7%

We used the derived nuclear wave functions to calculate the g factors of the two states. In the ANTOINE code, there is no option to use different g factors for the different orbitals, thus we were restricted to the first two cases from the previously described calculation: the free nucleon single particle g factors and the effective g factors. The results are presented in Table 3.11.

Table 3.11: *g factors for the two $13/2^+$ calculated using the ANTOINE code.*

	free	effective
first $13/2^+$ state $(p^{-1}g)$	+ 0.240	+ 0.212
second $13/2^+$ state $(f^{-1}g)$	+ 0.301	+ 0.242

Similarly to the previous calculations, these results also show that the two $13/2^+$ states in ^{69}Cu are strongly mixed and with very similar g factors and we cannot distinguish between them using the experimental value.

3.4.2 ^{67}Ni case

^{67}Ni can be presented as a single-hole nucleus to the proposed doubly-magic ^{68}Ni. From this point of view, we should expect that the 9/2$^+$ isomer has a pure $\nu g_{9/2}$ configuration and thus have a *g* factor close to the Schmidt limit (-0.425) . If we compare the *g* factors of the isomeric state with other *g* factors of 9/2$^+$ states in the region, we obtain the picture presented in Fig. 3.52
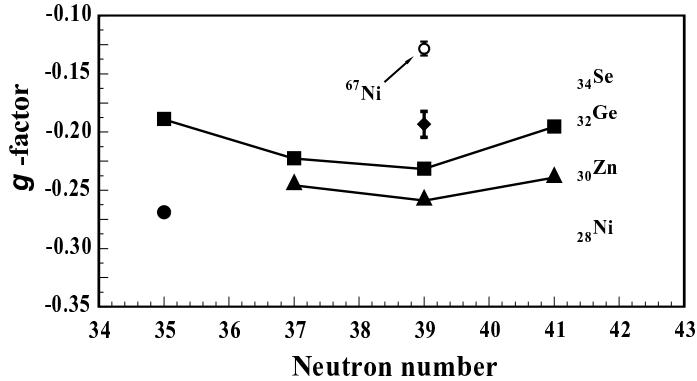
Figure 3.52: *Systematics of the g factors of the 9/2$^+$ states in the vicinity of ^{68}Ni. The solid lines connect the Ge and Zn isotopes, respectively. The measured g factor in ^{67m}Ni is depicted with an empty circle.*

One can clearly see that the experimentally derived *g* factor in ^{67m}Ni ($|g| = 0.1245(60)$) is far off the systematics in the region. In an attempt to understand the source of the discrepancy between the experimentally measured *g* factor and the expectation, we performed shell-model calculations. For this purpose, we used again the OXBASH and the AN-TOINE codes and the interactions as described for the ^{69}Cu case. We considered ^{56}Ni as an inert core and no restrictions were imposed on the number of particles on the $p_{3/2}, f_{5/2}, p_{1/2}$ and $g_{9/2}$ orbits. The detailed compositions of the wave-functions obtained in the two calculations are presented in Table 3.12.

It is clear that these calculations cannot reproduce the measured *g* factor. We attributed this to the fact that no core polarization effects were taken into account. Evidence for strong coupling of the Ni valence particles to the excitations of the ^{56}Ni core has been obtained by *g* factor measurements of the 2_1^+ states in the $^{56-64}$Ni isotopes [Ken01]. These

Table 3.12: *g factors and detailed compositions of the nuclear wave function for the $9/2^+$ state in ^{67}Ni as derived by the S3V [Sin92] and the modified Hjorth-Jensen [HJ95] interactions.*

interaction	wave function composition		g factor		
			free	effective	empirical
S3V	$\nu f_{5/2}^4 g_{9/2}$	43.5%	-0.407	-0.284	-0.259
	$\nu p_{1/2}^{-2} g_{9/2}$	19.8%			
	$\nu f_{5/2}^4 g_{9/2}^3$	11.8%			
	$\nu f_{5/2}^2 g_{9/2}^3$	6.6%			
	$\nu f_{5/2}^5 p_{1/2} g_{9/2}$	5.1%			
Hjorth-Jensen	$\nu f_{5/2}^4 g_{9/2}$	38.8%	-0.415	-0.290	
	$\nu g_{9/2}$	18.3%			
	$\nu f_{5/2}^4 g_{9/2}^3$	7.8%			
	$\nu p_{3/2}^2 g_{9/2}$	7.5%			
	$\nu p_{3/2}^2 f_{5/2}^4 g_{9/2}^3$	6.3%			

results could be reproduced only after increasing the configuration space to the full fp shell both for protons and neutrons and including up to 5-nucleon excitations from the $f_{7/2}$ into the remaining fp orbits. The core polarization was found to be crucial for ^{58}Ni, the nucleus closest to the doubly-magic core, but generally cross-shell excitations are expected to be even stronger in mid-shell semi-magic nuclei. Since the realistic interactions for current shell-model calculations, including the $g_{9/2}$ orbit, do not allow proton excitations across the $Z = 28$ gap, we have estimated their influence on the isomeric g factor using the naive shell model picture and the two-state configuration mixing approach in the spirit of Ref. [Ari54].

In the first order configuration mixing [Ari54], it is sufficient to exploit only such configurations that have a non-vanishing element of the magnetic moment operator with the configuration predicted by the single particle shell model (SPSM). These are configurations which differ by a single nucleon from the SPSM and are formed by a coupling of a pair of nucleons on $L - S$ orbital partners to form a state with $J^\pi = 1^+$. The wave function of such a mixed state should have the form:

$$\alpha_1 \Psi_1 \left(\left[(j_1{}^{n_1})_{0+} (j_2{}^{n_2})_{0+} (j^p)_j \right]_j \right) + \alpha_2 \Psi_2 \left(\left[(j_1{}^{n_1-1} j_2{}^{n_2+1})_{1+} (j^p)_j \right]_j \right) \quad (3.8)$$

where α_1 and α_2 are the mixing coefficients ($\alpha_1^2 + \alpha_2^2 = 1$ and α_2 is usually of the order of 0.1 [Ari54]); j_1 and j_2 is the pair of spin-orbit partners; n_1 and n_2 are the occupations of these orbits in the SPSM; Ψ_1 is the SPSM wave function and Ψ_2 is the admixture component.

The g factor of the core polarized state can be calculated using the relation for the $M1$ matrix element:

$$\langle \alpha_1 \Psi_1 + \alpha_2 \Psi_2 || \overrightarrow{M1} || \alpha_1 \Psi_1 + \alpha_2 \Psi_2 \rangle = \hspace{2cm} (3.9)$$
$$\alpha_1^2 \langle \Psi_1 || \overrightarrow{M1} || \Psi_1 \rangle + 2\alpha_1 \alpha_2 \langle \Psi_1 || \overrightarrow{M1} || \Psi_2 \rangle + \alpha_2^2 \langle \Psi_2 || \overrightarrow{M1} || \Psi_2 \rangle$$

where the last term is usually omitted due to the very small value of α_2^2. Using the empirical g factors from Ref. [Rag89, Mul89] and the additivity relation (eqn. 1.16), we can obtain the g factor of the mixed state as:

$$g(9/2^+) = \alpha_1^2(-0.269) + 2\alpha_1 \alpha_2(0.533) + \alpha_2^2(-0.167). \hspace{1cm} (3.10)$$

The derivation of the off-diagonal $M1$ matrix element is presented in detail in App. B. The correct sign of the product of $\alpha_1 \alpha_2$ and the off-diagonal $M1$ matrix element depend on the relative sign of the diagonal and off-diagonal matrix elements of the interaction causing the mixing (see e.g. [Bru77]). In this schematic calculation, we did not use any particular interaction thus we cannot determine the sign. We assumed a destructive correction according to the empirical rule that the first order core polarization quenches the g factor of the neutron $j = l + 1/2$ orbits [Noy59, Tow77].

Our calculations showed that a mixing amplitude of 0.13 ($\alpha_2^2 \sim 1.7\%$) is enough to explain the measured g factor (see Fig. 3.53). The strong dependence of the g factor on the mixing amplitude α_2 is caused by the very large (positive) value of the off-diagonal spin-flip $M1$ matrix element. The importance of this core excited configuration is emphasized by the strong interaction between $g_{9/2}$ neutrons and $f_{5/2}$ protons, an evidence for which can be found in the strong monopole shift of the proton $f_{5/2}$ levels in the Cu isotopes starting at $N \simeq 40$ [Fra98] (see Fig. 3.10).

For all these discussions, we have assumed a negative sign of the experimental g factor. Since in our measurement we determined only its absolute value, a positive sign is not excluded. However, it is much less probable because it would require a very large mixing ($\alpha_2^2 \sim 15\%$).

This result shows the extreme sensitivity of the g factor observable to particular components of the core excitation. Further developments
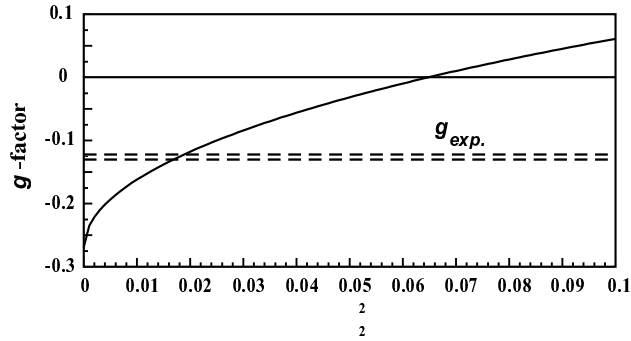
Figure 3.53: *The g factor of the mixed state as a function of the mixing* α_2^2. *The experimental g factor with its error-bars is presented by dashed lines.*

of the realistic interactions in larger shell model bases, including the full f, p and $g_{9/2}$ orbits, are necessary in order to explore the suggested core polarization.

3.4.3 ^{66}Co case

It is quite difficult to interpret the measured g factor of the 830 ns isomer in ^{66}Co. The spin/parity of the ground state is tentatively assigned to be 3^+ [Mue00]. The spin/parity of the isomeric states are not known. It is also not possible to perform shell-model calculations since the $f_{7/2}$ and $g_{9/2}$ orbitals should be included there. Nevertheless, we will examine the measured g factor assuming some particular pure configurations and we will try to find out what information we can derive from the measured g factor.

As a first approach, we will calculate the g factors for all possible combinations between the $f_{7/2}$ proton (the assumed proton configuration of ^{66}Co) and any of the neutron orbitals in the $f, p, g_{9/2}$ shell. The results for these calculations are presented in Table 3.4.3. There, one can clearly see that only states including the $g_{9/2}$ orbital in their wave function can have a g factor close to the measured value ($|g| = 0.157(9)$). All other neutron orbits give rise to a g factor of the order of 1 and higher.

Mueller *et al.* [Mue00] observed two β-decaying states both in ^{68}Co (Fig. 3.5) and ^{70}Co (Fig. 3.6). They did not find any evidence for a second β-decaying state in ^{66}Co at least not in the half-life limits of about

Table 3.13: *Table of the g factors, calculated using the additivity relation and, respectively, the free, effective and empirical single particle g factors, of the possible configurations between the proton $f_{7/2}$ and neutron $p_{3/2}, f_{5/2}, p_{1/2}$ and $g_{9/2}$ orbitals.*

configuration	g factor		
	free	effective	empirical
$g((\pi f_{7/2}\nu g_{9/2})_{1-})$	-4.065	-3.296	-3.154
$g((\pi f_{7/2}\nu g_{9/2})_{2-})$	-0.945	-0.7260	-0.682
$g((\pi f_{7/2}\nu g_{9/2})_{3-})$	-0.165	-0.0834	-0.064
$g((\pi f_{7/2}\nu g_{9/2})_{4-})$	0.147	0.1736	0.1832
$g((\pi f_{7/2}\nu g_{9/2})_{5-})$	0.303	0.302	0.3068
$g((\pi f_{7/2}\nu g_{9/2})_{6-})$	0.3921	0.3756	0.3774
$g((\pi f_{7/2}\nu g_{9/2})_{7-})$	0.4478	0.4215	0.4216
$g((\pi f_{7/2}\nu g_{9/2})_{8-})$	0.485	0.4521	0.4510
$g((\pi f_{7/2}\nu p_{1/2})_{3+})$	1.703	1.481	1.405
$g((\pi f_{7/2}\nu p_{1/2})_{4+})$	1.608	1.351	1.351
$g((\pi f_{7/2}\nu f_{5/2})_{1+})$	3.0405	2.707	2.724
$g((\pi f_{7/2}\nu f_{5/2})_{2+})$	1.7474	1.502	1.468
$g((\pi f_{7/2}\nu f_{5/2})_{3+})$	1.4241	1.201	1.154
$g((\pi f_{7/2}\nu f_{5/2})_{4+})$	1.2948	1.08	1.028
$g((\pi f_{7/2}\nu f_{5/2})_{5+})$	1.2301	1.02	0.965
$g((\pi f_{7/2}\nu f_{5/2})_{6+})$	1.1932	0.985	0.929
$g((\pi f_{7/2}\nu p_{3/2})_{2+})$	3.12	2.571	2.317
$g((\pi f_{7/2}\nu p_{3/2})_{3+})$	1.655	1.416	1.378
$g((\pi f_{7/2}\nu p_{3/2})_{4+})$	1.069	0.974	1.002
$g((\pi f_{7/2}\nu p_{3/2})_{5+})$	0.776	0.723	0.815

$1 - 5$ s [Mue]. However, one might expect, that the low energy structure of ^{66}Co is dominated by similar configurations, namely the coupling of the $f_{7/2}$ proton either to a $\nu g_{9/2}$ (creating a multiplet of negative parity states) or to a $\nu p_{1/2}$ (positive parity states). Thus, we can expect that the two γ-decaying isomeric states in ^{66}Co are, in a certain way, related to β-decaying isomeric states, similar to those in ^{68}Co and ^{70}Co.

An important point for the understanding of the puzzle is to fix the sequence of the two γ-decaying isomers. We measured the intensity of the 175 keV transition and compared it to the intensities of the 214 keV and 252 keV transitions. This was done in two cases - with an ion gate on ^{66}Co and on ^{71}Zn. In the γ-ray spectra gated on the ^{71}Zn, the long-

lived ^{66}Co isomeric γ-lines (241 keV and 252 keV) can appear due to accidental coincidences. However, the γ-line of the short-lived isomer (175 keV) should not be present at all, unless it is fed via the long-lived one. Thus, if the 175 keV line is present in the ^{71}Zn gated spectra, we might conclude that the short-lived isomer is fed by the long-lived one. However, a contamination in the 175 keV γ-line can come from neutron reactions in the Ge detectors (^{70}Ge $(n,\gamma)^{71}$Ge). To estimate this contribution we can use the 198 keV line, which is produced in the same reaction. Both of these lines correspond to the E_x = 198 keV, $t_{1/2}$ = 20 ms isomer in ^{71}Ge, which decays via two γ-transitions, 23 keV and 175 keV. Since this isomer is produced in the Ge detectors itself, it is very probable that both these γ-rays are detected in coincidence, which gives the 198 keV γ-line. Therefore, the relative intensity of the 175 keV and the 198 keV lines should depend only on the detector itself and not on the implanted heavy ion. Thus, comparing the intensity balance of the 252 keV, 175 keV and 198 keV lines in the ^{66}Co and ^{71}Zn gated γ-ray spectra, we should be able to deduce the contamination of the 175 keV (n,γ) in the 175 keV (^{66}Co) line. This should also give the answer, whether the short-lived isomer in ^{66}Co is fed by the long-lived one.

To derive the relative intensities of the above mentioned γ-lines in the ^{71}Zn gated γ-ray spectrum, we used the full 17 μs time window. However, in the ^{66}Co gated γ-ray spectra we wanted to avoid the direct production of the 175 keV line from the short-lived isomer. Therefore, we used an energy spectrum only from the last 7 μs (see Fig. 3.54).

The balance of the intensities of the 175 keV and 198 keV lines, relative to the 252 keV line (100%), is presented for the two cases in Table 3.14. No efficiency corrections were made. We can conclude that:

Table 3.14: *Intensities of the 175 keV and 198 keV lines, relative to the 252 keV (100%), for the two cases of ^{66}Co and ^{71}Zn ion gates.*

	^{66}Co	^{71}Zn
175 keV	110(4)%	135(9)%
198 keV	37(2)%	114(8)%
$I(175) - 1/4 I(198)$	$\sim$ 100 %	$\sim$ 100 %

- the intensity ratio $I(175)/I(198)$ is different in the ^{66}Co and ^{71}Zn gated spectra. This suggests that the 175 keV line is fed via the long-lived isomer. In that case $I(175)$ should be similar ($\sim$ 100 %)
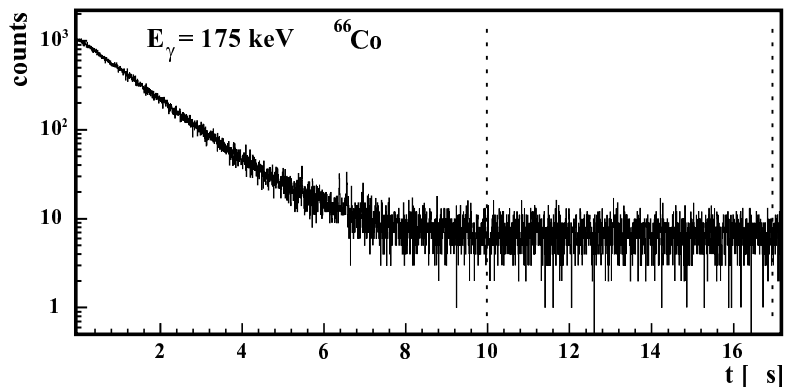
Figure 3.54: ^{66}Co gated time spectrum for the 175 keV line. Only the last part of the spectrum (between the dashed lines), was used to produce the energy spectrum, from which we derived the relative intensity of the 175 keV, 198 keV and 252 keV lines in ^{66}Co.

to $I(252)$. The higher intensity, $I(175)$, comes from the contamination via the (n, γ) reaction.

- the amount of the contamination in the 175 keV line is about 1/4 of the intensity of the 198 keV line ($I(175) - 1/4I(198) \approx 100$ %).

This clearly indicates that the long-lived isomer feeds directly the short-lived one.

Another point on which one can speculate is whether it is possible to have two β-decaying states in ^{66}Co, similarly to the case in ^{68}Co and ^{70}Co. Mueller *et al.* [Mue00] did not find evidence for such a state. However, they also mentioned that they did not observe the 471 keV line which, according to Bosch *et al.* [Bos88], should account for 20% of the β-decay. In their work, Bosch *et al.* actually did not find subsequent γ-rays following the 471 keV transition and they put it tentatively at 2.9 MeV. An interesting point is that the same 471 keV transition was also found in deep-inelastic reaction studies [Paw94] where it is situated close to a negative parity multiplet, without any spin/parity assignment. We can speculate that the initial state of the 471 keV transition has a negative parity. This would suggest the presence of a second β decaying state in ^{66}Co. This means that we have two options for investigation: i) two γ-decaying isomers built on top of a positive parity ground state;

ii) the same isomers built on top of a β decaying negative parity state.

From the point of view of lifetimes, we can say that the short-lived isomer decays most probably via an $E2$ or $E1$ transition, while the de-exciting transition of the long-lived isomer has possibly an $M2$ or $E3$ character.

Another experimental fact is that the 214 keV and 252 keV transitions are observed in coincidence, while the 175 keV transition is not in coincidence with other transitions.
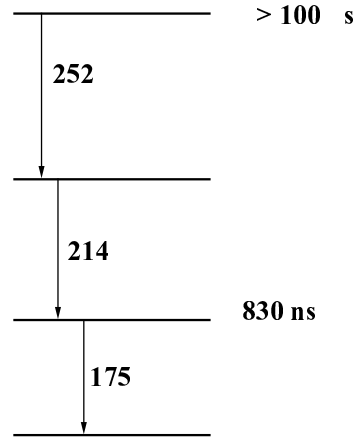
Figure 3.55: *Proposed level schemes for the isomers in* ^{66}Co.

Considering the above mentioned argument, we can propose a level scheme for the two isomers in ^{66}Co (see Fig. 3.55). It is build on the experimental fact that the two de-exciting transitions of the long-lived isomer are feeding the short-lived isomer. All what we can say about the the short-lived isomeric state is that it has a negative parity.

We can conclude that more investigations of the structure of ^{66}Co are needed for its better understanding. There are still many open questions to be answered.

Chapter 4

Conclusions and Outlook

In this work we discussed the results from two different experiments unified by a common object of investigation, the g-factor observable, and by a common method of production and selection of the nuclear species of interest: intermediate energy projectile-fragmentation followed by in-flight fragment separation.

In the first part we examined the results of a measurement of the ground state magnetic moment of ^{32}Cl. The method which we used was the β-NMR on reaction-oriented nuclei. An important experimental point in this measurement was the collection of full energy β-spectra, which allowed us to discriminate between branches of the β-decay of ^{32}Cl with opposite sings of their radiation parameters and in this way to increase considerably the amplitude of the observed β asymmetry.

The obtained magnetic dipole moment of the 1^+ ground state of ^{32}Cl ($\mu = 1.114(6)\mu_N$) was compared with the theoretical calculations. At first glance the experimental value is very close to the Schmidt limit. However, a more detailed study, using large scale shell model calculations, revealed that the initial assumption for a rather simple single-particle configuration is misleading. We used a renormalized $M1$ operator to account for the mesonic exchange currents and the higher order configuration mixing. The calculations were performed using three different interactions (USD, SDPOTA and SDPOTB), fitted in the sd shell. The results indicate that the SDPOTA Hamiltonian works best in the $A = 31 - 33$ region. However, to make a general conclusion about the Hamiltonian, one needs to carry out a comparison between M1 observables and those calculated with SDPOTA for other sd-shell nuclei.

In the second part of the thesis we discussed the results of the g-factor measurement on isomeric states in the neutron-rich ^{68}Ni region.

In this measurement we used the combination of the heavy ion - γ correlation technique together with the TDPAD method. In this experiment we applied for the first time these two methods to measure g factors of nuclear states produced in projectile-fragmentation reactions. This is possible due to the spin-alignment obtained in the reaction mechanism.

The result which we obtained for the g factor of the $13/2^+$ isomeric state in ^{69}Cu is $|g| = 0.213(25)$. We performed shell model calculations using the S3V [Sin92] and the modified Hjorth-Jensen [HJ95] interactions. There are two states with $J^\pi = 13/2^+$ which appear very close in energy in both of the calculations. One of the states has a dominant $\pi p_{3/2} \otimes \nu p_{1/2} g_{9/2}$ component in its wave function, while in the second one the $\pi p_{3/2} \otimes \nu f_{5/2}^{-1} g_{9/2}$ component is superior. However, both of them have strongly mixed configurations. The g factors of these two states have very similar values and with our measurement we cannot distinguish which of them is the isomeric state.

We measured the g factor of the $9/2^+$ isomer in ^{67}Ni to be $|g| = 0.125(6)$. This value is much smaller than other g factors of $9/2^+$ states in the region. The comparison with shell model calculations showed that the measured g factor could not be reproduced within the $p_{3/2}, f_{5/2}, p_{1/2}, g_{9/2}$ model space. This suggests that excitation from the $f_{7/2}$ orbit across the 28 shell gap can play an important role in the structure of the studied isomer. We estimated the influence of the first order core polarization in the approach of Ref. [Ari54, Noy59]. The result showed that $\sim 1.7\%$ mixing of the spin-flip $(\pi(f_{7/2}^{-1} f_{5/2})_{1^+} \otimes \nu g_{9/2})_{9/2^+}$ configuration into the wave function of the isomer can reproduce the experimental g factor. This shows the extreme sensitivity of the g factor observable to the detailed composition of the nuclear wave function. In order to further explore the suggested core excitation it is necessary to develop realistic interactions in larger shell-model bases, including the full $f, p, g_{9/2}$ orbits.

The g factor which we measured for the 830 ns isomeric state in ^{66}Co is $|g| = 0.157(9)$. Its interpretation is rather difficult since the spin and parity neither of the ground nor of the excited states in ^{66}Co are firmly assigned. There are no realistic shell-model calculations at the moment which can include both the f, p and $g_{9/2}$ shells. The experimental g factor suggests the presence of $g_{9/2}$ particles into the wave function of the isomer. However, we cannot propose a consistent picture of the (assumed) low-energy structure of ^{66}Co without unjustified assumptions.

Further investigations are needed for its better understanding.

In the same experiment we also measured the half-life of the 286 keV state in ^{71}Zn ($t_{1/2} = 46(4)ns$). The obtained reduced transition probability ($B(E2) = 16$ *W.u.*) confirms its previously proposed $J^{\pi} = 5/2^{+}$ assignment.

With the work presented in this thesis we have shown the feasibility of the g factor measurements, both on ground and isomeric states, of nuclei produced in projectile-fragmentation reactions. This opens up the possibility to study regions of exotic nuclei further away from the line of β stability. The g factor observable can serve as a stringent test for nuclear models.

Our results suggest, that the particle-hole excitations across the $Z = 28$ shell gap have strong impact on the properties of ^{67m}Ni. One would expect such a situation at mid-shell nuclei, and from this point of view our results do not support the proposed sub-shell closure at $N = 40$. However, more investigations in the region are necessary in order to gain deeper insight into its structure. It would be interesting to measure the g factors of other $g_{9/2}$ states in the vicinity (e.g., the ground state of ^{69}Ni), which are assumed to have quite pure configurations, as well as the interaction between the $g_{9/2}$ neutrons with particle on other proton and neutron orbitals in the region. Good candidates for this are the g factors of the isomeric states in ^{69}Ni, ^{70}Ni and ^{71}Cu.

Appendix A

A.1 Clebsch-Gordan coefficients

In order to obtain a two-particle state with definite angular momentum (IM) when nucleons occupy the single-particle orbits j_1 and j_2, one has to take a linear combination of various ψ_{jm}. The coefficients $\langle j_1 j_2 m_1 m_2 | IM \rangle$ in the expansion

$$\Psi_{IM}(1,2) = \sum_{m_1 m_2} \langle j_1 j_2 m_1 m_2 | IM \rangle \psi_{j1m1}(1) \psi_{j_2 m_2}(2) \qquad (A.1)$$

are called Clebsch-Gordan coefficients and are chosen so that the relations

$$\mathbf{J}^2 \Psi_{IM}(1,2) = I(I+1)\Psi_{IM}(1,2)$$
$$\mathbf{J_z} \Psi_{IM}(1,2) = M\Psi_{IM}(1,2)$$

are satisfied.

Since the angular momentum operator of the two-particle state is a sum of the operators of the individual states, these coefficients vanish unless

$$m_1 + m_2 = M$$

and

$$|j_1 - j_2| \leq I \leq j_1 + j_2$$

The physical interpretation of the Clebsch-Gordan coefficients comes from the orthonormality of ψ_{jm}. Thus

$$\langle j_1 j_2 m_1 m_2 | IM \rangle = \langle \psi_{j_2 m_2}(2) \psi_{j_1 m_1}(1) | \Psi_{IM}(1,2) \rangle$$

131

which means that $\langle j_1 j_2 m_1 m_2 | I M \rangle^2$ is the probability that in state $\Psi_{IM}(1,2)$ particle number 1 is in the state $(j_1 m_1)$ and particle number 2 in state $(j_2 m_2)$.

From the fact that ψ_{jm} and ψ_{IM} are orthonormal states it follows

$$\sum_{m_1 m_2} \langle j_1 j_2 m_1 m_2 | I M \rangle \langle j_1 j_2 m_1 m_2 | I' M' \rangle = \delta_{II'} \delta_{MM'}$$

and because Ψ_{IM} are complete set of states

$$\sum_{m_1 m_2} \langle j_1 j_2 m_1 m_2 | I M \rangle \langle j_1 j_2 m_1' m_2' | I M \rangle = \delta_{m_1 m_1'} \delta_{m_2 m_2'}$$

As a consequence equation (A.1) can be rewritten in the form:

$$\psi_{j_1 m_1}(1) \psi_{j_2 m_2}(2) = \sum_{IM} \langle j_1 j_2 m_1 m_2 | I M \rangle \psi_{IM}(1,2) \qquad (A.2)$$

There is the following relation between the Clebsch-Gordan coefficients and the Wigner $3j$ symbols

$$\langle j_1 j_2 m_1 m_2 | I M \rangle = (-1)^{j_1 - j_2 + M} \sqrt{(2I+1)} \begin{pmatrix} j_1 & j_2 & I \\ m_1 & m_2 & M \end{pmatrix} \qquad (A.3)$$

Some basic symmetry properties of the Clebsch-Gordan coefficients are presented below

$$\langle j_1 j_2 m_1 m_2 | I M \rangle = (-1)^{j_1 + j_2 - I} \langle j_2 j_1 m_2 m_1 | I M \rangle \qquad (A.4)$$

$$\langle j_1 j_2 m_1 m_2 | I M \rangle = (-1)^{j_1 + j_2 - I} \langle j_1 j_2 - m_1 - m_2 | I - M \rangle \qquad (A.5)$$

$$\langle j_1 j_2 m_1 m_2 | I M \rangle = (-1)^{j_1 - m_1} \sqrt{\left(\frac{2I+1}{2j_2+1} \right)} \langle j_1 I m_1 - M | j_2 - m_2 \rangle \qquad (A.6)$$

A.2   The Wigner-Eckart theorem

An irreducible tensor of rank λ is an operator with $(2\lambda + 1)$ components $Q_{\lambda \mu}$ that satisfy the commutation relations

$$[\mathbf{J}_z, Q_{\lambda \mu}] = \mu Q_{\lambda \mu} \qquad (A.7)$$

$$[\mathbf{J}_\pm, Q_{\lambda \mu}] = \sqrt{(\lambda \mp \mu)(\lambda \pm \mu + 1)} Q_{\lambda \mu \pm 1} \qquad (A.8)$$

Clearly the angular-momentum wave-functions ψ_{IM} are irreducible tensors. A product of two irreducible tensor operators

$$Q_{\lambda_3 \mu_3} = \sum_{\lambda_3 \mu_3} \langle \lambda_1 \lambda_2 \mu_1 \mu_2 | \lambda_3 \mu_3 \rangle Q_{\lambda_1 \mu_1} Q_{\lambda_2 \mu_2} \qquad (A.9)$$

is also an irreducible tensor operator of rank λ_3.

We can now consider the evaluation of the matrix element $\langle \Psi_{I'M'} | Q_{\lambda\mu} | \Psi_{IM} \rangle$ where $\Psi_{I'M'}$, $Q_{\lambda\mu}$ and Ψ_{IM} are irreducible tensor operators of rank I, λ and I' respectively. From equation (A.9) it follows that

$$Q_{\lambda\mu} \Psi_{IM} = \sum_{I''M''} \langle I\lambda M\mu | I''M'' \rangle \Phi_{I''M''} \qquad (A.10)$$

Since $\Phi_{I''M''}$ is a product of two irreducible tensor operators it is also an irreducible tensor operator of rank I''. Because states with different values of I and M are orthogonal, it is clear that

$$\langle \Psi_{I'M'} | Q_{\lambda\mu} | \Psi_{IM} \rangle = \langle I\lambda M\mu | I'M' \rangle \langle \Psi_{I'M'} | \Phi_{I'M'} \rangle \qquad (A.11)$$

It is also possible to show that $\langle \Psi_{I'M'} | \Phi_{I'M'} \rangle$ does not dependent on M'.

$$
\begin{aligned}
\langle \Psi_{I'M'+1} | \Phi_{I'M'+1} \rangle &= \frac{1}{\sqrt{(I'-M')(I'+M'+1)}} \langle J_+ \Psi_{I'M'} | \Phi_{I'M'+1} \rangle \\
&= \frac{1}{\sqrt{(I'-M')(I'+M'+1)}} \langle \Psi_{I'M'} | J_- \Phi_{I'M'+1} \rangle \\
&= \langle \Psi_{I'M'} | \Phi_{I'M'} \rangle \\
&\equiv \langle \Psi_{I'} \| Q_\lambda \| \Psi_I \rangle
\end{aligned}
$$

Thus we arrive at the Wigner-Eckart theorem which states that if Ψ_{IM}, $Q_{\lambda\mu}$ and $\Psi_{I'M'}$ are irreducible tensor of rank I, λ and I' then

$$\langle \Psi_{I'M'} | Q_{\lambda\mu} | \Psi_{IM} \rangle = \langle I\lambda M\mu | I'M' \rangle \langle \Psi_{I'} \| Q_\lambda \| \Psi_I \rangle \qquad (A.12)$$

where the reduced matrix element $\langle \Psi_{I'} \| Q_\lambda \| \Psi_I \rangle$ is independent on the z component of angular momentum.

Appendix B

B.1 Magnetic moments in case of configuration mixing.

Let us consider the magnetic moment of a state $|JM\rangle$ which can be presented as a mixture of two pure shell model configurations $|\alpha; JM\rangle$ and $|\beta; JM\rangle$. For the wave function of the mixed state we have

$$|JM\rangle \;=\; \sqrt{1-a^2}|\alpha; JM\rangle + a|\beta; JM\rangle$$

and for the magnetic moment

$$
\begin{aligned}
\mu \;\equiv\;& \sqrt{\frac{4\pi}{3}}\sqrt{\frac{J}{(J+1)(2J+1)}}\;\langle JJ\|\mathbf{M1}\|JJ\rangle = \\
=\;& \sqrt{\frac{4\pi}{3}}\sqrt{\frac{J}{(J+1)(2J+1)}}\;\Big[a^2\langle\beta; J\|\mathbf{M1}\|\beta; J\rangle \\
+\;& (1+a^2)\langle\alpha; J\|\mathbf{M1}\|\alpha; J\rangle + 2a\sqrt{(1-a^2)}\langle\alpha; J\|\mathbf{M1}\|\beta; J\rangle\Big]
\end{aligned}
\tag{B.1}
$$

Now we can calculate the g-factor of the mixed state as

$$
\begin{aligned}
g(JM) \;=\;& \frac{\mu(JM)}{J} = \Big[a^2 g(\beta; J) + (1-a^2)g(\alpha; J) \\
+\;& 2a\sqrt{1-a^2}\sqrt{\frac{4\pi}{3J(J+1)(2J+1)}}\langle\alpha; J\|\mathbf{M1}\|\beta; J\rangle\Big]
\end{aligned}
\tag{B.2}
$$

135

which for the case of $J = 9/2$ becomes

$$
\begin{aligned}
g(9/2) &= a^2 g(\beta; 9/2) + (1 - a^2) g(\alpha; 9/2) + \\
&+ 2a\sqrt{1 - a^2}\sqrt{\frac{4\pi}{3}}\frac{2}{3}\frac{1}{\sqrt{110}}\langle\alpha; 9/2\|\mathbf{M1}\|\beta; 9/2\rangle \quad \text{(B.3)}
\end{aligned}
$$

thus we have to calculate the off-diagonal term $\langle\alpha; 9/2\|\mathbf{M1}\|\beta; 9/2\rangle$.

Note that, since we are calculating the matrix element between states with equal spins $(J_i = J_f)$ the symmetrical off-diagonal matrix elements are identical

$$
\langle\alpha; J_f\|\mathbf{M1}\|\beta; J_i\rangle = (-1)^{J_i - J_f}\langle\beta; J_i\|\mathbf{M1}\|\alpha; J_f\rangle = \langle\beta; J_i\|\mathbf{M1}\|\alpha; J_f\rangle \quad \text{(B.4)}
$$

For the particular case when

$$
\begin{aligned}
|\alpha; JM\rangle &= |\pi(f_{7/2}^8)^{(0)}\,\nu(g_{9/2}); J = 9/2, M\rangle \\
|\beta; JM\rangle &= |\pi(f_{7/2}^7 f_{5/2})^{(1)}\,\nu(g_{9/2}); J = 9/2, M\rangle
\end{aligned}
$$

we obtain for the off-diagonal term

$$
\begin{aligned}
\langle\alpha; 9/2&\|\mathbf{M1}\|\beta; 9/2\rangle = \langle\beta; 9/2\|\mathbf{M1}\|\alpha; 9/2\rangle = \\
&= \langle\pi(f_{7/2}^7 f_{5/2})^{(1)}\nu(g_{9/2}); 9/2\|\sum_{k=1}^{9}(g_\ell(k)\ell(k) \\
&\qquad\qquad\qquad +g_s(k)s(k))\|\pi(f_{7/2}^8)^{(0)}\nu(g_{9/2}); 9/2\rangle = \\
&= \langle\pi(f_{7/2}^7 f_{5/2})^{(1)}\nu(g_{9/2}); 9/2\|\sum_{k=1}^{8}(g_\ell^\pi(k)\ell(k) \\
&\qquad\qquad\qquad +g_s^\pi(k)s(k))\|\pi(f_{7/2}^8)^{(0)}\nu(g_{9/2}); 9/2\rangle + \\
&+ \langle\pi(f_{7/2}^7 f_{5/2})^{(1)}\nu(g_{9/2}); 9/2\|g_\ell^\nu(k)\ell(k) \\
&\qquad\qquad\qquad +g_s^\nu(k)s(k)\|\pi(f_{7/2}^8)^{(0)}\nu(g_{9/2}); 9/2\rangle
\end{aligned}
$$

where after applying some standard formulae to calculate the matrix element for the product of two operators, each of which is operating on different coordinates of the wave function, we get

$$
\begin{aligned}
&\langle\alpha; 9/2\|\mathbf{M1}\|\beta; 9/2\rangle = \\
&= (-1)^{1+9/2+9/2+1}\delta_{9/2,9/2}\sqrt{10\cdot 10}\underbrace{\begin{Bmatrix} 9/2 & 1 & 9/2 \\ 1 & 9/2 & 0 \end{Bmatrix}}_{=\frac{1}{\sqrt{30}}} \times
\end{aligned}
$$

$$\times \quad \langle \pi (f_{7/2}^7 f_{5/2})^{(1)} \| \sum_{k=1}^8 (g_\ell^\pi(k)\ell(k) + g_s^\pi(k)s(k)) \| \pi(f_{7/2}^8)^{(0)} \rangle + \underbrace{C\delta_{1,0}}_{=0}$$

$$= \quad -\sqrt{\frac{10}{3}} \langle \pi(f_{7/2}^7 f_{5/2})^{(1)} \| \sum_{k=1}^8 (g_\ell^\pi(k)\ell(k)$$
$$+ g_s^\pi(k)s(k)) \| \pi(f_{7/2}^8)^{(0)} \rangle \tag{B.5}$$

where we have a matrix element of the **M1** operator between states of eight particles. In order to calculate it we have to reduce it to a superposition of single-particle matrix elements. It is convenient to do this in isospin formalism. Any one-body operator can be presented as a linear combination of an isoscalar and an isovector part. For **M1** we have

$$\mathbf{M1} \quad = \quad \sum_{k=1}^A \left\{ \left[\frac{1}{2}(1 - \tau_z(k))g_\ell^\pi + \frac{1}{2}(1 + \tau_z(k))g_\ell^\nu \right] \ell(k) \right.$$

$$+ \quad \left. \left[\frac{1}{2}(1 - \tau_z(k))g_s^\pi + \frac{1}{2}(1 + \tau_z(k))g_\ell^\nu \right] s(k) \right\} =$$

$$= \quad \underbrace{\sum_{k=1}^A \left[\frac{1}{2}(g_\ell^\pi + g_\ell^\nu)\ell(k) + \frac{1}{2}(g_s^\pi + g_s^\nu)s(k) \right]}_{isoscalar\ part\ (T=0)}$$

$$+ \quad \underbrace{\sum_{k=1}^A \left[\frac{1}{2}(g_\ell^\pi - g_\ell^\nu)\ell(k) + \frac{1}{2}(g_s^\pi - g_s^\nu)s(k) \right] \tau_z(k)}_{isovector\ part\ (T=1)}$$

thus for the proton operator we obtain

$$\mathbf{M1} \quad = \quad \underbrace{\sum_{k=1}^8 \left[\frac{1}{2}(g_\ell^\pi + g_\ell^\nu)\ell(k) + \frac{1}{2}(g_s^\pi + g_s^\nu)s(k) \right]}_{\mathbf{M1}_{T=0}}$$

$$+ \quad \underbrace{\sum_{k=1}^8 \left[\frac{1}{2}(g_\ell^\pi - g_\ell^\nu)\ell(k) + \frac{1}{2}(g_s^\pi - g_s^\nu)s(k) \right]}_{\mathbf{M1}_{T=1}} \tag{B.6}$$

Further we have to calculate the reduced matrix element of the isoscalar and isovector parts of **M1** in isospin space for which we apply the

Wigner-Eckart theorem

$$\langle \pi(f_{7/2}^7 f_{5/2})^{(1)}\|\mathbf{M1}\|\pi(f_{7/2}^8)^{(0)}\rangle =$$
$$= \langle f_{7/2}^7 f_{5/2}; 1,4,4\|\mathbf{M1}_{T=0}\|f_{7/2}^8; 0,4,4\rangle$$
$$+\langle f_{7/2}^7 f_{5/2}; 1,4,4\|\mathbf{M1}_{T=1}\|f_{7/2}^8; 0,4,4\rangle =$$
$$= \frac{1}{3}\Big[\langle f_{7/2}^7 f_{5/2}; 1,4\||\mathbf{M1}_{T=0}\||f_{7/2}^8; 0,4\rangle$$

$$+\underbrace{\langle 4\,4\,1\,0|4\,4\rangle}_{=\frac{2}{\sqrt5}}\langle f_{7/2}^7 f_{5/2}; 1,4\||\mathbf{M1}_{T=1}\||f_{7/2}^8; 0,4\rangle\Big]$$

$$= \frac{1}{3}\Big[\langle f_{7/2}^7 f_{5/2}; 1,4\||\mathbf{M1}_{T=0}\||f_{7/2}^8; 0,4\rangle$$
$$+ \langle f_{7/2}^7 f_{5/2}; 1,4\||\mathbf{M1}_{T=1}\||f_{7/2}^8; 0,4\rangle\Big] \tag{B.7}$$

At this point we have to calculate the 8 particles matrix element of the isoscalar and isovector part of **M1** operator. For this we can use formula (10.105) from [Bru77]

$$\langle f_{7/2}^7 f_{5/2}; 1,4\||\mathbf{M1}_T\||f_{7/2}^8; 0,4\rangle =$$
$$= (-1)^{1+(0+4)+(1+4)+(7/2+7/2)+(8+4)+(7/2+7/2)+(1+T)-1}\times$$
$$\times\ \sqrt{1944}\underbrace{\langle\frac{5}{2}\frac12\frac52|\ \}\frac52\ \begin{smallmatrix}0\\\ \end{smallmatrix}\ 0\ 0\rangle}_{=1}\times\underbrace{\langle\frac72\begin{smallmatrix}8\\\ \end{smallmatrix}\ 0\ 4|\ \}\frac72\begin{smallmatrix}7\\\ \end{smallmatrix}\frac72\frac72\rangle}_{=1}$$
$$\times\ \sum_\nu\underbrace{U\left(\frac72 0 1\frac52;\nu\frac52\right)}_{\delta_{\nu,7/2}}\underbrace{U\left(\frac72 0 4\frac12;T_\nu\frac12\right)}_{\delta_{T_\nu,7/2}}\underbrace{U\left(0\frac72 0\frac72;\nu 0\right)}_{\delta_{\nu,7/2}}\underbrace{U\left(0\frac72 4\frac12;T_\nu 4\right)}_{\delta_{T_\nu,7/2}}$$
$$\times\ \underbrace{\left\{\begin{matrix}5/2 & 7/2 & 1\\0 & 1 & \nu\end{matrix}\right\}}_{=-\frac{1}{\sqrt{24}}\delta_{\nu,7/2}}\left\{\begin{matrix}1/2 & 1/2 & T\\4 & 4 & T_\nu\end{matrix}\right\}\langle f_{5/2}\||\mathbf{M1}_T\||f_{7/2}\rangle$$
$$= (-1)^{T+1}9\sqrt{24}\left(-\frac{1}{\sqrt{24}}\right)\left\{\begin{matrix}1/2 & 1/2 & T\\4 & 4 & 7/2\end{matrix}\right\}\langle f_{5/2}\||\mathbf{M1}_T\||f_{7/2}\rangle =$$
$$= \begin{cases}\frac{3}{\sqrt2}\langle f_{5/2}\||\mathbf{M1}_{T=0}\||f_{7/2}\rangle\\[2ex]\frac12\sqrt{\frac{15}{2}}\langle f_{5/2}\||\mathbf{M1}_{T=1}\||f_{7/2}\rangle\end{cases} \tag{B.8}$$

Calculation of the single-particle matrix elements of the **M1** operator
for its isoscalar and isovector part gives respectively

$$\langle f_{5/2}|||\mathbf{M1}_{T=0}|||f_{7/2}\rangle = (-1)^3\sqrt{\frac{3}{4\pi}}\sqrt{48}\left[\frac{1}{2}(g_\ell^\pi + g_\ell^\nu)(-1)^{7/2+3/2}\sqrt{168}\times\right.$$

$$\times \underbrace{\left\{\begin{array}{ccc} 3 & 3 & 1 \\ 7/2 & 5/2 & 1/2 \end{array}\right\}}_{=-\frac{1}{14\sqrt{6}}} + \frac{1}{2}(g_s^\pi + g_s^\nu)(-1)^{5/2+3/2}\sqrt{3}\left.\underbrace{\left\{\begin{array}{ccc} 1/2 & 1/2 & 1 \\ 7/2 & 5/2 & 3 \end{array}\right\}}_{=-\frac{1}{\sqrt{21}}}\right] =$$

$$= -\sqrt{\frac{3}{4\pi}}2\sqrt{\frac{3}{7}}\left[(g_\ell^\pi + g_\ell^\nu) - (g_s^\pi - g_s^\nu)\right] \tag{B.9}$$

and

$$\langle f_{5/2}|||\mathbf{M1}_{T=1}|||f_{7/2}\rangle = -\sqrt{\frac{3}{4\pi}}\frac{6}{\sqrt{7}}\left[(g_\ell^\pi - g_\ell^\nu) - (g_s^\pi - g_s^\nu)\right] \quad \text{(B.10)}$$

Thus for the 8-particle wave function after applying formula (B.8) we
get

$$\langle (f_{7/2}f_{5/2};14|||\mathbf{M1}_{T=0}|||f_{7/2}^8;04\rangle = -\sqrt{\frac{3}{4\pi}}3\sqrt{\frac{6}{7}}\left[(g_\ell^\pi + g_\ell^\nu) - (g_s^\pi + g_s^\nu)\right]$$

$$\langle (f_{7/2}f_{5/2};14|||\mathbf{M1}_{T=1}|||f_{7/2}^8;04\rangle = -\sqrt{\frac{3}{4\pi}}3\sqrt{\frac{15}{14}}\left[(g_\ell^\pi - g_\ell^\nu) - (g_s^\pi - g_s^\nu)\right] \text{ (B.11)}$$

Then using formula (B.7) we can calculate the matrix element for
the proton part of the **M1** operator

$$\langle \pi(f_{7/2}^7 f_{5/2})^{(1)}||\mathbf{M1}_\pi||\pi(f_{7/2}^8)^{(0)}\rangle = -\sqrt{\frac{3}{4\pi}}2\sqrt{\frac{6}{7}}(g_\ell^\pi - g_s^\pi) \quad \text{(B.12)}$$

and substituting the result in formula (B.5) we obtain the complete off-
diagonal term

$$\langle \alpha;9/2||\mathbf{M1}||\beta;9/2\rangle = \sqrt{\frac{3}{4\pi}}4\sqrt{\frac{5}{7}}(g_\ell^\pi - g_s^\pi) \tag{B.13}$$

For the calculation of the off-diagonal matrix element of the **M1**
operator we can use experimental g-factors of $f_{7/2}$ and $f_{5/2}$ orbitals from

the region (for example $g(f_{7/2}) = 1.378$ for ^{55}Co and $g(f_{5/2}) = 0.669$ for ^{71}As [Rag89]) and obtain the effective orbital and spin g-factors

$$g_\ell^{eff.} \quad = \quad 1.0235$$

and

$$g_s^{eff.} \quad = \quad 3.5045$$

Thus we can substitute the final values in equation (B.3) and rewrite it

$$g(9/2) \quad = \quad a^2(-0.167) + (1 - a^2)(-0.269) + 2a\sqrt{1 - a^2}(0.533) \tag{B.14}$$

where we have used the experimental value for $g(\nu g_{9/2})$ [Mul89] and we have calculated the g-factor for pure configuration $|\beta; JM\rangle$ using the additivity relation (1.16).

Bibliography

[Alf80]   W. Alford, R. Boyd, E. Sugarbaker, D. Hanson, and E. Flynn, *(t,p) Reaction on ^{56}Fe, $^{58,60,64}Ni$: Structure and Reaction-Mechanism Effects*, Phys. Rev. **C21** (1980) 1203.

[Ame98]   F. Ameil, M. Bernas, P. Armbruster, S. Czajkowski, P. Dessagne, H. Geissel, E. Hanelt, C. Kozhuharov, C. Miehe, C. Donzaud, A. Grewe, A. Heinz, Z. Janas, M. de Jong, W. Schwab, and S. Steinhauser, *beta-Decay Half-Lives of Very Neutron-Rich Isotopes of Elements from Ti to Ni*, Eur.Phys.J. **A1** (1998) 275.

[Ann87]   R. Anne, D. Bazin, A. Mueller, J. Jacmart, and M. Langevin, *The Achromatic Spectrometer Lise At Ganil*, Nucl. Instrum. Methods Phys. Res. **A257** (1987) 215-232.

[Ari54]   A. Arima and H. Horie, *Configuration Mixing and Magnetic Moments of Odd Nuclei*, Progr. Theor. Phys. **12** (1954) 623 - 641.

[Arn88]   E. Arnold, J. Bonn, W. Neu, R. Neugart, E. Otter, and the ISOLDE collaboration, *Quadrupole Interaction of ^{8}Li and ^{9}Li in $LiNbO_3$ and the Quadrupole Moment of ^{9}Li*, Z. Phys. **A331** (1988) 295.

[Arn92]   E. Arnold, J. Bonn, A. Klein, R. Neugart, M. Neuroth, E. Otten, P. Lievens, H. Reich, W. Widdra, and the ISOLDE Collaboration, *Quadrupole Moment of ^{11}Li*, Phys. Lett. **B281** (1992) 16.

[AS81]   F. Ajzenberg-Selove, R. Brown, E. Flynn, and J.W.Sunier, *States of ^{69}Cu*, Phys. Rev. **C24** (1981) 1762.

[Asa90]   K. Asahi, M. Ishihara, N. Anabe, T. Ichihara, T. Kubo,
          M. Adachi, H. Takanashi, M. Kouguchi, M. Fukuda, D. Miko-
          las, D. Morrissey, D. Beaumel, T. Shimoda, H. Miyatake, and
          N. Takahashi, *New Aspect of Intermediate Energy Heavy Ion
          Reactions. Large Spin Polarization of Fragments*, Phys. Lett.
          B251 (1990) 488.

[Asa91]   K. Asahi, M. Ishihara, T. Ichihara, M. Fukuda, T. Kubo,
          Y. Gono, A. Mueller, R. Anne, D. Bazin, D. Guillemaud-
          Mueller, R. Bimbot, W. Schmidt-Ott, and J.Kasagi, *Obser-
          vation of Spin-Aligned Secondary Fragment Beams of ^{14}B*,
          Phys. Rev. **C43** (1991) 456.

[Asa92]   K. Asahi, H. Okuno, H. Ueno, H. Sato, J.Kura, T. Kubo,
          T. Nakamura, N. Inabe, A. Yoshida, Y. Ohkubo, M. Adachi,
          T. Ichihara, M. Ishihara, T. Shimoda, H. Miyatake, T. Taka-
          hashi, D. Beaumel, D. Morrissey, and W. Schmidt-Ott, *Spin-
          Oriented Projectile Fragments: The first application to g-
          factor measurements*, Hyp. Int. **75** (1992) 101.

[Baz90]   D. Bazin, D. Guerreau, R. Anne, D. Guillemaud-Mueller,
          A. Mueller, and M. Saint-Laurent, *Zero Degree Measurements
          of Isotopic Distributions in 44 MeV/u ^{86}Kr-Induced Reactions
          for the Production of Nuclei Far from Stability*, Nucl. Phys.
          A515 (1990) 349.

[Baz01]   D. Bazin, M. Lewitowicz, O. Sorlin, and O. Tarasov.
          *The Code "LISE": A New Version for "Win-
          dows"*, 2001. http://dnr080.jinr.ru/lise.html or
          http://www.ganil.fr/lise/prog.html.

[Ben66]   J. S. Bendat and A. G. Piersol, *Measurement and Analysis
          of Random Data*, (JOHN WILEY & SONS, Inc, New York,
          London, Sydney, 1966).

[Ber81]   M. Bernas, J. Peng, H. Doubre, M. Langevin, M. L. Vine,
          F. Pougheon, and P. Roussel, *Masses and Energy Levels of
          ^{62}Fe and ^{68}Ni: ($^{14}C,^{16}O$) Reaction on even Ni and Zn iso-
          topes*, Phys. Rev. **C24** (1981) 756.

[Ber82a] M. Bernas, P. Dessagne, M. Langevin, J. Payet, F. Pougheon,
          and P. Roussel, *Magic Features of ^{68}Ni*, Phys. Lett. **B113**
          (1982) 279.

[Ber82b]   H. Berry and M. Hass, *Beam-foil spectroscopy*, Ann. Rev. Nucl. Part. Sci. **32** (1982) 1-34.

[Boh75]   A. Bohr and B. R. Mottelson, *Nuclear Structure*, (W. A. Benjamin, Inc., London, 1975).

[Bos88]   U. Bosch, W.-D. Schmidt-Ott, E. Runte, P. Tidemand-Petersson, P. Koschel, F. Meissner, R. Kirchner, O. Klepper, E. Roeckl, K. Rykaczewski, and D. Schardt, *Beta- and Gamma-Decay Studies of Neutron-Rich Chromium, Manganese, Cobalt and Nickel Isotopes Including the New Isotopes ^{60}Cr and ^{60g}Mn*, Nucl. Phys. **A477** (1988) 89.

[Bro]   B. A. Brown. *The computer code OXBASH.* MSU-NSCL report number 524.

[Bro83]   B. Brown and B. Wildenthal, *Corrections to the free-nucleon values of the single-particle matrix elements of the M1 and Gamow-Teller operators, from a comparison of shell-model predictions with sd-shell data*, Phys. Rev. **C28** (1983) 2397.

[Bro87]   B. Brown and B. Wildenthal, *Empirically optimum M1 operator for the sd-shell nuclei*, Nucl. Phys. **A474** (1987) 290.

[Bro88a]   B. Brown, W. Richter, R. Julies, and B. Wildenthal, *Semi-Empirical Effective Interactions for the 1s-0d Shell*, Ann. Phys. **182** (1988) 191.

[Bro88b]   B. Brown and B. Wildenthal, *Status of the nuclear shell model*, Ann. Rev. Nucl. Part. Sci. **38** (1988) 29.

[Bro95]   R. Broda, B. Fornal, W. Krolas, T. Pawlat, D. Bazzacco, S.Lunardi, C. Rossi-Alvarez, R. Menegazzo, G. de Angelis, P. Bednarczyk, J.Rico, D. D. Acuna, P. Daly, R. Mayer, M. Sferrazza, H. Grawe, K. Maier, and R. Schubart, *N = 40 Neutron Subshell Closure in the ^{68}Ni Nucleus*, Phys. Rev. Lett. **74** (1995) 868.

[Bro98]   R. Broda, B. Fornal, W. Krolas, T. Pawlat, J. Wrzesinski, K. Maier, H. Grawe, M. Schramm, R. Schubart, D. Bazzacco, S. Lunardi, C. R. Alvarez, G. de Angelis, P. Daly, C. Zhang, and Z. Grabowski, *Spectroscopy of Nuclei Close to the ^{68}Ni Produced in Deep-Inelastic Heavy-Ion Reactions*, in: Fission

and Properties of Neutron-rich Nuclei, Proceedings of the International Conference, Sanibel Island, Florida 1997; (1998) 202.

[Bru77]   P. Brussaard and P. Glaudemans, *Shell-Model Applications in Nuclear Spectroscopy*, (North-Holland Publishing Company, Amsterdam, 1977).

[Cas90]   B. Castel and I. Towner, *Modern Theories of Nuclear Moments*, Oxford Studies in Nuclear Physics, (Clarendon Press, Oxford, 1990).

[Cau89]   E. Caurier. *computer code ANTOINE*, 1989. CRN, Strasbourg.

[Cou99]   N. Coulier, *Statiche momenten en spinorientatie van projectile-fragmentatiekernen bestudeerd met toestandsmengingstechniken*, (PhD thesis, 1999, unpublished).

[Cou01]   N. Coulier, G. Neyens, D. Balabanski, D. Borremans, R. Coussement, J. Daugas, G. Georgiev, S. Teughels, and K. Vyvey, *beta-level mixing resonance: A method to study the spin alignment and spin polarization of projectile fragments*, Phys. Rev. **C63** (2001) 054605.

[Dar71]   W. Darcey, R. Chapman, and S. Hinds, *A Study of the States of ^{60}Ni, ^{62}Ni, ^{64}Ni and ^{66}Ni Using the (t,p) Reaction*, Nucl. Phys. **A170** (1971) 253.

[Dau]   J. M. Daugas. private communication.

[Dau01]   J. Daugas, R. Grzywacz, M. Lewitowicz, M. Lopez-Jimenez, F. de Oliveira-Santos, J. Angelique, L. Axelsson, C. Borcea, C. Longour, and G. Neyens, *Interplay between angular momentum transfer and nuclear structure in the production of isomers at intermediate energies*, Phys. Rev. **C** (2001).

[Des84]   P. Dessagne, M. Bernas, M. Langevin, G. Morrison, J. Payet, F. Pougheon, and P. Roussel, *The Complex Transfer Reaction (^{14}C,^{15}O) on Ni, Zn and Ge Targets: Existence and mass of ^{69}Ni*, Nucl. Phys. **A426** (1984) 399.

[Det73]   C. Detraz, C. Zaidins, D. Frantsvog, R. Wilson, and A. Kunselman, *Beta-Decay of ^{32}Cl and ^{40}Sc*, Nucl. Phys. **A203** (1973) 414.

[Dob94]   J. Dobaczewski, I. Hamamoto, W. Nazarewicz, and J. Sheikh, *Nuclear shell structure at the particle drip-lines*, Phys. Rev. Lett. **72** (1994) 981.

[Duc99]   G. Duchene, F. Beck, P. Twin, G. de France, D. Curien, L. Han, C. Beausang, M. Bentley, P. Nolan, and J. Simpson, *The Clover: a new generation of composite Ge detectors*, Nucl. Instrum. Methods Phys. Res. **A432** (1999) 90-110.

[Ehr67]   D. V. Ehrenstein and J. Schiffer, *Study of the (d,p) Reactions on $Zn^{64,66,68,70}$*, Phys.Rev. **164** (1967) 1374.

[Fir96]   R. Firestone, *Table of Isotopes*, (John Wiley and Sons, Inc., New York, 8 edition, 1996).

[Fly72]   E. Flynn and J. Garrett, *The levels of ^{64}Co populated by the $^{64}Ni(t,\tau)$ reaction*, Phys. Lett. **B42** (1972) 49.

[Fra98]   S. Franchoo, M. Huyse, K. Kruglov, Y. Kudryavtsev, W. Mueller, R. Raabe, I. Reusen, P. V. Duppen, J. V. Roosbroeck, L. Vermeeren, A. Wöhr, K.-L. Kratz, B. Pfeiffer, and W. Walters, *Beta Decay of $^{68-74}Ni$ and Level Structure of Neutron-Rich Cu Isotopes*, Phys. Rev. Lett. **81** (1998) 3100.

[Fra99]   S. Franchoo, *Evolution of Nuclear Structure towards ^{78}Ni Investigated by the β Decay of Laser-Ionized $^{68-74}Ni$.*, (PhD thesis, 1999, unpublished).

[Fra01]   S. Franchoo, M. Huyse, K. Kruglov, Y. Kudryavtsev, W. Mueller, R. Raabe, I. Reusen, P. V. Duppen, J. V. Roosbroeck, L. Vermeeren, A. Wohr, H. Grawe, K.-L. Kratz, B. Pfeiffer, and W. Walters, *Monopole migration in $^{69,71,73}Cu$ observed from beta decay of laser-ionized $^{68-74}Ni$*, Phys. Rev. **C** (2001).

[Fri83]   W. Friedman, *Heavy ion projectile fragmentation: A reexamination*, Phys. Rev. **C27** (1983) 569.

[GEA]   GEANT - Detector Description and Simulation Tool, *http://wwwinfo.cern.ch/asdoc/geantold/GEANTMAIN.html*.

[Gir88]   M. Girod, P. Dessagne, M. Bernas, M. Langevin, F. Pougheon, and P.Roussel, *Spectroscopy of Neutron-Rich Nickel Isotopes: Experimental results and microscopic interpretation*, Phys. Rev. **C37** (1988) 2600.

[Gol74]   A. Goldhaber, *Statistical Models of Fragmentation Processes*, Phys. Lett. **B53** (1974) 306.

[Gol78]   A. Goldhaber and H. Heckmann, *High Energy Interactions of Nuclei*, Ann. Rev. Nucl. Part. Sci. **28** (1978) 161.

[Gol82]   G. Goldring, *in "Heavy Ion Collisions"*, (North Holland, Amsterdam, 1982).

[Gra99]   H. Grawe, M. Górska, M. Rejmund, M. Pfützner, M. Lipoglavšek, C. Fahlander, M. Hellström, D. Kast, A. Jungclaus, K. Lieb, R. Grzywacz, K. Rykaczewski, M. Lewitowicz, B. Brown, M. Hjorth-Jensen, and K. Maier, *Highlights of Modern Nuclear Structure*, (World Scientific Publishing Company, Singapore, 1999).

[Gra00]   H. Grawe, M. Górska, J. Döring, C. Fahlander, M. Palacz, F. Nowacki, E. Caurier, J. Daugas, M. Lewitowicz, M. Sawicka, M. Pfützner, R. Grzywacz, K. Rykaczewski, O. Sorlin, S. Leenhardt, F. Aziez, M. Rejmund, K. Hauschild, and J. Uusitalo, *Nuclear structure in the vicinity of shell closures far from stability*, AIP Conference proceedings, Tours Symposium on Nuclear Physics IV, TOURS 2000 (2000).

[Grz98]   R. Grzywacz, R. Beraud, C. Borcea, A. Emsallem, M. Glogowski, H. Grawe, D. Guillemaud-Mueller, M. Hjorth-Jensen, M. Houry, M. Lewitowicz, A. Mueller, A. Nowak, A. Plochocki, M. Pfutzner, K. Rykaczewski, M. Saint-Laurent, J. Sauvestre, M. Schaefer, O. Sorlin, J. Szerypo, W.Trinder, S. Viteritti, and J. Winfield, *New Island of μs Isomers in Neutron-Rich Nuclei Around the $Z = 28$ and $N = 40$ Shell Closures*, Phys. Rev. Lett. **81** (1998) 766.

[Haa]   H. Haas. private communication.

[Her89]   P. Herzog, U. Dammrich, K. Freitag, C.-D. Herrmann, and K. Schlosser, *The Magnetic Moments of ($\nu g_{9/2}$)-Levels in Odd Zn Isotopes*, Z. Phys. **A332** (1989) 247.

[HJ95]   M. Hjorth-Jensen, T. Kuo, and E. Osnes, *Realistic Effective Interactions for Nuclear Systems*, Phys. Rep. **261** (1995) 125.

[Hos85]   A. Hosaka, K.-I. Kubo, and H. Toki, *G-Matrix Effective Interaction with the Paris Potential*, Nucl. Phys. **A444** (1985) 76.

[HR69]   W. Hume-Rothery, R. Smallman, and C. Haworth, *The Structure of Metals and Alloys*, (Institute of Metals, London, 1969).

[Huf81]   J. Hufner and M. Nemes, *Relativistic Heavy Ions Measure the Momentum Distribution on the Nuclear Surface*, Phys. Rev. **C23** (1981) 2538.

[Ish00]   T. Ishii, M. Asai, A. Makishima, I. Hossain, M. Ogawa, J. Hasegawa, M. Matsuda, and S. Ichikawa, *Core-Excited States in the Doubly Magic ^{68}Ni and Its Neighbor ^{69}Cu*, Phys. Rev. Lett. **84** (2000) 39.

[Ji89]   X. Ji and B. Wildenthal, *Shell-Model Calculations of the Neutron-Rich ^{40}Cl Nucleus*, Phys. Rev. **C39** (1989) 701.

[Ken01]   O. Kenn, K.-H. Speidel, R. Ernst, J. Gerber, N.Benczer-Koller, G. Kumbartzki, P. Maier-Komor, and F. Nowacki, *Striking Harmony between the Nuclear Shell Model and New Experimental g Factors and B(E2) Values of Even Ni Isotopes*, Phys. Rev. **C63** (2001) 021302.

[Kou78a]   R. Kouzes and D. Mueller, *The Mass of ^{65}Co*, Nucl. Phys. **A307** (1978) 71.

[Kou78b]   R. Kouzes, D. Mueller, and C. Yu, *Mass of ^{67}Ni*, Phys. Rev. **C18** (1978) 1587.

[Kra86]   K. Krane, in *Low Temperature Nuclear Orientation*, chapter 2, (North-Holland, Amsterdam, 1986).

[Kra88]   K. Krane, *Introductory Nuclear Physics*, (John Wiley & Sons, Inc., New York, 1988).

[Lan67]   H. Lange, *Correlation Techniques*, (Iliffe Books, Ltd., London, 1967).

[Leo94]   W. R. Leo, *Techniques for Nuclear and Particle Physics Experiments*, (Springer-Verlag, Berlin, second edition, 1994).

[Leo98]   A. Leon, S. Melki, D. Lisfi, J. Grandin, P. Jardin, M. Suraud, and A. Cassimi, *Charge state distribution of swift heavy ions behind various solid targes (36≤ Z_p ≤ 92, 18 MeV/u ≤ E ≤ 44 MeV/u)*, Atomic Data and Nuclear Data Tables **69** (1998) 217 - 238.

[Lew99]   M. Lewitowicz, *Study of Nuclei Far from Stability at Intermediate Energies: Present Status and Future*, Proc. Int. Conf. Experimental Nuclear Physics in Europe, June 1999, Sevilla, Spain, AIP proceedings 495 (1999) 43.

[Mac01]   H. Mach, M. Lewitowicz, M. Stanoiu, R. Grzywacz, K. Rykaczewski, F. Becker, J. Blomqvist, M. Borge, R. Boutami, B. Cederwall, Z. Dlouhy, B. Fogelberg, L. Fraile, G. Georgiev, H. Grawe, P. Johansson, W. Klamra, S. Lukyanov, M. Mineva, J. Mrazek, G. Neyens, F. de Oliveira Santos, M. Pftzner, Y. Penionzhkevich, E. Ramström, and M. Sawicka, *Probing the Structure of Exotic Nuclei by Advanced Time-Delayed Methods; Studies of s Isomers at LISE in GANIL and RMS at HRIBF*, Proceedings of the international conference ISOL'01, March 11-14, 2001, Oak Ridge, Tennessee (2001).

[Man97]   P. Mantica, R. Ibbotson, D. Anthony, M. Fauerbach, D. Morrissey, C. Powell, J. Rikovska, M. Steiner, N. Stone, and W. Walters, *Sign Dependence of Spin Polarization for Secondary Fragments Produced following Intermediate-Energy Projectile Fragmentation*, Phys. Rev. **C55** (1997) 2501.

[Mat71]   E. Matthias, B. Olsen, D. Shirley, J. Templeton, and R. Steffen, *Theory of the Nuclear Magnetic Resonance Detected by Nuclear Radiations*, Phys. Rev. **A4** (1971) 1626.

[Mor76]   H. Morinaga and T. Yamazaki, *In-beam γ-ray spectroscopy*, (North Holland, Amsterdam, 1976).

[Mor89]   D. Morrissey, *Systematics of Momentum Distributions from Reactions with Relativistic Ions*, Phys. Rev. **C39** (1989) 460.

[Mot95]   T. Motobayashi, Y. Ikeda, Y. Ando, K. Ieki, M. Inoue, N. Iwasa, T. Kikuchi, M. Kurokawa, S. Moriya, S. Ogawa, H. Murakami, S. Shimoura, Y. Yanagisawa, T. Nakamura, Y. Watanabe, M. Ishihara, T. Teranishi, H. Okuno, and

R. Casten, *Large Deformation of the Very Neutron-Rich Nucleus ^{32}Mg from Intermediate-Energy Coulomb Excitation*, Phys. Lett. **B346** (1995) 9.

[Mue] W. Mueller. private communication.

[Mue99] W. Mueller, B. Bruyneel, S. Franchoo, H. Grawe, M. Huyse, U. Koster, K.-L. Kratz, K. Kruglov, Y. Kudryavtsev, B. Pfeiffer, R. Raabe, I. Reusen, P. Thirolf, P. V. Duppen, J. V. Roosbroeck, L. Vermeeren, W. Walters, and L. Weissman, *Magicity of the ^{68}Ni Semidouble-Closed-Shell Nucleus Probed by Gamow-Teller Decay of the Odd-A Neighbors*, Phys. Rev. Lett. **83** (1999) 3613.

[Mue00] W. Mueller, B. Bruyneel, S. Franchoo, M. Huyse, J. Kurpeta, K. Kruglov, Y. Kudryavtsev, N. Prasad, R. Raabe, I. Reusen, P. V. Duppen, J. V. Roosbroeck, L. Vermeeren, L. Weissman, Z. Janas, M. Karny, T. Kszczot, A. Plochocki, K.-L. Kratz, B. Pfeiffer, H. Grawe, U. Koster, P. Thirolf, and W. Walters, *beta Decay of ^{66}Co, ^{68}Co, and ^{70}Co*, Phys. Rev. **C61** (2000) 054308.

[Mul89] W. Muller, H. Bertschat, H. Hass, B. Spellmeyer, and W.-D. Zeitz, *Magnetic hyperfine interaction studies of isolated Ni impurities in Pd and Pd-Pt alloys*, Phys. Rev. **B40** (1989) 7633.

[Ney97a] G. Neyens, N. Coulier, S. Ternier, K. Vyvey, S. Michiels, R. Coussement, D. Balabanski, J. Casandjian, M. Chartier, M. Cortina-Gil, M. Lewitowicz, W. Mittig, A. Ostrowski, P. Roussel-Chomaz, N. Alamanos, and A. Lépine-Szily, *Nuclear Spin Alignment and Static Moments of Light Projectile Fragments Measured with the Level Mixing Resonance (LMR) Method*, Phys. Lett. **B393** (1997) 36.

[Ney97b] G. Neyens, G. S'heeren, and R. Coussement, *Nuclear Orientation in a Two-Step Laser Ionization Process*, Nucl. Instrum. Methods Phys. Res. **B122** (1997) 121.

[Noy59] H. Noya, A. Arima, and H. Horie, *Nuclear Moments and Configuration Mixing*, Progr. Theor. Phys. Suppl. **8** (1959) 33.

[Oku93]   H. Okuno, K. Asahi, H. Ueno, H. Sato, M. Adachi, T. Kubo,
          T. Nakamura, N. Inabe, A. Yoshida, Y. Ohkubo, T. Ichihara,
          M. Ishihara, H. Miyatake, and T. Takahashi, Hyp. Int. **76**
          (1993) 257.

[Oku94]   H. Okuno, K. Asahi, H. Sato, H. Ueno, J.Kura, M. Adachi,
          T. Nakamura, T. Kubo, N. Inabe, A. Yoshida, T. Ichihara,
          Y. Kobayashi, Y. Ohkubo, M. Iwamoto, F. Ambe, T. Shi-
          moda, H. Miyatake, T. Takahashi, J. Nakamura, D. Beaumel,
          D. Morrissey, W. Schmidt-Ott, and M. Ishihara, *Systematic
          Behavior of Ejectile Spin Polarization in the Projectile Frag-
          mentation Reaction*, Phys. Lett. **B335** (1994) 29.

[Oza00]   A. Ozawa, T. Kobayashi, T. Suzuki, K. Yoshida, and I. Tani-
          hata, *New Magic Number, N = 16, Near the Neutron Drip
          Line*, Phys. Rev. Lett. **84** (2000) 5493.

[PAW]   *Physics   Analysis   Workstation   Package.*
          http://paw.web.cern.ch/paw/.

[Paw94]   T. Pawlat, R. Broda, W. Krolas, A. Maj, M. Zieblinski,
          H. Grawe, R. Schubart, K. Maier, J. Heese, H. Kluge, and
          M. Schramm, *Spectroscopy of Neutron-Rich Ni Isotopes Pro-
          duced in ^{208}Pb + ^{64}Ni Collisions*, Nucl. Phys. **A574** (1994)
          623.

[Pos86]   H. Postma and N. Stone, editors, *Low-Temperature Nuclear
          Orientation*, (North-Holland, Amsterdam, 1986).

[Pri99]   J. Prisciandaro, P. Mantica, A. Oros-Peusquens, D. Anthony,
          M. Huhta, P. Lofy, and R.M.Ronningen, *beta Decaying $T_{1/2}$
          = 3.4 s Isomer in ^{69}Ni*, Phys. Rev. **C60** (1999) 054307.

[Pur46]   E. Purcell, H. Torrey, and R. Pound, Phys. Rev. **69** (1946) 37.

[Rag89]   P. Raghavan, *Table of Nuclear Moments*, At. Data Nucl. Data
          Tables **42** (1989) 189.

[Rei00]   P.-G. Reinhard, M. Bender, T. Buervenich, C. Reiss,
          J. Maruhn, and W. Greiner, *Skyrme-Hartree-Fock in the realm
          of nuclear mean field models*, RIKEN Review **26** (2000) 23 -
          30.

[Rik00]   J. Rikovska, T. Giles, N. Stone, K. van Esbroeck, G. White, A. Wohr, M. Veskovic, I. Towner, P. Mantica, J. Prisciandaro, D. Morrissey, V. Fedoseyev, V. Mishin, U. Koster, W. Walters, , the NICOLE, and I. Collaborations, *First On-Line β-NMR on Oriented Nuclei: Magnetic dipole moments of the $(\nu p_{1/2})_{1/2^-}^{-1}$ Ground State in ^{67}Ni and $(\pi p_{3/2})_{3/2^-}^{+1}$ Ground State in ^{69}Cu*, Phys. Rev. Lett. **85** (2000) 1392.

[Rog00]   W. Rogers, G. Georgiev, G. Neyens, D. Borremans, N.Coulier, R. Coussement, A. Davies, J. Mitchell, S. Teughels, B. Brown, and P. Mantica, *Ground-State Magnetic Moment of the $T = 1$ Nucleus ^{32}Cl using On-Line β-NMR Spectroscopy*, Phys.Rev. **C62** (2000) 044312.

[Ros78]   F. Rosel, H. Friess, K. Alder, and H. Pauli, *Internal Conversion Coefficients for all Atomic Shells*, At.Data Nucl.Data Tables **21** (1978) 92, 291.

[Roz96]   J. Rozet, C. Stephan, and D. Vernhet, *ETACHA: a program for calculating charge states at GANIL energies*, Nucl. Instr. Meth. Phys. Res. **B107** (1996) 67-70.

[Run83]   E. Runte, W.-D. Schmidt-Ott, P. Tidemand-Petersson, R. Kirchner, O. Klepper, W. Kurcewicz, E. Roeckl, N. Kaffrell, P. Peuser, K. Rykaczewski, M. Bernas, P. Dessagne, and M. Langevin, *Decay Studies of Neutron-Rich Products from ^{76}Ge-Induced Multinucleon Transfer Reactions Including the New Isotopes ^{62}Mn, ^{63}Fe and $^{71,72,73}Cu$*, Nucl. Phys. **A399** (1983) 163.

[Sei94]   H. Seifert, J. Wouters, D. Vieira, H. Wollnik, X. Zhou, X. Tu, Z. Zhou, and G. Butler, *Mass Measurement of Neutron-Rich Isotopes from ^{51}Ca to ^{72}Ni*, Z. Phys. **A349** (1994) 25.

[She77]   J. Sherman, E. Flynn, O. Hansen, N. Stein, and J. Sunier, *A Study of ^{64}Cu, ^{66}Cu, ^{68}Cu and ^{70}Cu by $(t,^3He)$ Reactions*, Phys. Lett. **B67** (1977) 275.

[She91]   B. Sherrill, D. Morrissey, J. NolenJr., and J. Wigner, *The A1200 projectile fragment separator*, Nucl. Instrum. Methods Phys. Res. **B56/57** (1991) 1106 - 1110.

[She99] S. Shepherd, P. Nolan, D. Cullen, D. Appelbe, J. Simpson, J. Gerl, M. Kaspar, A. Kleinboehl, I. Peter, M. Rejmund, H. Schaffner, C. Schlegel, and G. de France, *Measurements on a prototype segmented Clover detector*, Nucl. Instrum. Methods Phys. Res. **A434** (1999) 373-386.

[Sie65] K. Siegbahn, editor, in *Alpha-, beta- and gamma-ray spectroscopy*, chapter XIX A, Angular correlations, p. 1193, (North-Holland Publishing Company, Amsterdam, New York, Oxford, 1965).

[Sin92] J. Sinatkas, L. Skouras, D. Strottman, and J. Vergados, *Shell-Model Calculations in the A = 80-100 Mass Region: I. A study of the N = 50 nuclei; II. A study of the N = 49,48 nuclei*, J. Phys. **G18** (1992) 1377, 1401.

[SO94] W.-D. Schmidt-Ott, K. Asahi, Y. Fujita, H. Geissel, K.-D. Gross, T. Hild, H. Irnich, M. Ishihara, K. Krumbholz, V. Kunze, A. Magel, F. Meissner, K. Muto, F. Nickel, H. Okuno, M. Pfutzner, C. Scheidenberger, K. Suzuki, M. Weber, and C. Wennemann, *Spin Alignment of ^{43}Sc Produced in the Fragmentation of 500 MeV/u ^{46}Ti*, Z. Phys. **A350** (1994) 215-219.

[Sto84] W. Stoeffl. *FITEK program*, 1984. Lawrence Livermore National Laboratory.

[Sug69] K. Sugimoto, *Magnetic Moments and beta-Decay ft Values of Mirror Nuclei*, Phys. Rev. **187** (1969) 1051.

[Tow77] I. Towner, F. Khanna, and O. Hausser, *Magnetic Moments in N = 126 Isotones and Core Polarisation Blocking*, Nucl. Phys. **A277** (1977) 285.

[Uen96] H. Ueno, K. Asahi, H. Izumi, K. Nagata, H. Ogawa, A. Yoshimi, H. Sato, M. Adachi, Y. Hori, K. Mochinaga, H. Okuno, N. Aoi, M. Ishihara, A. Yoshida, G. Liu, T. Kubo, N. Fukunishi, T. Shimoda, H. Miyatake, M. Sasaki, T. Shirakura, N. Takahashi, S. Mitsuoka, and W.-D. Schmidt-Ott, *Magnetic Moments of ^{17}N and ^{17}B*, Phys. Rev. **C53** (1996) 2142.

[Van86] L. Vanneste, in *Low Temperature Nuclear Orientation*, chapter 3, (North-Holland, Amsterdam, 1986).

[Vyv00]   K. Vyvey, G. Neyens, N. Coulier, R. Coussement, G. Georgiev, S. Ternier, S. Teughels, A. Lepine-Szily, and D. Balabanski, *Preservation of Orientation of Fusion-Evaporation Reaction Residues Recoiling into Vacuum in a Level Mixing Spectroscopy Experiment*, Phys. Rev. **C62** (2000) 034317.

[Wei99]   L. Weissman, A. Andreyev, B. Bruyneel, S. Franchoo, M. Huyse, K. Kruglov, Y. Kudryavtsev, W. Mueller, R. Raabe, I. Reusen, P. V. Duppen, J. V. Roosbroeck, L. Vermeeren, U. Koster, K. Kratz, B. Pfeiffer, P. Thirolf, and W. Walters, *Beta Decay of ^{67}Co*, Phys. Rev. **C59** (1999) 2004.

[Zei78]   B. Zeidman and J. N. Jr., *Mass and Low-Lying Energy Levels of ^{69}Cu*, Phys. Rev. **C18** (1978) 2122.